Universidad de Valladolid

Escuela de Doctorado Universidad de Valladolid

PhD PROGRAMME IN

INDUSTRIAL ENGINEERING

DOCTORAL THESIS:

DEVELOPMENT OF ELECTROMAGNETIC-BASED APPROACHES FOR NON-DESTRUCTIVE EVALUATION AND HEALTH MONITORING OF AEROSPACE STRUCTURAL JOINTS

Submitted by MATTIA MAZZESCHI
in fulfilment of the requirements for
PhD Degree by the University of Valladolid

Directed by:

ESTEBAN CAÑIBANO ALVAREZ

KARINA CARLA NÚÑEZ CARRERO

Development of Electromagnetic-Based Approaches for Non-Destructive Evaluation and Health Monitoring of Aerospace Structural Joints

by

Mattia Mazzeschi

Directed by:

Esteban Cañibano Alvarez

Karina Carla Núñez Carrero

Universidad de Valladolid
School of Industrial Engineering
University of Valladolid

Department of Materials,
Products and Processes
Fundación Cidaut

ABSTRACT

The increasing use of lightweight materials such as aluminium alloys and carbon fibre-reinforced polymers (CFRP) in the aerospace industry has created a need for advanced, reliable non-destructive evaluation (NDE) and structural health monitoring (SHM) techniques. These materials are widely used in critical structural applications, where their performance, durability, and integrity directly impact safety. Consequently, the ability to monitor and assess the quality of aerospace joints, both during the manufacturing process and throughout their service life, is essential. This research focuses on the development of electromagnetic-based approaches for monitoring aerospace structural joints, specifically friction stir welded (FSW) aluminium alloys and thermoplastic welded CFRP laminates. The thesis is divided into two main applications, each representing a distinct case where an electromagnetic-based approach was developed and optimized for a specific type of joint.

The first application addresses the real-time process monitoring of FSW aluminium joints (CASE I). Through a series of parametric studies and numerical simulations, the optimal design for an Eddy Current Testing (ECT) probe was identified, aimed at detecting subsurface defects, such as wormholes. Experimental results demonstrated the probe ability to accurately detect these defects, particularly on the lower surface of the joint, while establishing significant correlations between electrical conductivity, microhardness, and mechanical properties such as ultimate tensile strength (UTS). This highlights the potential of ECT as an effective method for real-time process monitoring in the manufacturing of aerospace joints.

The second application focuses on the structural health monitoring of thermoplastic induction welded CFRP laminates (CASE II). In this context, two electromagnetic sensors were developed: the PM (Purely Magnetic) sensor, based on a purely magnetic approach, and the H (Hybrid) sensor, which integrates both magnetic and electric field measurements. While the PM sensor showed limitations in detecting dielectric variations within the weld, the H sensor exhibited superior sensitivity, particularly in capturing changes related to dielectric permittivity, making it highly effective for defect detection and localization in CFRP laminates. This work contributes to the advancement of electromagnetic NDE and SHM methods, with findings that pave the way for future integration of these techniques in real-time monitoring systems.

Keywords: Aerospace Structures, Friction Stir Welding, Thermoplastic Welding, Structural Health Monitoring, Non-Destructive Evaluation.

RESUMEN

El creciente uso de materiales ligeros como las aleaciones de aluminio y los polímeros reforzados con fibra de carbono (CFRP) en la industria aeroespacial ha generado la necesidad de desarrollar técnicas avanzadas y fiables de evaluación no destructiva (NDE) y monitorización de la salud estructural (SHM). Estos materiales se utilizan ampliamente en aplicaciones estructurales críticas, donde su rendimiento, durabilidad e integridad tienen un impacto directo en la seguridad. Por lo tanto, la capacidad de supervisar y evaluar la calidad de las uniones aeroespaciales, tanto durante el proceso de fabricación como a lo largo de su vida útil, es esencial.

Objetivos: La presente investigación tiene como objetivo principal investigar y desarrollar técnicas de monitorización basadas en métodos electromagnéticos,

específicamente el uso de Corrientes de Eddy (ECT) y sensores electromagnéticos, para la evaluación y supervisión de uniones estructurales aeroespaciales durante su fabricación y vida útil. Esto se enfoca en abordar las necesidades de la industria aeroespacial para la detección de defectos y la predicción de la salud estructural de uniones de aleaciones de aluminio y CFRP.

Metodología: La tesis se estructura en dos aplicaciones específicas. En la primera (CASO I), se estudia la monitorización en tiempo real del proceso de soldadura por fricción-agitación (FSW) en aleaciones de aluminio. Se llevaron a cabo estudios paramétricos y simulaciones numéricas para definir el diseño óptimo de una sonda ECT, orientada a detectar defectos como "wormholes". Esta etapa experimental permitió establecer correlaciones entre la conductividad eléctrica y propiedades microestructurales y mecánicas.

En la segunda aplicación (CASO II), se desarrollan sensores electromagnéticos para SHM de uniones de CFRP soldadas por inducción. Dos configuraciones de sensores fueron analizadas: el sensor PM, basado en un enfoque puramente magnético, y el sensor H, que combina mediciones de campos magnéticos y eléctricos. La investigación abarcó tanto la evaluación experimental de la sensibilidad de los sensores a defectos como el análisis detallado de su capacidad para detectar variaciones en las propiedades eléctricas, asociadas con la presencia de defectos de distintos tamaños y ubicaciones en el laminado de CFRP.

Resultados: Para el CASO I, la sonda ECT diseñada demostró una alta capacidad para detectar defectos subsuperficiales en la parte inferior de las uniones FSW, mostrando correlaciones significativas entre la variación de conductividad eléctrica y propiedades como la microdureza y la resistencia a la tracción. Estos resultados resaltan el potencial del ECT como técnica de monitorización en tiempo real durante la fabricación. En el CASO II, tanto el sensor PM como el sensor H demostraron buena sensibilidad para la detección de variaciones de propriedades eléctricas asociadas a la presencia de defectos en laminados de CFRP. Sin embargo, al considerar aplicaciones específicas como la inspección de uniones soldadas por inducción, el sensor H mostró una sensibilidad superior y una mayor resistencia al efecto borde. Esto sugiere que el sensor H tiene un fuerte potencial para la detección y localización de defectos en estructuras termoplásticas de CFRP.

Conclusiones: La investigación demuestra que las técnicas electromagnéticas desarrolladas son herramientas prometedoras para el monitoreo de calidad y salud estructural de uniones aeroespaciales. La sonda ECT se destaca por su aplicabilidad en el proceso de soldadura FSW, mientras que el sensor H muestra un alto potencial para la monitorización de la salud estructural de uniones de CFRP. En conjunto, los hallazgos de esta tesis establecen una sólida base para la implementación de sistemas de monitorización que contribuyen significativamente a mejorar la integridad y seguridad de estructuras aeroespaciales a lo largo de su ciclo de vida.

Palabras clave: Estructuras Aeroespaciales, Soldadura por Fricción-Agitación, Soldadura Termoplástica, Monitorización de la Salud Estructural, Evaluación No Destructiva.

Acknowledgements

Many people to thank, and certainly only a few words that can truly reflect my gratitude. The development and completion of this thesis has been a journey of perseverance and learning, made possible by the unwavering support of many people along the way.

I want to express my sincere thanks to my thesis directors, Esteban Cañibano and Karina Núñez. Esteban has supported me from the inception of the idea through to the completion of this work, always providing valuable insights that greatly enriched the scientific value of my thesis. Karina's support has been truly enriching; she continually motivated me to aim higher and maintained the highest standards in the development of the research. Her availability and dedication, always there to clarify any questions, made a tremendous difference.

I am deeply grateful to Jose Maria Pastor, my thesis tutor. If I had the opportunity to embark on this wonderful thesis journey, it is largely due to him. From the moment I reached out to him, looking for research opportunities, he was kind enough to not only respond but to introduce me to Fundacion Cidaut, which marked the beginning of a new professional chapter for me. His mentorship and guidance have been instrumental throughout the process, particularly in helping to overcome the administrative challenges encountered.

I also wish to thank Juan Carlos Merino, Director of Fundacion Cidaut and my thesis director during its early stages. His strong technical insight provided invaluable guidance throughout each revision of the thesis, shaping both the methodology and the analysis of this work.

Special thanks go to Maite Fernández, Head of Dissemination and Technology Transfer at Cidaut, for her trust in this project and for the essential financial support. Additionally, I extend my gratitude to all my colleagues at Cidaut who, in their own ways, contributed to the success of this work. In particular, I thank Jose Francisco Diez for his useful advice on electronics and for his great patience in accommodating my needs, despite his own numerous commitments.

My deep and infinite thanks are and always will be to my wife, Rut. This achievement is as much hers as it is mine. Her patience and unwavering support during the long hours of work and time spent away from family life were crucial. To my parents, Roberto and Anna, I am profoundly grateful for everything they've done. Their teaching of ambition and perseverance, no matter the challenge, has brought me to where I am today. I would like to extend my gratitude to the rest of my family, particularly Miguel Ángel and Consuelo, for their unwavering support and for always being there when I needed them most.

I would also like to thank Alfredo Güemes, Professor of the Universidad Politécnica de Madrid, for his guidance and for trusting me by giving me the opportunity to embark on an international PhD stay at Stanford University. I am also deeply grateful to Professor Fu-Kuo Chang for welcoming me into the Structures and Composites Laboratory (SACL) at Stanford in such an engaging and inspiring way. My sincere thanks also go to Saman Farhangdoust for his mentorship during the Stanford Scholar Visiting Program. Thanks to the rest of the SACL team, particularly Shabbir Ahmed and Pu Xie, for their essential support.

My sincere thanks also go to Daniel Moriñigo, Professor of Electrical Engineering at University of Valladolid, for his insightful guidance on electromagnetism and electrical systems.

A special thanks to Carlos Rodriguez, founder of ISEND, and to Miguel Sanz and Julio Monge, valued members of the ISEND team, for their collaboration and the expertise they shared in Eddy Current Testing.

Last but not least, I give thanks to God. Reflecting on this journey I am moved to quote the words of Galileo Galilei, who said, *"I do not feel obliged to believe that the same God who gave us sense, reason and intellect wanted us to renounce their use."* Faith and science, often seen as opposites, have always walked hand in hand throughout history. Great minds, Isaac Newton, Johannes Kepler, and James Clerk Maxwell, to name a few, sought to understand the universe, knowing that their discoveries did not conflict with their belief in a greater order. This harmonious balance inspires me, reminding us that the pursuit of knowledge is not only a quest for understanding but also a way to appreciate the profound purpose of life and our existence in the universe.

Agradecimientos

Muchas personas a las que agradecer, y seguramente pocas palabras aquí pueden reflejar verdaderamente mi gratitud. El desarrollo y culminación de esta tesis ha sido un viaje de perseverancia y aprendizaje, posible gracias al apoyo incondicional de muchas personas en el camino.

Quiero expresar mi más sincero agradecimiento a mis directores de tesis, Esteban Cañibano y Karina Núñez. Esteban me ha apoyado desde la concepción de la idea hasta la finalización de este trabajo, brindando siempre valiosos aportes que enriquecieron enormemente el valor científico de mi tesis. El apoyo de Karina ha sido verdaderamente enriquecedor; ella me ha motivado continuamente a apuntar más alto y ha mantenido los más altos estándares en el desarrollo de la investigación. Su disponibilidad y dedicación, siempre ahí para aclarar cualquier duda, hicieron una gran diferencia.

Estoy profundamente agradecido con José María Pastor, mi tutor de tesis. Si tuve la oportunidad de embarcarme en este maravilloso camino, es en gran parte gracias a él. Desde el momento en que me acerqué a él buscando oportunidades de investigación, tuvo la amabilidad no solo de responder, sino de presentarme a la Fundación Cidaut, lo cual marcó el comienzo de una nueva etapa profesional para mí. Su guía y mentoría han sido fundamentales a lo largo de todo el proceso, especialmente al ayudarme a superar los desafíos administrativos que se presentaron.

También deseo agradecer a Juan Carlos Merino, Director de la Fundación Cidaut y director de mi tesis durante sus primeras etapas. Su fuerte conocimiento técnico proporcionó orientación inestimable a lo largo de cada revisión de la tesis, dando forma tanto a la metodología como al análisis de este trabajo.

Un agradecimiento especial a Maite Fernández, Responsable de Difusión y Transferencia de Tecnología en Cidaut, por su confianza en este proyecto y por el apoyo financiero esencial. Además, extiendo mi gratitud a todos mis colegas de Cidaut que, de una u otra forma, contribuyeron al éxito de este trabajo. En particular, agradezco a José Francisco Diez por sus valiosos consejos sobre electrónica y por su gran paciencia para atender mis necesidades, a pesar de sus numerosos compromisos.

Mis profundos y infinitos agradecimientos son y serán siempre para mi mujer, Rut. Este logro es tanto suyo como mío. Su paciencia y apoyo incondicional durante las largas horas de trabajo y el tiempo alejado de la vida familiar fueron cruciales. A mis padres, Roberto y Anna, les estoy profundamente agradecido por todo lo que han hecho. Su enseñanza de ambición y perseverancia, sin importar el desafío, me ha llevado hasta

donde estoy hoy. Y cómo no, dar las gracias al resto de la familia, en especial a Miguel Ángel y Consuelo, que siempre han estado ahí cuando más lo he necesitado.

También quiero agradecer a Alfredo Güemes, Profesor de la Universidad Politécnica de Madrid, por su orientación y por confiar en mí dándome la oportunidad de llevar a cabo una estancia internacional de doctorado en la Universidad de Stanford. También estoy profundamente agradecido al Prof. Fu-Kuo Chang por recibirme en el Laboratorio de Estructuras y Materiales Compuestos (SACL) de Stanford de una manera tan comprometida e inspiradora. Mi más sincero agradecimiento también a Saman Farhangdoust por su mentoría durante el Programa de Visiting Scholar en Stanford. Gracias al resto del equipo del SACL, en particular a Shabbir Ahmed y Pu Xie, por su apoyo esencial.

Mis más sinceros agradecimientos también a Daniel Moriñigo, Profesor de Ingeniería Eléctrica de la Universidad de Valladolid, por sus valiosos consejos sobre electromagnetismo y sistemas eléctricos.

Un agradecimiento especial a Carlos Rodríguez, fundador de ISEND, y a Miguel Sanz y Julio Monge, valiosos miembros del equipo de ISEND, por su colaboración y el conocimiento compartido en Ensayos por Corrientes Inducidas.

Por último, pero no menos importante, agradezco a Dios. Reflexionando sobre este camino, me inspira citar las palabras de Galileo Galilei, quien dijo: "*No me siento obligado a creer que el mismo Dios que nos ha dotado de sentido, razón e intelecto, haya querido que renunciemos a su uso*." Fe y ciencia, a menudo vistas como opuestos, siempre han caminado de la mano a lo largo de la historia. Grandes mentes como Isaac Newton, Johannes Kepler y James Clerk Maxwell , por citar solo algunas, buscaron comprender el universo, sabiendo que sus descubrimientos no contradecían su creencia en un orden superior. Este equilibrio armonioso me inspira, recordándonos que la búsqueda del conocimiento no solo es un esfuerzo por comprender, sino también una manera de apreciar el profundo propósito de la vida y nuestra existencia en el universo.

Contents

List of Figures

List of Tables

List of Abbreviations

ACFM	Alternating Current Field Measurement
ACPD	Alternating Current Potential Difference
AE	Acoustic Emission
AHM	Aircraft Health Management
AI	Artificial Intelligence
BT	Barium Titanate
CBM	Condition-Based Maintenance
CFRP	Carbon Fibre Reinforced Polymers
CNS	Carbon Nanostructure
CNT	Carbon Nanotubes
CVM	Comparative vacuum monitoring
DCPD	Direct Current Potential Difference
DIP	Digital Image Processing
DY	Calendar Days
ECFS	Eddy Current Foil Sensors
ECP	Electric Current Perturbation
ECT	Eddy Current Testing
EIT	Electrical impedance tomography
EM	Electromagnetic
EMAT	Electromagnetic Acoustic Transducers
EMIS	Electromechanical impedance spectroscopy
EM-NDT	Electromagnetic Non-Destructive Testing
EPM	Electrical Resistance Tomography
ERT	Electrical Potential Mapping
eVTOL	Electric Vertical Takeoff and Landing
FBG	Fiber Bragg Grating
FC	Flight Cycles
FEM	Finite Element Method
FH	Flight Hours
FOS	Fibre Optic Sensor
FRP	Fibre-Reinforced Polymer
FSW	Friction Stir Welding
GF/PP	Glass Fiber/Polypropylene
GFRP	Glass Fiber Reinforced Polymers
GPR	Ground Penetrating Radar
H	Hybrid
HAZ	Heat-Affected Zone
LET	Lorentz Force Eddy Current Testing
MBN	Magnetic Barkhausen Noise
MFL	Magnetic Flux Leakage
MMM	Metal Magnetic Memory
MPI	Magnetic Particle Inspection
MRB	Material Review Board
MWCNTs	Multi-Walled Carbon Nanotubes
MWMTM-Array	Meandering Winding Magnetometer Array
NDE	Non-Destructive Evaluation
NDT	Non-Destructive Testing

PAUT	Phased Array Ultrasonic Inspection
PEC	Pulsed Eddy Current Testing
PM	Purely Magnetic
PMP	Permanent Magnetic Perturbation
PZT	Piezoelectric
SGs	Strain Gauges
SHM	Structural Health Monitoring
SNR	Signal-to-Noise Ratio
SSMs	Self-Sensing Materials
SWCNTs	Single-Walled Carbon Nanotubes
SZ	Stir Zone
TDR	Time Domain Reflectometry
TMAZ	Thermo-Mechanically Affected Zone
TPCs	Thermoplastic Composites
UGW	Ultrasonic guided waves
UM	Usage Monitoring
UTS	Ultimate Tensile Strength

Chapter 1

1 Introduction

1.1 Context and Motivation

The aerospace sector is undergoing rapid expansion, encompassing **aeronautical industries** and emerging markets such as **Electric Vertical Takeoff and Landing (eVTOL)** aircraft and **space exploration**. These segments are experiencing a significant rise in demand due to increased urban mobility solutions and the growing commercial space sector. Forecasts suggest that the global eVTOL market, valued at USD 11.3 billion in 2023, will expand to USD 30.8 billion by 2030 [1]. Similarly, the space industry, currently estimated at USD 469 billion, is projected to surpass USD 1 trillion by 2040 [2]. These dynamic trends, coupled with advancements in aviation technologies, reflect a broader need for innovation across material science, manufacturing techniques, and structural integrity throughout the lifecycle of aerospace components.

One of the key drivers of innovation in aerospace manufacturing is the **need for lightweight, high-performance materials** that can meet the rigorous demands of flight while reducing environmental impact. **High-strength aluminium alloys** and **thermoplastic composites** have emerged as critical materials for achieving the dual goals of weight reduction and enhanced structural performance in aerospace applications. Thermoplastic composites, in particular, are noted for their potential to reduce aircraft manufacturing times while offering superior recyclability compared to traditional thermosetting materials [3]. Moreover, the distinctive attribute of thermoplastic matrices to be melted repetitively without altering their physical properties makes possible the implementation of **fusion bonding techniques** with a consequent weight saving potential thanks to aircraft fasteners and adhesives elimination.

However, despite advancements in composite materials, high-strength aluminium alloys remain indispensable. They offer excellent strength-to-weight ratios, ductility, and lower environmental impact due to their recyclability [4]. Their increasing use in both the aerospace and automotive industries highlights the potential for these materials to contribute significantly to cleaner, more sustainable transportation systems [4].

Joining techniques like **friction stir welding (FSW)** have become indispensable in aerospace manufacturing, enabling the formation of robust, defect-free joints in similar materials. FSW is a solid-state joining technique where a rotating tool generates heat through friction at the interface of two materials, softening them without reaching the melting point. This lower processing temperature prevents typical problems of fusion

welding, such as porosity, distortion, and contamination, making it particularly advantageous for high-strength aluminum alloys [5]. FSW has become an essential process in aerospace manufacturing not only for its technical benefits but also for its contributions to sustainability [6]–[8]. By allowing the production of lighter structures, FSW helps reduce the overall weight of aircraft, which in turn decreases fuel consumption and lowers greenhouse gas emissions during operation. Moreover, FSW is environmentally efficient compared to fusion welding. It eliminates the need for filler materials, fluxes, and shielding gases, significantly reducing the environmental impact of the welding process itself. Its solid-state nature means there are no direct gas emissions during welding, further enhancing its role as a low-impact manufacturing technique. This combination of efficiency and sustainability makes FSW a critical technology in advancing greener aerospace manufacturing [9], [10].

As aerospace manufacturing becomes increasingly complex, **the importance of real-time process monitoring** cannot be overstated. Real-time process monitoring focuses on the manufacturing phase, ensuring that every step of the production process is controlled, monitored, and optimized to prevent defects before they occur. By **integrating advanced sensors and data analytics** into the manufacturing process, companies can detect variations in real-time, allowing for **immediate corrective action, reducing scrap rates, and increasing overall efficiency** [11]. This real-time feedback loop not only enhances product quality but also supports the creation of **digital twins**—virtual models that represent the physical manufacturing process—enabling predictive maintenance and further process optimization [12].

While real-time process monitoring ensures that each manufacturing step is tightly controlled and optimized to prevent defects from occurring, this approach forms the foundation for **Structural Health Monitoring (SHM)** systems, which extend this vigilance into the operational lifespan of aerospace components.SHM systems use **embedded sensors** to **continuously monitor** the health of a structure, detecting early signs of fatigue, damage, or degradation [13]. This approach allows for a shift from traditional, time-based maintenance strategies to **condition-based maintenance**, which can significantly extend the life of a component while reducing downtime and maintenance costs.

A **holistic approach to monitoring** is essential for ensuring product integrity from manufacturing to service. This comprehensive framework involves recording and **analyzing data throughout the entire lifecycle** of a component, starting from the manufacturing process and continuing through its operational life. By implementing this approach, companies can maintain a complete history of each component, enabling a more informed understanding of its performance and longevity. The ability to track a product lifecycle provides numerous advantages, including the early identification of potential issues, optimized maintenance schedules, and an overall increase in safety and reliability. Ensuring consistent quality from the factory floor to the field enhances customer satisfaction while reducing operational risks and costs.

Central to both real-time process monitoring and SHM is the integration of **Non-Destructive Testing (NDT) techniques** and **sensors** specifically developed to assess structural integrity. Among these, **electromagnetic techniques** such as **eddy current testing (ECT)** hold significant promise due to their **high detection speed**, **non-contact** nature, and ability to detect **microstructural changes** [14]. Despite these advantages,

ECT methods remain **underutilized** in real-time process monitoring and SHM application. Current methods, such as fluid penetrant and X-ray inspections, have inherent limitations in terms of automation and speed. ECT offers a more efficient and reliable alternative, with the potential to significantly reduce both production cycle times and maintenance costs.

A **critical area** of development is the **establishment of robust correlations** between ECT signals and the microstructural properties of materials. Achieving this correlation will allow for more accurate and reliable interpretations of sensor data, both during the manufacturing process and throughout the service life of the component. Furthermore, this understanding opens the door to the **application of artificial intelligence (AI)** and **machine learning algorithms**. By leveraging AI, data from real-time monitoring and SHM systems can be processed more efficiently, identifying patterns and predicting failures before they occur. This predictive capability could revolutionize the aerospace industry, leading to smarter, more efficient manufacturing processes and maintenance strategies.

The **motivation** for this research is rooted in addressing the current gaps in knowledge and **application of ECT**, specifically in the context of **real-time process monitoring** and **SHM** of **aerospace welded joints**. By exploring the potential of eddy current sensors and their integration into both manufacturing and service life monitoring frameworks, this research aims to **contribute** to a **more comprehensive** and effective approach to quality assurance in the aerospace sector.

As a result of this investigation, the application of **ECT methods is expanded**, establishing a **stronger correlation** between ECT signals and the microstructural characteristics of welds, thereby enhancing the potential for real-time process monitoring in FSW. Additionally, **two specialized electromagnetic sensors** are developed, capable of detecting weld area reductions in thermoplastic joints, specifically for SHM applications.

1.2 Research Objectives

The main objective of this research is to **investigate** and **advance** the **application of electromagnetic-based monitoring approaches**, specifically ECT and electromagnetic SHM sensor, in manufacturing and structural health monitoring of aerospace structural joints.

The specific objectives of this investigation are:

- **Identifying** critical aerospace structural joint cases where **monitoring ECT techniques are underdeveloped or insufficiently applied**, in order to focus the research on areas with the greatest potential for improvement and relevance to aerospace applications.

- **Establish a robust correlation** between ECT and the microstructural properties of the considered welded joints to facilitate the implementation of ECT for real-time process monitoring applications.

- **Develop electromagnetic sensors** capable of detecting defects and material degradation in welded joints for SHM applications.

- **Evaluate the capabilities and limitations** of selected monitoring techniques for real-time process monitoring and SHM applications, ensuring their suitability and effectiveness for specific aerospace use cases.

1.3 Scientific publications

This section presents the articles that have arisen from this thesis in the form of a compendium of scientific publications and their thematic relation.

The indexed scientific publications summarised in this research are:

Table R 1 Indexed scientific publications

Article #	Reference	Q/IF
1	M. Mazzeschi, K. C. Nuñez, E. Cañibano, and J. C. Merino, "**Monitoring of thermoplastic induction welding defects. Use of electromagnetic properties as a predictive tool**," Struct. Heal. Monit., vol. 22, no. 3, pp. 1–15, 2022, doi: 10.1177/14759217221111979.	Q1/6.6
2	M. Mazzeschi, S. Farhangdoust, E. Cañibano, J. C. Merino, and K. C. Núñez, "**Structural health monitoring of composite laminates in thermoplastic induction welded** joints **using electromagnetic field technique**," Sensors Actuators A Phys., vol. 375, no. May, 2024, doi: 10.1016/j.sna.2024.115540.	Q1/4.1
3	M. Mazzeschi, M. Sanz, J. C. Monge, E. Cañibano, C. P. Rodriguez-Juan, and K. C. Núñez, "**Electrical conductivity field analysis: A prognostic instrument for real time monitoring of friction stir welding process**," *J. Manuf. Process.*, vol. 131, pp. 93–110, 2024, doi: https://doi.org/10.1016/j.jmapro.2024.09.005.	Q1/6.1

The three publications are tightly connected by their focus on evaluating electrical conductivity changes, specifically using the ECT method, to detect defects and microstructural variations in welded joints. **Article 1** primarily focuses on a numerical evaluation of how electromagnetic responses, influenced by conductivity changes, can detect delamination in thermoplastic induction-welded joints. It establishes the groundwork for developing electromagnetic sensors sensitive to structural damage, targeting SHM. **Article 2**, building on the numerical foundation of Article 1, emphasizes experimental analysis by using both magnetic and electric field sensors to measure the effects of induced defects in thermoplastic composites, further reinforcing the potential of conductivity variations for SHM purposes. These first two articles collectively highlight the importance of electrical conductivity as a diagnostic tool for assessing the health of thermoplastic joints throughout their service life.

In contrast, **Article 3** shifts the focus from SHM to real-time process monitoring during manufacturing. This study investigates the relationship between electrical conductivity and microstructural changes in FSW aluminium alloy joints. It demonstrates how ECT can be employed to track process parameters, such as tool rotational speed and travel speed, and their impact on weld quality, providing insights for real-time process

monitoring. Together, these publications create a comprehensive narrative: from numerical simulations and experimental validation in SHM applications to real-time monitoring of the FSW process, all unified by the central role of ECT in evaluating weld integrity through electrical conductivity analysis.

4 non-indexed publications have also been published:

Table R 2 No-indexed scientific publications

Article #	Reference
1P	M. Mazzeschi, K. Nuñez-Carrero, M.T. Fernandez, E. Cañibano, and J. C. Merino, "**Thermoplastic weld fatigue behaviour analysis using structural health monitoring sensors data**," in *Proceedings of MATCOMP21 (2022) and MATCOMP23 (2023)*, 2024, p. Vol. 08.
2P	M. Mazzeschi, A. P. Valbuena, K. C. Nunez, M. Fernandez, E. Canibano, and J. C. Merino, "**Thermoplastic Induction Welded Joint Design for Structural Health Monitoring Damage Detectability**," in *Structural Health Monitoring 2023*, 2023. doi: 10.12783/shm2023/36731.
3P	M. Mazzeschi, E. Cañibano, M. T. Fernandez, and J. C. Merino, "**Técnicas de monitorización de la salud estructural para satélites receptivos**," in *DESEi+d 2023 (X Congreso Nacional de I+D en Defensa y Seguridad)*, 2023.
4P	M. Mazzeschi, S. Farhangdoust, S. Ahmed, E. Cañibano, M. Fernandez, and F. K. Chang, "**Guided-wave structural health monitoring for assessing the bond strength of induction-welded thermoplastic composite joints**," in *SMASIS 2024 (ASME 2024 Conference on Smart Materials, Adaptive Structures and Intelligent Systems)*, 2024.

The results of this investigation have been presented at several national and international congresses, as shown in the following table:

Table R 3 National and International Congresses.

Number	Congress	Contribution
1C	M. Mazzeschi, A.G. Arnáiz, E. Cañibano, J.C. Merino "**Study of electromagnetic characteristics changes due to defects generation in thermoplastic induction welded joint for structural health monitoring application**" ICFC8 - The Eight International Conference on Fatigue of Composites	Oral presentation
2C	M. Mazzeschi, J.C. Merino, E. Cañibano, M.T. Fernandez "**Electromagnetic-based structural health monitoring approach for tracking damage in thermoplastic welded joints**" EWSHM2022 - 10º European Workshop on Structural Health Monitoring	Oral presentation
3C	Mazzeschi, M., Gaton, P., Guerrero, Merino, J. C., Cañibano, E." **Eddy current modeling in thermoplastic welded joints for non-destructive**	Oral presentation

	testing and structural health monitoring application" CNMAT2022 - XVI Congreso nacional de materiales	
4C	M. Mazzeschi, P. Gaton, M. Asensio, K. C. Nunez, E. Cañibano, J. C. Merino, M. Fernández "**Electromagnetic-Based Structural Health Monitoring Approach For Thermoplastic Welded Joints: Experimental and Numerical Analysis**". MATCOMP21 - XIV Congreso nacional de materiales compuestos	Poster*
5C	M. Mazzeschi, A. P. Valbuena, K. C. Nunez, M. Fernandez, E. Canibano, and J. C. Merino, "**Thermoplastic Induction Welded Joint Design for Structural Health Monitoring Damage Detectability**," IWSHM2023 - 14º International Workshop on Structural Health Monitoring	Oral presentation
6C	M. Mazzeschi, K.C. Nuñez, M. Fernandez, E. Cañibano1, J. C. Merino "**Thermoplastic weld fatigue behaviour analysis using structural health monitoring sensors data**," MATCOMP23 - XV Congreso nacional de materiales compuestos	Oral presentation
7C	M. Mazzeschi, E. Cañibano, M. T. Fernandez, and J. C. Merino, "**Técnicas de monitorización de la salud estructural para satélites receptivos**," in *DESEi+d 2023 (X Congreso Nacional de I+D en Defensa y Seguridad)*, 2023.	Oral presentation
8C	M. Mazzeschi, S. Farhangdoust, S. Ahmed, E. Cañibano, M. Fernandez, and F. K. Chang, "**Guided-wave structural health monitoring for assessing the bond strength of induction-welded thermoplastic composite joints**," in *SMASIS 2024 (ASME 2024 Conference on Smart Materials, Adaptive Structures and Intelligent Systems)*, 2024.	Oral presentation

* This work was honored in the form of the **Best Scientific Poster Award** at MATCOMP21 Congress.

Table R 4 below outlines the research stays conducted during the development of this research. The PhD candidate undertook two research stays, with a duration of more than three months, at the Department of Aeronautics and Astronautics at Stanford University (USA), under the supervision of Prof. Fu-Kuo Chang.

The first stay focused on defining the primary objectives of the research project and collaborating closely with the team over the course of one month. After this initial phase, the candidate returned to *Fundación CIDAUT* in Spain to supervise the manufacturing of essential specimens, which were crucial for the data acquisition and subsequent analysis. Following this phase, the researcher returned to Stanford University in August as a Visiting Student Researcher, continuing his experimental work at the Stanford Structures and Composites Laboratory (SACL) through the end of September. This period involved refining the data acquisition and analysis, advancing the project toward its final outcomes with guidance from the Stanford research team.

Table R 4 International Research Stays.

International Research Stays	
1	International Research Stay (1) (1 month**). Structures and Composites Laboratory (SACL)**, Department of Aeronautics and Astronautics, Stanford University, USA – (28/02/2023 – 31/03/2023)
2	International Research Stay (1) (2.5 month**). Structures and Composites Laboratory (SACL)**, Department of Aeronautics and Astronautics, Stanford University, USA – (16/07/2023 – 29/09/2023)

1.4 Novelty of contributions

The key novelties of this research can be summarized as follows:

Development of electromagnetic SHM sensors for thermoplastic induction welded joints:

- This research introduces a novel sensor design capable of measuring both magnetic and electric field variations for monitoring thermoplastic induction welded joints. Unlike prior studies, which utilized existing sensor configurations, the design presented here is unique, offering simplicity while maintaining high sensitivity to damage. This approach improves signal interpretation and streamlines the modelling of sensor behaviour, facilitating a clearer correlation between sensor response and changes in electrical conductivity and dielectric permittivity.

- This work represents the first application of electromagnetic SHM techniques specifically for thermoplastic induction welded joints. It goes beyond detecting signal variations from damage and explores the deeper correlation between sensor response and controlled local variations in electromagnetic properties, enhancing the potential for damage detection and monitoring.

Enhanced understanding of electrical conductivity and microstructural changes in AA6082-T6 aluminium alloy FSW joints:

- This study establishes a robust correlation between electrical conductivity and the microstructural changes induced by varying FSW process parameters. Previous research typically focused on detecting common defects, without a thorough examination of how changes in electrical conductivity reflect metallurgical phenomena in FSW processes.

- This is the first study to investigate the electrical conductivity of AA6082-T6 aluminium alloy FSW joints, using multiple combinations of tool rotational speed (ω) and travel speed (v). This approach provides a comprehensive understanding of how microstructural changes affect conductivity, contributing to improved process monitoring and weld quality control.

1.5 Thesis Outline

The structure of this research is organized to progressively build a comprehensive understanding of the research topic, beginning with a broad overview of existing techniques and narrowing down to the specific contributions of the study. **Chapter 2** outlines the state of the art in NDT, Non-Destructive Evaluation (NDE) and SHM, emphasizing their relevance in structural and manufacturing quality monitoring within aerospace. This chapter also introduces electromagnetic NDT methods, with a particular focus on eddy current probes, and explores the role of welding technologies in aerospace manufacturing. It further discusses the holistic monitoring approach that combines real-time process monitoring and SHM to ensure product integrity throughout its lifecycle. The chapter concludes by presenting case studies that exemplify these monitoring techniques and highlights the specific research contributions. **Chapter 3** delves into the theoretical background underpinning the research, starting with a review of Maxwell's equations and analytical methods, and leading into the electrical properties of composite materials and how microstructural changes affect electrical conductivity in FSW. This theoretical foundation supports the experimental and numerical methods described in the following chapter. In **Chapter 4**, the methodology for both real-time process monitoring and SHM applications is detailed, including the design of eddy current sensors and probes. This chapter presents the materials, test specimens, and experimental setups used in the case studies, and explains how the numerical models were developed. **Chapter 5** presents the results of the experimental and numerical investigations, discussing the findings by citing the published articles while also incorporating additional results that were not included in the papers. This approach allows for a more comprehensive analysis, connecting published work with new experimental insights. **Chapter 6** compiles the author's publications as they were published, ensuring full access to the relevant studies. Finally, **Chapter 7** reflects the key conclusions drawn from the research and outlines potential avenues for future work. This final chapter highlights the broader implications of the findings and suggests directions for further exploration in both real-time process monitoring and SHM applications in aerospace manufacturing.

Chapter 2

2 State of the art

This chapter outlines the current landscape and advancements in NDE and SHM, specifically focusing on process quality and structural health assessment of welding in aluminium alloys and thermoplastics. Moreover, it highlights the knowledge gaps and delineates the research contributions of this investigation. More specifically: Section 2.1, clarifies the roles and development of NDT, NDE, and SHM, emphasizing their significance in maintaining structural integrity. Section 2.2 introduces electromagnetic NDT techniques and explores eddy current testing in depth, discussing various probe designs and their applications. Section 2.3 focuses on the significance of welding in aerospace production, underscoring the importance of FSW and thermoplastic welding. Section 2.4 emphasises the importance of the integration of monitoring techniques across the product lifecycle and presents the current state of the art in NDE and SHM specifically applied to monitoring FSW and thermoplastic welding processes. Section 2.5 highlights the knowledge gaps identified and details the research contributions of this investigation, which focus on selected monitoring cases that address these gaps. Finally, Section 2.6, summarizes the key insights of the all chapter.

2.1 NDT, NDE, and SHM: Evolving Approaches in Structural and Manufacturing Quality Monitoring

In the realm of process quality and structural integrity assessment, it is essential to distinguish between NDT and NDE, as these terms, while often used interchangeably, encompass different scopes of application. NDT refers to a range of techniques used to detect surface and subsurface flaws in materials and components without destroying the part, as opposed to destructive testing [15]. These techniques are commonly employed during manufacturing for quality control and throughout the service life of structures for maintenance purposes, following standardized procedures that leave little room for variation, ensuring consistent application by trained personnel according to established qualification schemes.

On the other hand, NDE represents a broader concept, encompassing not only the flaw detection capabilities of NDT but also the assessment of material properties, stress states, and overall performance over time. NDE techniques provide quantitative data that enable the evaluation of structural health, prediction of future performance, and estimation of remaining life [16]. Thus, NDE is not limited to periodic inspections but includes a more comprehensive approach to understanding the condition of a structure.

NDT techniques are diverse, each built on distinct physical principles, and have proven effective in various stages of product management and in-service inspection. The most relevant NDT methods include:

- Ultrasonic Testing (UT) [17]
- Acoustic Emission (AE) [18]
- Infrared Thermography (IRT) [19]
- Eddy Current Testing (ECT) [20]

- X-ray Radiography (XR) [21]
- Visual Inspection (VI) [22]
- Magnetic Particle Inspection (MPI) [23]
- Liquid Penetrant Inspection (LPI) [24]

Although NDE relies on a variety of NDT techniques to detect, quantify, and localize damage in structures, as well as to estimate their remaining lifespan, an equally important approach to achieving these objectives is the emerging field of Structural Health Monitoring (SHM). SHM shares the same fundamental goals as NDE but differs in its methodology. SHM is defined as the continuous or periodic assessment of a structure condition through sensors that are permanently attached to the material, enabling real-time or near-real-time monitoring [13], [25]. This on-board, in-service capability allows for ongoing assessment of a structure condition, facilitating more informed maintenance decisions and enhancing safety. It is important to note that the majority of SHM techniques have evolved from traditional NDT methods, specifically tailored for the continuous monitoring of structures in service. The adaptation of these techniques for SHM has been driven by the need for real-time data in critical applications, particularly in fields like aerospace, where safety and reliability are paramount.

It is important to note, however, that while on-board sensors are central to SHM, the integration of periodic NDT inspection data can also be valuable. Combining these data sources can significantly improve the accuracy of damage prognosis and prediction, offering a more comprehensive understanding of the structural health over time [26].

As SHM gains prominence, particularly for its ability to provide continuous, real-time monitoring, significant advancements have been made in developing sensors specifically designed for integration with materials and structures. These sensors aim to enhance detection, location, and characterization capabilities while addressing challenges such as power consumption, system weight, installation complexity, and data analysis [27]. Key SHM sensors include:

- Accelerometers [28]
- Piezoelectric Sensors [29]
- Fiber Optic Sensors [30]
- Microelectromechanical Systems (MEMS) [31]
- Eddy Current Sensors [20]
- Capacitive Sensors [32]
- Comparative Vacuum Monitoring (CVM) Sensors [33]
- Strain Gauges [34]

The integration of multiple sensor types is often necessary for comprehensive SHM, with each sensor contributing to a broader system capable of detecting, locating, quantifying, and classifying damage. Further details on the various SHM methodologies and their applications can be found in Section 2.4.2.

2.2 Introduction to Electromagnetic NDT methods

Electromagnetic Non-Destructive Testing (EM-NDT) encompasses a range of techniques that utilize electric currents, magnetic fields, or a combination of both to evaluate the integrity of materials and structures [35]. These methods detect and analyse

distortions in the electromagnetic response caused by the presence of defects, all without damaging the test object. According to this definition, techniques such as infrared thermography, optical methods, and X-ray could also be considered EM-NDT, as they involve the use of electromagnetic waves across different parts of the spectrum. Nevertheless, EM-NDT is commonly understood to refer specifically to electromagnetic-based non-destructive testing methods within the radio-frequency range, also known as *radio frequency NDT* [36]. In this dissertation, the term is used in this context. These techniques offer rapid, contact-free inspection capabilities suitable for automated processes, making them particularly valuable in industrial applications.

Figure 1 provided offers an overview of various EM-NDT methods, detailing their operating frequency ranges and suitability for ferromagnetic, non-ferromagnetic, and dielectric materials.

For ferromagnetic materials, EM-NDT methods typically involve inducing a magnetic field and observing disturbances caused by defects. The primary techniques include **Magnetic Flux Leakage (MFL)** [37], which detects leakage fields created when a ferromagnetic material is magnetized, revealing flaws, and **Magnetic Particle Inspection (MPI)** [23], which uses magnetic particles applied to a magnetized surface to highlight surface and near-surface defects. Additional methods like **Permanent Magnetic Perturbation (PMP)** [38], **Magnetic Barkhausen Noise (MBN)** [39], and **Metal Magnetic Memory (MMM)** [40] focus on detecting disturbances in the magnetic field or material memory to identify stress points and defects. PMP works by applying a permanent magnetic field to the material and then monitoring changes in this field caused by defects or material inhomogeneities [23]. MBN detects noise signals generated by sudden, localized changes in magnetization when a material is subjected to an external magnetic field [39]. These noise signals are correlated with the presence of stress, microstructural anomalies, or defects. MMM, on the other hand, relies on the natural magnetic memory of ferromagnetic materials, which retains information about stress and deformation. This method detects variations in the magnetic field that have occurred over the material history, which can point to areas of potential failure or damage [40].

Pulsed Eddy Current Testing (PEC) operates by inducing transient eddy currents into a conductive material using a pulse of electromagnetic energy [41]. These currents diffuse through the material, and their decay is monitored over time. Variations in the decay curve can indicate the presence of defects, changes in material properties, or variations in thickness. PEC is suitable for detecting flaws and corrosion in ferrous materials like carbon steel and cast iron. It can also be used for non-ferromagnetic materials such as aluminum alloys, although its effectiveness may be limited compared to ferrous materials [42].

These techniques leverage the high magnetic permeability of ferromagnetic materials, which enhances their effectiveness. For non-ferromagnetic and dielectric materials, these methods are less effective due to their low magnetic permeability, which limits their sensitivity and accuracy, making them unsuitable for such materials.

Given that the current investigation focuses on aluminum alloys and CFRP, which fall into the non-ferromagnetic category, these methods were excluded from consideration.

Ground Penetrating Radar (GPR) [43] and **Time Domain Reflectometry (TDR)** [44]are specialized electromagnetic techniques with applications that differ significantly from the focus of this research. GPR, which uses high-frequency electromagnetic waves to image subsurface structures, is commonly employed for inspecting reinforced concrete,

bridges, and underground utilities [43]. TDR, on the other hand, sends a pulse along a transmission line to detect impedance changes, making it useful for monitoring the integrity of cables and locating faults in hidden or underground installations [44]. Given their distinct applications, these methods were not considered relevant to the scope of this research.

To evaluate the applicability of the remaining EM-NDT techniques, an assessment of their operational principles and effectiveness was conducted to identify a method that offers a balanced tradeoff among the following criteria:

- Suitability for aluminum alloys
- Suitability for CFRP
- Real-Time process monitoring capability
- SHM sensor integration potential

Table 1 provides a summary of this analysis, presenting a comparative overview of each technique based on these key factors.

ECT operates on the principle of electromagnetic induction. When an alternating current passes through a coil, it generates a fluctuating magnetic field. When this coil is brought near a conductive material, such as aluminum alloy or CFRP, the magnetic field induces circulating currents (eddy currents) within the material [14]. These eddy currents generate their own magnetic fields, which can be detected and analyzed to identify variations caused by defects, such as cracks or corrosion. ECT is well-suited for detecting defects in aluminum alloys because of its sensitivity to changes in electrical conductivity, which is characteristic of these materials. Similarly, it is applicable to CFRP composites, where it can identify surface and near-surface flaws despite the composite insulating nature [45]. ECT ability to provide real-time monitoring is supported by its rapid response to changes in electromagnetic fields, making it valuable for process control [20]. Furthermore, its compatibility with small, lightweight sensors enables effective integration into SHM systems [46].

The **Alternating Current Potential Difference (ACPD)** method involves applying an AC to the surface of the material through electrodes. As the current flows through the material, any defects or discontinuities cause variations in the local potential difference. These variations are measured using voltage sensors positioned at different locations on the material surface. By analyzing these potential differences, ACPD can identify and map defects such as cracks or voids [47]. **Direct Current Potential Difference (DCPD)** operates similarly to ACPD but uses a direct current (DC) instead of AC. DCPD is effective in detecting and locating surface and near-surface defects by measuring these changes in potential. ACPD and DCPD are effective for aluminum alloys due to their sensitivity to changes in potential caused by defects.

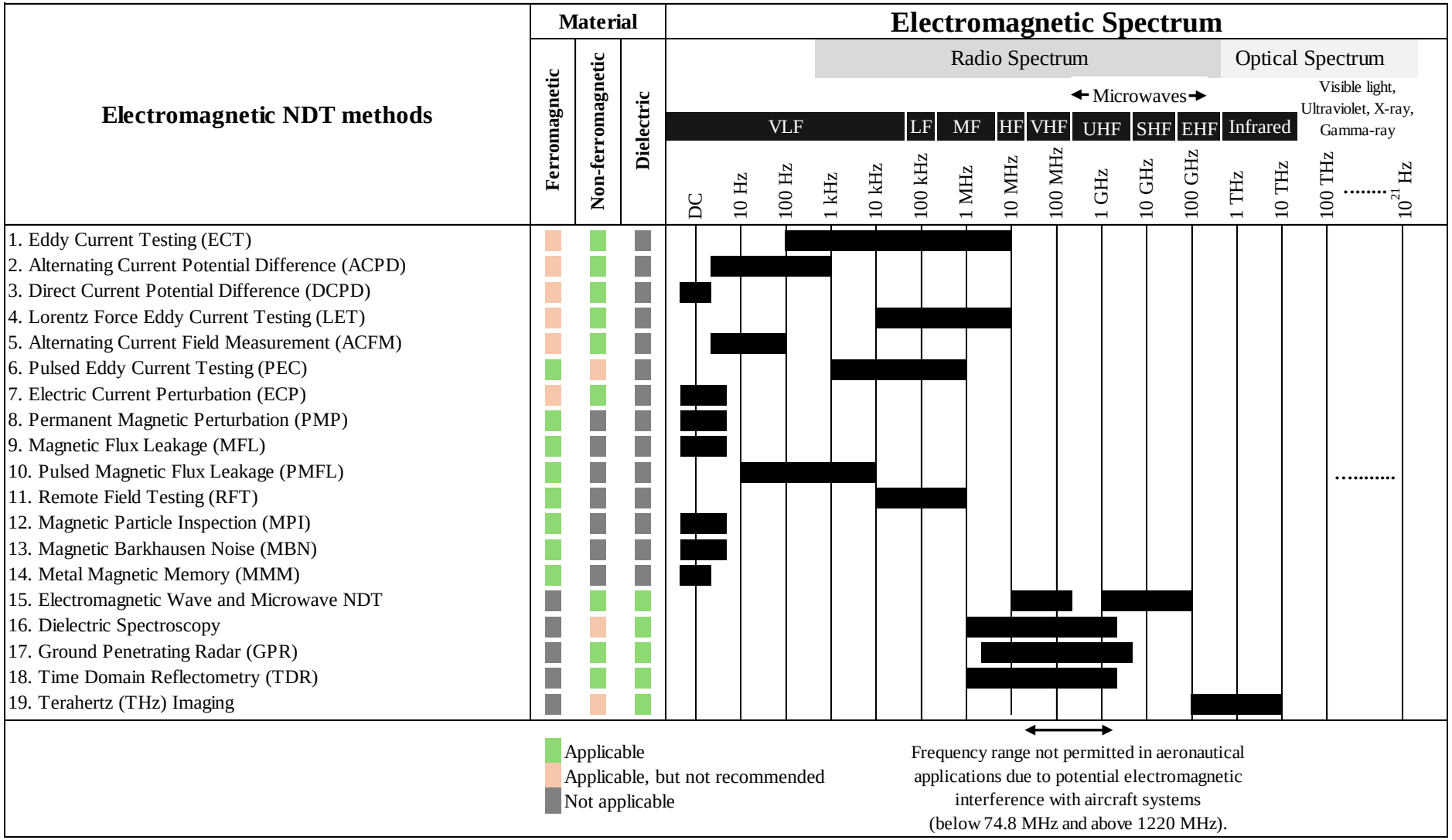

Figure 1 Overview of Electromagnetic NDT methods: operating frequency ranges and suitability for ferromagnetic, non-ferromagnetic, and dielectric materials.

Table 1 Comparison of EM-NDT methods considering their effectiveness in inspection of aluminum alloys and CFRP and evaluating their capability for real time process monitoring and SHM applications.

EM-NDT Technique	Aluminium Alloys Suitability	CFRP Suitability	Real-Time Monitoring	SHM Sensor Integration
Eddy Current Testing (ECT)	✓	✓	✓	✓
Alternating Current Potential Difference (ACPD)	✓	✗	✗	✓
Direct Current Potential Difference (DCPD)	✓	✗	✗	✓
Lorentz Force Eddy Current Testing (LET)	✓	✓	✓	✗
Alternating Current Field Measurement (ACFM)	✓	✗	✗	✗
Electric Current Perturbation (ECP)	✓	✗	✗	✓
Electromagnetic Wave and Microwave NDT	✓	✓	✗	✓
Dielectric Spectroscopy	✗	✓	✗	✗
Terahertz (THz) Imaging	✗	✓	✗	✗

However, these techniques are less suited for CFRP due to the composite low electrical conductivity, which limits their effectiveness . ACPD and DCPD require the introduction of current into the material, which compromises the advantage of contact-free methods and can introduce complications for a real-time process monitoring implementation [48].

In **Lorentz Force Eddy Current Testing (LET)**, an electrically conductive specimen is subjected to a constant magnetic field while it is in relative motion [49]. This interaction generates an electromagnetic field that induces eddy currents within the material. When these eddy currents interact with defects or discontinuities, they produce a Lorentz force that causes a measurable displacement or vibration in the material . This displacement is detected and analyzed to identify the presence, location, and severity of defects [50]. LET is highly effective for aluminum alloys due to its ability to detect both surface and subsurface defects, making it suitable for inspecting this conductive material. Neverthless, it is less effective for CFRP composites, which are non-conductive and do not support significant eddy currents [50]. While LET supports real-time process monitoring through its rapid response to material changes, its use in SHM is constrained by the need for relative motion between the sensor and the material. This requirement limits its feasibility for integration into SHM systems where attached sensors are needed [49].

Alternating Current Field Measurement (ACFM) detects surface and near-surface defects by inducing an alternating current in a probe, which creates a magnetic field around the inspected material [51]. Disturbances in this field, caused by defects, are measured through changes in the probe impedance. ACFM is effective for large ferromagnetic and no-ferromagnetic components, especially with coatings, but is less suitable for short sections, small items, and less conductive materials like CFRP [51]. Its design for periodic inspections rather than continuous monitoring makes it unsuitable for real-time process monitoring and SHM applications.

Electric Current Perturbation (ECP) works by injecting an electric current into the material under examination and detecting localized perturbations in the magnetic flux associated with the current flow around defects such as cracks or inclusions [52]. While this method is effective for detecting defects and variations in the properties of aluminum alloys, its performance in CFRP is less robust, although it can still identify in-plane

waviness and other imperfections [53]. A significant disadvantage of ECP is its reliance on a contact-based approach to introduce current into the material, which can limit its application in real-time process monitoring. ECP has the potential to be effectively integrated into sensor networks for continuous SHM, as demonstrated by similar methods [54].

All of the aforementioned techniques operate predominantly within the frequency range below a few MHz, where inductive phenomena are dominant. However, in the higher frequency range of 10 MHz to 10 THz, other methods emerge where electromagnetic wave propagation plays a more significant role. **Dielectric Spectroscopy** involves measuring a material dielectric properties across various frequencies by applying an external electric field and observing the material response [55]. This technique is less effective for highly conductive metals like aluminum alloys, as their conductivity interferes with the measurement process [55]. **Terahertz (THz) Imaging**, which uses terahertz radiation to produce images of a material internal structure, is non-destructive and capable of penetrating certain materials, making it suitable for inspecting CFRP and other composites [56]. Nevertheless, its application to metals like aluminum alloys is limited due to their high reflectivity and absorption of terahertz radiation [57]. Both Dielectric Spectroscopy and Terahertz Imaging present challenges in terms of complexity and method development, which hinders their suitability for real-time process monitoring and complicate sensor miniaturization for integration into SHM applications.

Electromagnetic Wave and Microwave NDT techniques utilize antenna-based systems to transmit and receive microwave signals. This method involves a transmitter antenna that emits microwave signals and a receiver antenna that detects the reflected or transmitted waves after they interact with the material [58]. These microwaves can penetrate aluminum alloys and CFRP, allowing for the detection of variations such as delaminations, voids, and other defects within these materials [59]. While effective for both aluminum alloys and CFRP, the practical implementation of these techniques for real-time monitoring is challenging due to issues related to antenna integration and electromagnetic interference in industrial environments. In the context of SHM, some methods have explored the possibility of embedding a receiving antenna within CFRP structures while using an external antenna for inspection [60]. Nevertheless, this approach is limited as the excitation can only be performed with the external antenna at specific intervals, such as during ground inspections of aircraft and continuous SHM is impeded because the structure cannot be interrogated during flights. Another work explored damage evaluation in CFRP plates using a non-contact electromagnetic sensor with coupled spiral inductors [61]. This sensor detects subsurface defects by measuring transmission coefficients, enhanced by the addition of ferrite layers and a new ferrite yoke design, improving sensitivity by up to 57%. This development indicates potential for real-time SHM applications, though it has yet to be validated with actual defects on structures during operational conditions.

In summary, **ECT** emerges as the most balanced technique, demonstrating exceptional suitability for both aluminum alloys and CFRP. Its capability for effective real-time monitoring and seamless integration into SHM systems makes it the optimal choice for addressing the present research.

In the following section, a comprehensive review of eddy current probes is presented.

2.2.1 Eddy current probes overview

ECT operates on the principle of electromagnetic induction, as described by Faraday's law. When an alternating current flows through a coil, it generates a time-varying magnetic field, concentrated primarily at the coil centre (**Figure 2**). This magnetic field, in the context of ECT, can be considered quasi-static at lower frequencies, where induction phenomena dominate. As the coil approaches an electrically conductive, non-ferromagnetic material, this magnetic field induces circular eddy currents within the material. These currents generate a secondary magnetic field that opposes the primary field, leading to a change in the coil impedance [14].

However, at higher excitation frequencies, particularly in the range of 1 to 10 MHz, the behaviour of the system begins to change. While the inductive phenomena remain significant, there is also the onset of power transmission from the coil in the form of electromagnetic waves. This effect, though more pronounced at frequencies above 10 MHz, can still influence measurements depending on the characteristic size of the object under test respect to the wavelength of the propagating radiation [58]. Thus, the ECT response is influenced not only by the material properties but also by the interplay between inductive and radiative effects as frequency increases. By analysing the variation in the coil impedance, valuable information about the material conductivity, composition, and geometry can be extracted.

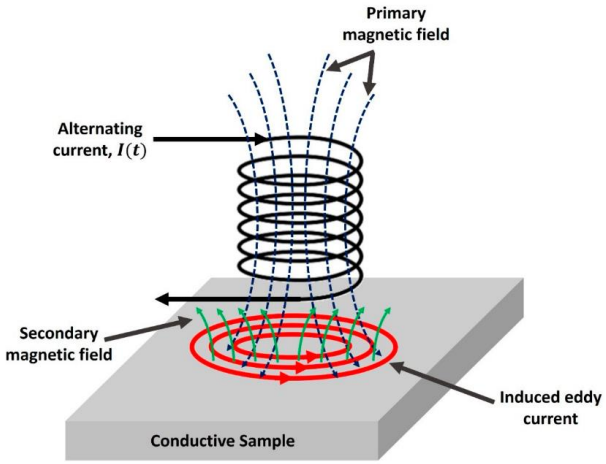

Figure 2 Schematic representation of eddy current working principle showing coil-induced eddy currents, primary and secondary magnetic fields [58].

To measure variations in magnetic fields, various types of magnetic sensors are available, including solenoid coil probes, superconducting quantum interference devices (SQUIDs), Hall-effect sensors, and magnetoresistive sensors. Among these, coil probes are the most widely used in ECT due to their versatility and effectiveness [14].

Absolute probes (**Figure 3 (a)**), the simplest type, consist of a single coil that both generates eddy currents and senses changes in the resulting eddy current field. These probes are effective for detecting long flaws or gradual dimensional variations that may not be detected by differential probes. Beyond crack detection, absolute probes provide valuable information about the test material, including grain size, hardness, and stress levels.

Differential probes (**Figure 3 (b)**), in contrast, employ two coils that compare adjacent sections of the material. These coils are wound in opposite directions to cancel out the voltages induced by the primary magnetic field, allowing them to detect small discontinuities with high sensitivity. Nevertheless, differential probes are less effective at identifying gradual variations in dimensions or composition because of the proximity of the coils.

EC probes can also be classified based on their function: double-function probes and separate-function probes. Double-function probes use the same coil or set of coils to generate eddy currents and to receive the secondary field generated by those currents. Separate-function probes (**Figure 3 (c)**), however, employ different coils for excitation and detection. This separation allows for optimized coil design, with primary coils adjusted to produce a strong and uniform magnetic field and secondary coils fine-tuned to maximize the detection of the secondary field while minimizing noise.

Additionally, double-function probes can be further categorized based on the position of the pick-up coils. The conventional method (**Figure 3 (d)**), which is the most common, positions the exciting and pick-up coils on the same side of the inspected material. The transmission method (**Figure 3 (e)**), typically used in separate-function probes, places the pick-up coil on the opposite side of the magnetic source. This transmission method requires the material under inspection to have a thickness of no more than 3–5 times the standard penetration depth to effectively receive the signal on the opposite side.

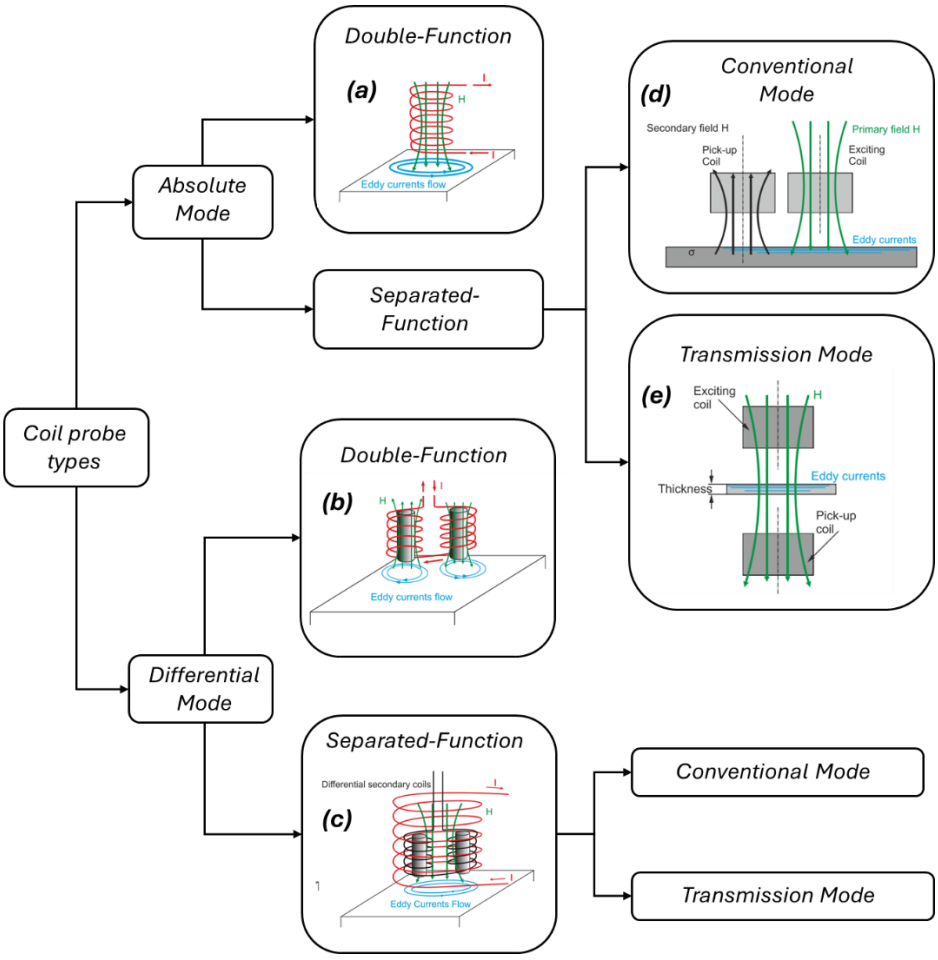

Figure 3 Overview of coil probe configurations for Eddy Current Testing (Figures adapted from [14])

To systematically evaluate the current research landscape, the probes identified in the literature were classified into two main categories:

1. 3D probes and
2. surface-mounted or planar probes.

This classification was guided by the intended end applications, specifically focusing on the suitability of these probes for real-time process monitoring and their potential for integration into structures for embedded SHM applications. Surface-mounted or planar probes, in this context, refer to eddy current probes that possess a planar geometry, making them suitable for attachment directly to the surface of the material under test. These probes are designed to conform to the material surface, ensuring close proximity and consistent interaction with the test object. Even in cases where these probes have not been explicitly attached to the surface in existing research, their flat, planar design inherently lends itself to such applications, including potential embedding within the material for continuous monitoring. This contrasts with probes having a three-dimensional (3D) geometry, which are primarily utilized in scenarios where the probe must maintain a certain distance from the material, such as in manual or robotic inspections.

Given the broad range of applications for eddy current probes, this analysis has been specifically focused on their use in welding inspection and in CFRP assessment.

The application of ECT in welded joints and composite structures is well-documented in the research literature. As indicated in **Table 2**, various studies have explored the potential of ECT for inspecting FSW joints and CFRP materials.

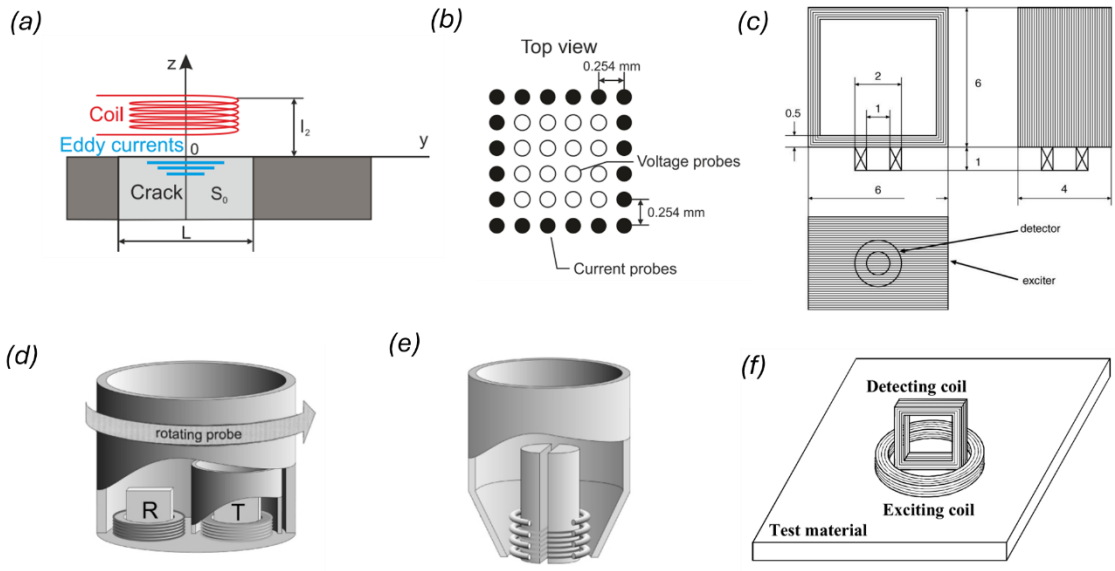

Figure 4 Common 3D eddy current probe designs: (a) pancake coil [14], (b) array of pancake coils [14], (c) uniform eddy current probe [62]. 3D probes employed for CFRP inspection: (d) rotating probe [63], (e) static differential probe [63], and (f) theta probe [64].

Figure 4 illustrates some relevant 3D probe types and designs commonly used for these applications. 3D geometry probes often use absolute configurations due to their high sensitivity in detecting subtle variations in the material under test. Pancake-type coils, one of the most widely used designs, have their axis perpendicular to the surface of the

test piece, making them particularly suitable for inspecting flat surfaces. As shown in **Figure 4 (a)**, the eddy currents generated in the test piece form concentric circles parallel to the surface. When a penetrating crack or defect is present, the eddy current flow is disrupted, allowing for the detection of surface and subsurface flaws. Differential probes are less commonly used, as they are typically better suited for identifying small, localized defects but are less effective at detecting gradual material variations. The use of dual-function or separate-function probes, which either combine the excitation and receiving functions in the same coil or separate them into distinct coils, is also widespread, allowing for optimized coil design. Separate-function probes are advantageous in NDT since they allow more precise control over the magnetic field generation and sensing processes.

In welded joints, the primary focus has been on detecting common defects such as lack of penetration, kissing bonds, root micro-defects, cavities, and tunnel defects.

McNab et al. [65] employed an array of pancake-type coils (**Figure 4 (b)**) to inspect friction stir welded joints, demonstrating the technique effectiveness in detecting subsurface defects such as cavities and tunnel defects. Another notable contribution comes from Yusa et al. [62], who developed a uniform eddy current probe (**Figure 4 (c)**) that produced a highly homogeneous magnetic field. This approach increased the sensitivity of the system in detecting uniform defects like lack of penetration and kissing bonds.

In the context of CFRP materials, the challenges differ due to the anisotropic conductivity of the material. The main focus in CFRP inspections has been on identifying fiber orientation, local imperfections, delamination, and impact damages. For instance, Mook et al. [63] utilized a rotating absolute probe (**Figure 4 (d)**) and a static differential probe (**Figure 4 (e)**) to inspect CFRP components, detecting changes in fiber orientation and delamination effectively. Koyama et al. [64] proposed a specialized theta probe (**Figure 4 (f)**), optimized for CFRP anisotropic conductivity, which was highly sensitive in detecting impact damage. This tailored approach addressed the unique electrical properties of CFRP, enabling a more effective inspection of composite materials.

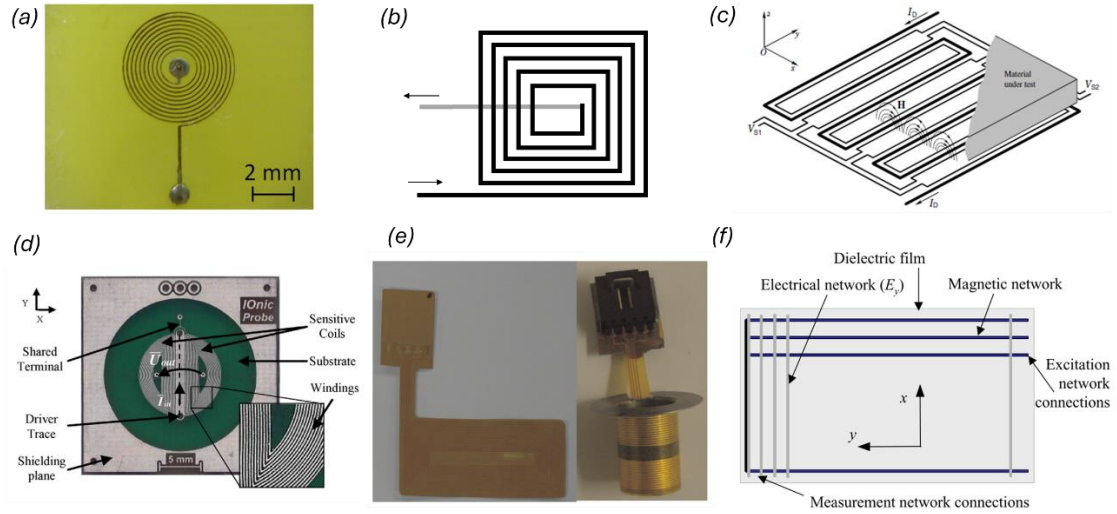

Figure 5 Examples of planar eddy current probes: from simple geometries to advanced sensing solutions — (a) Spiral [66], (b) Planar Rectangular, (c) Meandering Coils [67], (d) IOnic Probe [68], (e) Flexible EC Sensing Films for Bolt-Hole Edge Crack Detection [69], (f) HELP Layer®-1 [70].

Table 2 Literature review of ECT in welded joints and CFRP structures.

Authors	Kind of analysis	Type of sample	Probe geometry	Probe Type	Probe Configuration	Key Findings
McNab et al. [65]	Cracks detection	Mild steel welds	3D	Array of pancake type coils	Absolute - Double function	The eddy current array effectively detected cracks in mild steel welds, including in the heat-affected zone, with a high probability of detection even with lift-off variations
Sorger et al. [71]	Electrical conductivity	- FSW of Ti6Al4V, Cu, Pb and S355 steel - GTAW of AISI 304 stainless steel.	3D	Pancake type probe	Absolute - Double function	Electrical conductivity measurements provided better resolution of microstructural changes in friction stir processed and welded materials compared to hardness tests.
Yusa et al. [62]	Fatigue cracks detection	Inconel weld	3D	Uniform eddy current probe	Absolute - Separated function	Eddy current testing was highly effective in detecting and sizing fatigue cracks in Inconel weld overlays, outperforming other methods like potential drop and ultrasonic testing.
Postolache et al. [72]	Weld defect (not specified)	Welded joint (material not mentioned)	3D	Pancake type probe	Absolute - Separated function	The eddy current probe, combined with image processing, successfully localized and estimated weld defects, but future work is needed for online detection and improving image quality.
Cheng et al. [73]	Fatigue cracks detection	Inconel weld	3D	Pancake type probe	Absolute - Double function	Eddy current testing accurately detected and sized surface-breaking cracks in Inconel welds, validating its effectiveness compared to other methods.
Mook et al. [63]	Fibre orientation, local imperfection, delamination, impact damages	CFRP laminates	3D	Rotating absolute probe and static differential probe	Absolute and Differential - Separated function	Eddy current methods characterized CFRP for defects like delamination and fiber orientation, with high-frequency sensors providing detailed structural insights.
Grimberg et al. [74]	Fibre orientation	CFRP laminates	3D	Eddy current focused micro transducer	Absolute - Separated function	A focused micro-eddy current sensor effectively visualized successive layers of carbon fibers in composites, aiding in the assessment of fiber integrity.

Table 2 (continued)

Gros et al. [75]	Delamination	CFRP laminates	3D	Probe type not mentioned	Absolute - Double function	Eddy current testing accurately detected and quantified delamination in CFRP, showing potential for in-service monitoring despite limitations in signal-to-noise ratio.
Koyama et al. [64]	Impact damage	CFRP laminates	3D	Eddy current theta probe	Absolute - Separated function	The eddy current theta probe, optimized for CFRP anisotropic conductivity, effectively detected impact damage with a high signal-to-noise ratio.
Dmitriev et al. [76]	Cracks and cavities	Aluminum-magnesium alloy FSW joints	3D	Pancake type probe	Absolute - Separated function	A subminiaturized eddy current system detected small defects in FSW joints of aluminum-magnesium alloys, demonstrating high accuracy and efficiency.
Ishkov et al. [77]	Cracks and cavities	Aluminum-magnesium alloy FSW joints	3D	Pancake type probe	Absolute - Double function	The developed eddy current system detected ultra-small defects in FSW joints of aluminum-magnesium alloys with high accuracy, proving its suitability for quality assessment.
Lamarre et al. [78]	Kissing bonds defect	Aluminum alloy FSW joints (Specific aluminum alloy not specified)	3D	Array of pancake type coils	Absolute and Differential - Separated function	Eddy current arrays successfully detected kissing bonds in aluminum alloy FSW joints, though more data is needed for comprehensive evaluation.
Bhat et al. [79]	Lack of penetration, kissing bonds, cavities and tunnel defects	AA2219 FSW joints	3D	Pancake type probe	Absolute - Separated function	Eddy current testing was effective in detecting various FSW discontinuities in AA2219, with comparisons made to other NDE methods.
Chen et al. [80]	Fibre orientation and various damages	CFRP laminates	3D	Pancake type probe	Absolute - Separated function	A low-frequency eddy current system successfully detected surface and near-surface defects in CFRP, demonstrating high sensitivity to fiber orientation and damages.
Mizukami et al. [81]	Delamination	CFRP laminates	Planar	Rectangular	Absolute - Separated function	A flexible eddy current coil sheet detected delamination in CFRP through temperature differences, using a statistical diagnosis method for clearer defect identification.

Table 2 (continued)

Yamada et al. [82]	Cracks detection	Copper plate	Planar	Meandering	Absolute - Separated function	The planar meander-mesh coil provided detailed imaging of metallic defects, aiding in the inference of defect geometry and orientation.
Fava et al. [83]	Electrical conductivity assessment	Zircaloy-4 plate	Planar	Rectangular	Absolute - Separated function	Planar rectangular coils showed high sensitivity to conductivity changes in Zircaloy-4, useful for inspecting complex surfaces with shallow imperfections.
Rakow et al. [69]	Cracks in a bolt hole	6061-T6 aluminium alloy	Planar	Rectangular & Meandering	Absolute - Separated function	The SHM fastener system, integrating an eddy current sensor film, successfully monitored fatigue crack growth in aluminum alloy joints in situ.
Ding et al. [84]	Fatigue cracks	2A12-T4 aluminum alloy	Planar	Rosette EC	Absolute - Separated function	The rosette eddy current sensor achieved quantitative fatigue crack monitoring in aluminum alloys with high precision, demonstrating real-time monitoring capability.
Xie et al. [85]	Fatigue cracks	7075 aluminum alloy	Planar	Sensor array	Absolute - Separated function	A novel flexible planar eddy current sensor array effectively detected and sized microcracks in aluminum alloy, showing high spatial resolution and accuracy.
Jiao et al. [86]	Cracks in a fastener hole	2A12-T4 aluminium alloy	Planar	Rosette EC	Absolute - Separated function	The micro eddy current sensor accurately monitored fatigue cracks in aluminum alloys with high resolution, even in corrosive environments.
Chen et al. [87]	Fatigue crack	Welded structure (material not reported)	Planar	Rectangural sensor array	Absolute - Separated function	The high-sensitivity flexible eddy current array sensor significantly improved crack detection in welded structures, with minimal influence from stress and temperature.
Chen et al. [88]	Cracks in a bolt hole	Material not reported	Planar	Rosette EC	Absolute - Separated function	A new rosette-like eddy current array sensor was developed, showing improved sensitivity in detecting fatigue-induced defects around bolt holes compared to traditional sensors.
Sun et al. [89]	Cracks in a bolt hole	2024-T351 aluminum alloy	Planar	Rectangular	Absolute - Separated function	The embedded eddy current sensing film quantified crack parameters in aluminum bolted joints, effectively tracking crack propagation.

Table 2 (continued)

Liu et al. [46]	Cracks in a bolt hole	CFRP laminates	Planar	Rectangular	Absolute - Separated function	The eddy current sensor network effectively identified and quantified hole-edge damages in CFRP bolted joints, demonstrating potential for SHM applications.
Song et al. [90]	Cracks in a fastener hole	2024-T351 aluminum aluminium alloy	Planar	Rosette EC	Absolute - Separated function	Flexible eddy current array sensors demonstrated high durability and effectiveness in monitoring fatigue cracks in aluminum alloys, even under harsh environmental conditions.
Rosado et al. [91]	Root defects	AA2024-T531 FSW joints	Planar	IOnic Probe	Diferential - Separated function	A planar differential eddy current probe, optimized for FSW joint inspection, successfully detected root defects with high spatial discrimination.
Santos et al. [66]	Root micro defects	AA6013 and AA7075 alloys FSW joints	Planar	IOnic Probe	Diferential - Separated function	An innovative eddy current probe detected and sized micro-defects in the root of FSW joints with high accuracy, showing lift-off independence.
Goldfine et al. [92]	Bolt holes inpection	Material not reported	Planar	MWM-Rosettes	Absolute - Separated function	MWM-Rosettes effectively monitored subsurface cracks in bolt holes, demonstrating high durability and long-term monitoring capability.
Goldfine et al. [93]	Lack of penetration	Friction stir welded joints (material not reported)	Planar	MWM-Arrays	Absolute - Separated function	The MWM-Array demonstrated high sensitivity in detecting lack-of-penetration defects in FSW joints, correlating well with microstructural changes.
Goldfine et al. [94]	CFRP disbond/delamination monitoring	CFRP laminates	Planar	MWM-Arrays	Absolute - Separated function	MWM-Arrays successfully monitored disbond growth in CFRP, though matrix damage detection was limited.
Lemistre et al. [95]	Delaminations and burning	CFRP laminates	Planar	HELP Layer	Absolute - Separated function	The HELP-Layer system detected and characterized both mechanical and thermal/chemical damages in CFRP, proposing a dual SHM approach with electromagnetic and piezoelectric sensors.

Planar probes, as illustrated in **Figure 5**, are gaining attention, particularly SHM applications, because their geometry allows for surface attachment or embedding within materials. These probes typically employ absolute configurations to ensure the highest sensitivity and separate-function configuration is the most encountered. The rationale behind this choice lies in the ability to separately optimize the design of the excitation and sensing coils. The most common geometries for planar eddy current probes include spiral (**Figure 5 (a)**), planar rectangular (**Figure 5 (b)**), and meandering coils (**Figure 5 (c)**).

Santos et al. [66] explored electrical conductivity in FSW of AA6013-T4 and AA7075-T6 aluminium alloys using a spiral planar eddy current probe. The study investigated the correlation between electrical conductivity and microstructural changes, with conductivity varying significantly with depth. This correlation was also aligned with hardness variations, suggesting that electrical conductivity could provide a non-destructive means to assess weld integrity. In a separate study, Rosado et al. [68] focused on optimizing the geometry of a differential planar eddy current probe, called the IOnic probe (**Figure 5 (d)**), to enhance its non-destructive testing capabilities. Through finite element modelling and experimental validation, adjustments in the probe geometrical parameters significantly improved its sensitivity and spatial resolution.

In SHM applications, planar probes have demonstrated their effectiveness in detecting damage propagation and structural changes, offering a non-invasive monitoring approach. For surface-mounted or planar probes, especially in metallic structures, flexible ECT sensing films have been proposed to monitor fatigue cracks. Eddy Current Foil Sensors (ECFS) were tested in the root joint area during Airbus A380 full-scale fatigue test [96], while Rakow and Chang [69] developed flexible EC sensing films to detect bolt-hole edge cracks and monitor propagation (**Figure 5 (e)**). The same approach was improved by Chen et al. [88] who proposed an innovative rosette-like ECT array sensor to boost sensitivity around bolt holes, detecting fatigue-induced defects with increased precision. Such research works demonstrate the flexibility of ECT probes for monitoring weld integrity and fatigue crack propagation.

In composite materials like CFRP, the low electrical conductivity presents challenges for ECT, but several innovations have proven effective. The Meandering Winding Magnetometer Array (MWMTM-Array), developed by JENTEK Sensors, has shown sensitivity to conductivity changes in adhesive-bonded CFRP T-joints, though matrix damage remains difficult to detect [94]. Liu et al. [46] developed an eddy current array sensing film to monitor damage around the hole-edge of composite bolted joints, demonstrating localized damage detection in composite structures. ONERA's work [95] further advances this field by integrating electromagnetic imaging into components, offering an innovative approach to both localization and visualization of defects within CFRP materials. ONERA developed an innovative sensor network, called HELP Layer®-1 (**Figure 5 (f)**), designed for electromagnetic health monitoring in composite structures. This sensor features two orthogonal wire networks printed onto a flexible substrate only 100 microns thick. Distinctively, one network is short-circuited at one end, functioning as induction loops, while the other remains open-circuited, acting as a network of capacitances sensitive to electric fields. This configuration allows the HELP Layer®-1 to effectively detect and visualize structural defects by interacting with both magnetic and electric field variations.

Across these diverse ECT probe configurations and applications, the presence of an excitation coil or network, combined with a passive sensing coil or electrodes, remains a common feature. These elements enable the detection of changes in the material magnetic or electric fields, facilitating the identification of structural defects, regardless of the specific sensor design or material under inspection.

2.2.2 Benefits and Challenges

Considering the insights garnered from previous sections, it is evident that ECT offers several compelling benefits for NDE and SHM. ECT is distinguished by its **non-invasive, contact-free approach**, allowing for the detection of subtle variations in material properties without physical contact, a feature especially valuable for real-time process monitoring applications. ECT demonstrates a **strong capability** for identifying **various types of defects** in welded joints, including fatigue cracks, porosities, and even minute micro-cracks. Additionally, by monitoring changes in electrical conductivity, ECT can effectively **track various kinds of damage** that may occur over a structure operational life, making it particularly valuable for SHM applications. This includes detecting impact damage and burns caused by lightning strikes—issues that are especially critical for CFRP structures despite their inherently low electrical conductivity. Such capabilities make ECT a versatile tool for assessing structural integrity across a range of conditions and materials.

Furthermore, the integration of ECT with Artificial Intelligence (AI) opens up significant opportunities. By employing **physics-based machine learning algorithms**, the interpretative power of ECT can be significantly enhanced, linking empirical data with theoretical models to provide a comprehensive view of material conditions.

Nevertheless, ECT also introduces **complexities in signal interpretation** that necessitate **robust correlations** between probe signals and the material characteristics they reflect. These correlations are crucial for a deeper understanding of material behaviours under various manufacturing processes. The challenge lies in extending the application of ECT beyond mere defect detection to provide a profound understanding of the underlying material science. This expanded application not only enhances the utility of ECT in industrial settings but also contributes significantly to the scientific community's ability to develop targeted solutions for material testing and evaluation.

2.3 Welding in Aerospace Manufacturing

Welding stands as one of the cornerstones of aerospace manufacturing, playing a pivotal role in the construction of aircraft structures and components. Its significance lies not only in the assembly process but also in the optimization of crucial factors such as weight, structural integrity, and performance.

Traditional joining methods, such as riveting, have historically been favoured for their simplicity and reliability. However, rivets, constituting a substantial portion of the overall structural assembly, can represent up to 10% of the aircraft total weight [97], particularly in certain aircraft configurations. Thus, the reduction in the use of riveting methods promises a substantial weight reduction, thus facilitating significant progress towards achieving optimal weight reduction in aerospace structures. Moreover, welding provides continuous load paths and superior fatigue resistance, enhancing the overall structural integrity and performance of the aircraft [98]. Although these benefits, conventional welding processes face several challenges, such as achieving high-quality welds with

sensitive alloys, managing distortion in thin materials, and maintaining productivity amidst a skilled labour shortage [99]. These issues necessitate advanced welding technologies and meticulous process control to meet stringent aerospace standards. To address these challenges, a variety of advanced welding techniques have been developed, including TIG, MIG, friction stir, laser, and resistance welding [99]–[102]. Therefore, a thorough evaluation of the materials to be joined is crucial in selecting the most appropriate welding technique, ensuring optimal performance, compliance with industry codes, and maximizing the benefits of weight reduction and structural integrity.

Aerospace Materials

In this section, aerospace materials are defined as structural materials that bear the loads exerted on various airframe components during flight operations. These materials are essential for maintaining the safety and integrity of critical airframe parts, from the wings and fuselage to the empennage and landing gear of aircraft. They also fortify the fuselage, tail boom, and rotor blades of helicopters, as well as the airframe, skins, and thermal insulation tiles of spacecraft like the space shuttle. Beyond airframes, aerospace materials extend to the jet engines, where they are pivotal in components such as turbine blades, generating the thrust that propels aircraft through the skies.

Aerospace engineers have access to an extraordinarily diverse array of materials for constructing aircraft. It is estimated that they can choose from over 120 different materials for airframe and engine construction, including more than 65,000 types of metals, 15,000 types of plastics, 10,000 types of ceramics, as well as numerous composites [99]. However, the stringent demands of the aerospace industry for materials to be lightweight, structurally efficient, damage-tolerant, and durable—while also being cost-effective and easy to manufacture—exclude the majority from aerospace applications. It is estimated that fewer than one hundred types of metal alloys, composites, polymers, and ceramics meet the essential combination of properties required for aerospace use.

Figure 6 illustrates the types and quantities of structural materials used in various modern civil and military aircraft. A notable feature across different aircraft types is the reliance on a core set of materials: aluminium, titanium, steel, and composites. While the weight percentages of these materials vary among aircraft, they collectively make up over 80-90% of the total weight. High-strength aluminium alloy is the most prevalent due to its exceptional properties: it is lightweight, offers good stiffness, strength, and fracture toughness, is cost-effective, and can be easily fabricated into complex structural components. This versatility and performance make aluminium a cornerstone of modern aircraft construction. Titanium is another important material extensively studied and widely used in aerospace applications. Recent research and technological advancements have significantly enhanced its strength and performance. Titanium alloys offer a high strength-to-weight ratio, excellent corrosion resistance, high temperature resistance, superior fatigue resistance, and crack resistance, making them ideal for critical aerospace components [103].

Nevertheless, over the past five decades, the use of high-performance Fibre-Reinforced Polymer (FRP) composites in aircraft structures has grown steadily. Alongside aluminium, CFRP have become a key ingredient in the construction of aircraft and helicopter airframes. CFRPs offer the advantage of being lighter and stronger than aluminium alloys; however, they are also more expensive and more susceptible to impact damage [104], [105]. Despite their benefits, the high cost of composite components has

slowed their adoption in the aerospace sector compared to similar metal structures. As a result, **it is expected that metals and FRP composites will continue to coexist** in many airframe applications, balancing performance, cost, and durability[106].

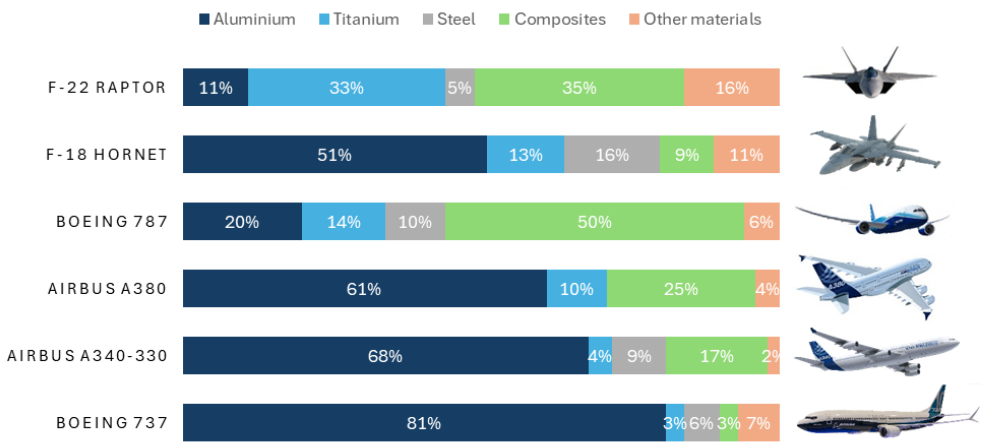

Figure 6 Structural materials and weight percentage used in civil and military aircraft (percentage data from [99], [104], [106], [107]).

FRP fall into two primary categories based on the differences in matrix characteristics: thermoplastic and thermoset. The most commonly used composites are thermosets, of which those based on epoxy resins account for around thirty eight billion dollars in 2023 [108]. However, in recent years, Thermoplastic Composites (TPCs) have attracted increasing interest in the aerospace industry due to their numerous advantages over traditional thermoset composites. One of the primary benefits of TPCs is their cost-effective manufacturing processes, which can significantly reduce production costs. Additionally, TPCs offer substantial environmental advantages, including lower energy requirements during manufacturing and improved recyclability. The distinctive feature of thermoplastic matrices, which can be melted and reshaped multiple times without significant loss of physical properties, allows for the use of fusion bonding techniques. This capability not only enhances manufacturing efficiency but also potentially reduces the weight of aircraft by eliminating the need for fasteners and adhesives.

Welding techniques: Friction Stir Welding

Advancements in welding technology, particularly in the development of new welding methods, have significantly enhanced the weldability of materials used in engineering applications. This progress underscores the growing importance of welding technology in various industries.
Several challenges must be addressed when welding aluminium alloys:

- **Oxide Formation:** Aluminium forms a tenacious oxide layer that can inhibit weld quality. Proper surface preparation and the use of appropriate shielding gases are essential.
- **Thermal Conductivity:** Aluminium high thermal conductivity requires careful heat management to prevent warping and ensure uniform welds.
- **Porosity:** Controlling weld pool contamination and employing advanced welding techniques can mitigate porosity issues.

- **Cracking:** Proper alloy selection, preheating, and post-weld treatments help reduce the risk of hot cracking and ensure durable joints.

FSW has emerged as a solution for welding aluminium alloys, including those that are challenging or impossible to weld with conventional methods such as arc welding. For example, non-weldable aluminium alloy 7075 can be successfully joined using FSW, a solid-state welding method.
Currently, FSW is commercially employed in various industries , including shipbuilding [109], [110], high-speed train manufacturing [109], [111], and the aviation sector [109], [112]. In this method, the plates to be welded are clamped together in a butt or overlap configuration, and a stirring tool with suitable geometry moves along the joint line. Unlike conventional friction welding, where pieces are moved over each other, FSW uses a rotating tool that is plunged into the clamped plates, causing friction.
The FSW process can be summarized in three steps (see **Figure 7**):

1. **Tool Approach:** The highly rotating tool approaches the components to be joined. The rotation speed of the tool (ω) and the travel speed along the joint (v) are critical process parameters that influence the amount of heat generated and the material flow. Tool tilt angle and the plunge depth, which control the contact pressure between the tool and the material, influence the degree of plastic deformation and have an impact on defect-free joint formation. These parameters determine the frictional heat and the degree of plasticization in the material, essential for creating a strong weld.
2. **Plastic Deformation:** Heat generated by the friction between the rotating tool and the material softens the material, leading to plastic deformation at the joint interface. This plasticized material flows around the tool, allowing the formation of a solid-state bond without melting the material.
3. **Weld Formation:** As the tool moves along the joint line, the frictional heat and plasticized material facilitate the formation of the welded joint. The stirred material behind the tool consolidates to form a defect-free, continuous weld. The final weld quality is highly dependent on the careful balance of the FSW process parameters, including tool geometry, ω and v.

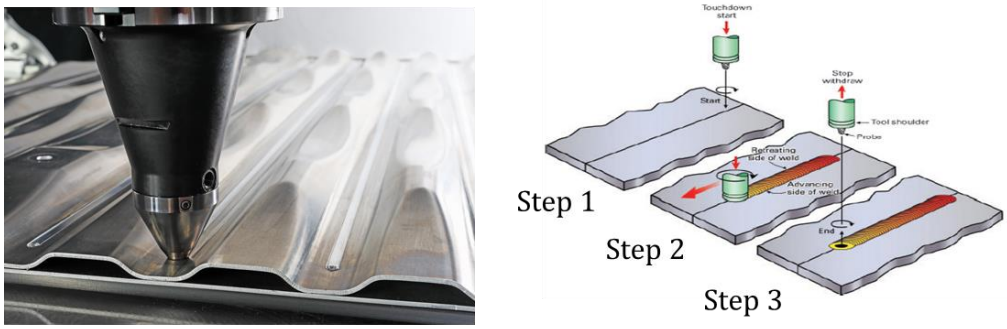

Figure 7 Main steps of the FSW process (Photo from [113]; Process steps adapted from [114]).

Currently, FSW is extensively used in the industrial manufacturing of ships, airplanes, space shuttles, trains, and other vehicles for various applications, including butt-, lap-, and spot-welding of aluminium alloys (**Figure 8**). Intensive research is ongoing to expand the applicability of FSW to join dissimilar aluminium alloys and aluminium alloys with other materials, such as magnesium alloys [101], [115]. Advancements in friction stir butt- and spot-welding, particularly in dissimilar combinations, promise to enable mass

production of lightweight transportation systems, leading to significant reductions in fuel consumption [116].

Figure 8 Illustration of FSW applications across various sectors. (a) Aviation: Eclipse 550 aircraft, utilizing FSW for 128 meters of welding, replacing 60% of traditional rivets [117]; (b) Space: Hydrogen tank for the Ariane 6 upper stage [118]; (c) Automotive: Battery trays for electric vehicles [119]; (d) Naval: Floor panels of large high-speed vessels [120].

Relative to the use of FSW for FRPs, it is an area of active research, focusing on adapting this technique for thermoplastic composites. Recent studies aim to optimize process parameters and tool designs to improve joint quality and mechanical properties [121]–[124]. FSW potential to create high-strength, defect-free welds in FRPs without additional adhesives or fasteners highlights its promise for aerospace and automotive applications, contributing to lightweight, high-performance structures. Despite its potential, FSW of FRPs remains in the early stages of development, with significant advancements needed before it can be widely adopted in aerospace and automotive applications [125].

Welding techniques: Thermoplastic welding

A variety of techniques are available for welding TPCs as shown in **Figure 9**.

Among these, three techniques stand out as the most promising for TPC welding: resistance, ultrasonic, and induction welding:

1. **Resistance Welding**: This technique involves placing an electrically resistive element between the surfaces to be welded. Heat is generated by Joule's Law when an electric current passes through the element, causing the matrix to melt. Upon cooling under pressure, a weld is formed. An example setup is illustrated in **Figure 10 (a)**.
2. **Ultrasonic Welding**: In this process, a sonotrode vibrates the materials to be welded using a piezoelectric element. As depicted in **Figure 10 (b)**, a sequential ultrasonic spot welding setup generates high-frequency stresses that heat the

material. The heat is produced at the weld interface through friction and hysteresis by appropriately designing the components.

3. **Induction Welding**: This method uses an alternating voltage across a conductive coil to create a time-variable magnetic field. According to Faraday's Law, eddy currents induced in a conductor placed within this magnetic field encounter resistance, generating heat. Pressure can then be applied during or after heating to complete the weld. An induction welding setup is shown in **Figure 10 (c)**.

These techniques are recognized for their efficiency and effectiveness in welding TPCs, providing promising solutions for various industrial applications.

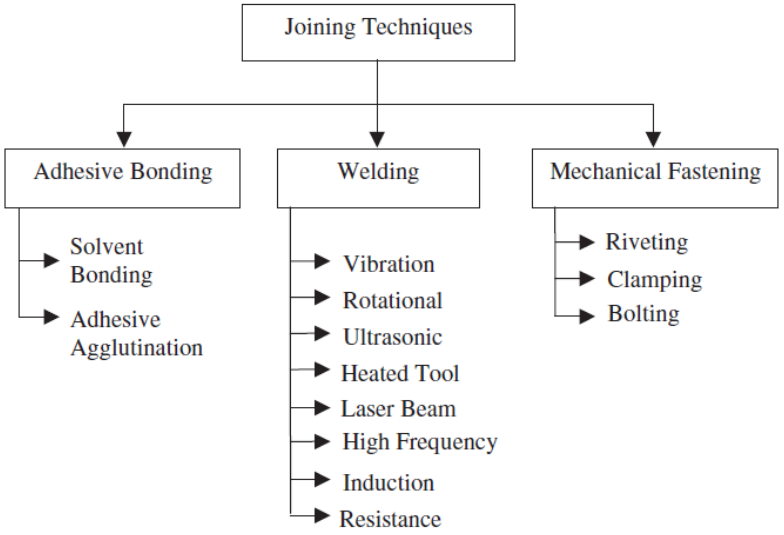

Figure 9 Diagram of the different joining techniques for thermoplastic composites [126].

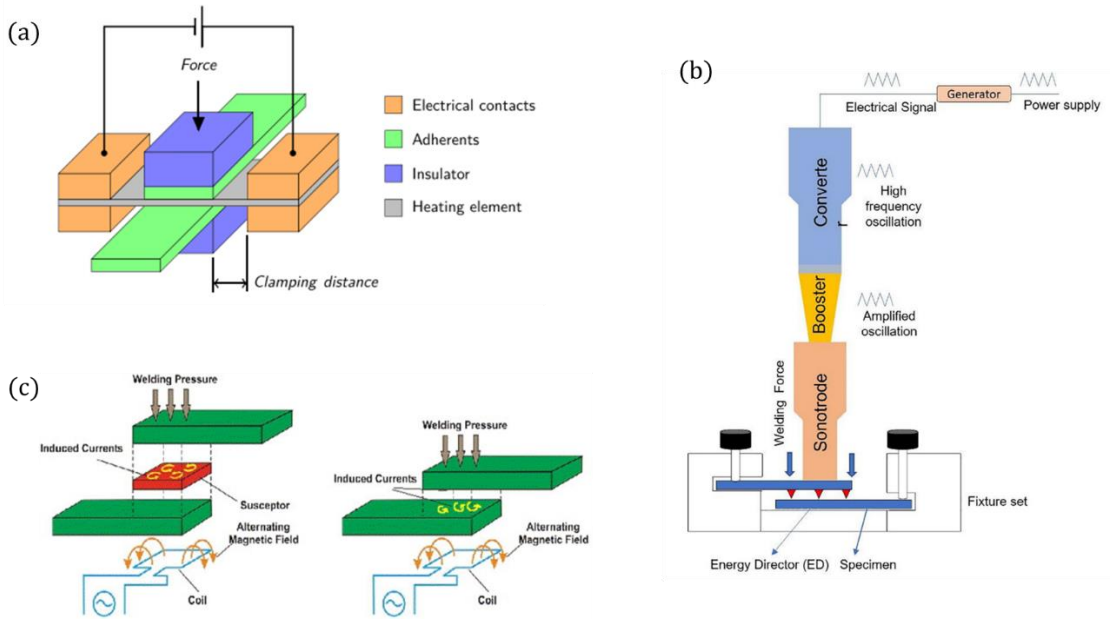

Figure 10 (a) Resistance welding [127], (b) ultrasonic welding [128] and (c) induction welding [129].

One of the most interesting aspects of induction welding is that it requires no contact between the coil and the workpiece and is suitable for welding complex structures and re-opening the welds for repair or part replacement.

Large-scale applications have also been successfully implemented using induction welding with reduced assembly time such as the elevators and rudders of Gulfstream G650 [4] and the Dassault Falcon 5X business jet and the rudder for Boeing Phantom Eye UAV (**Figure 11**).

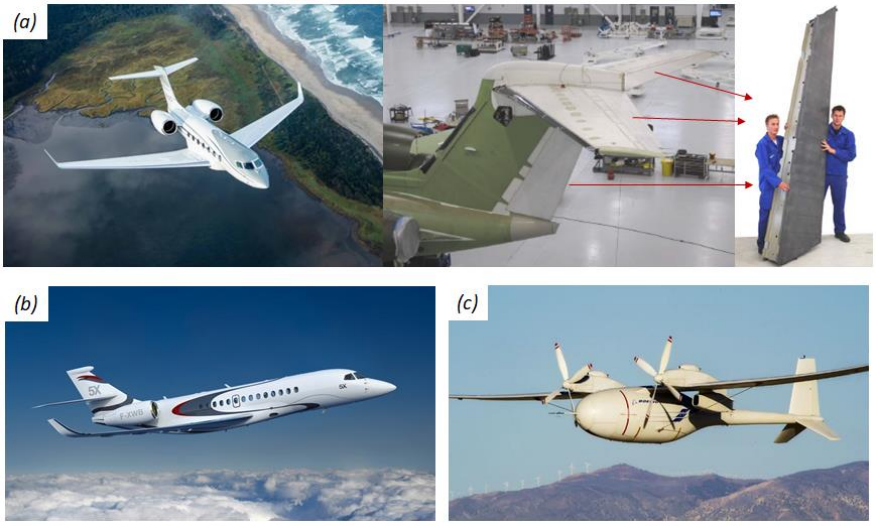

Figure 11 (a) Gulfstream G650 induction welded rudder and elevators [130], [131], (b) Dassault Falcon 5X [132] and (c) Boeing Phantom Eye UAV [133].

The material properties define where and how the heat is produced and if the material is sufficiently conductive it is possible to generate heat in the bond line without the need for a heating element (called susceptor), which in many cases is not desirable having the potential to weaken the mechanical strength of the bond. On the other hand, heating element used as insert in the weld can provide heat exactly where is needed and thermal stress accumulation is prevented in other areas of the workpiece. Moreover, susceptors are mandatory to make possible the induction welding of dielectric composites such as Glass Fiber Reinforced Polymers (GFRP). The main types of susceptors come in the form of a powder dispersed in the thermoplastic resin to form nanoparticles-loaded films and metal mesh. High susceptibility to an electromagnetic field, enough electrical resistance to produce heat and the tendency to form a conductive closed-loop network are important requirements that maximize their function.

The monitoring methodologies investigated in this research need to be validated on components and assemblies that are relevant to the aerospace sector, and for this reason, **FSW and Thermoplastic Induction Welding were chosen as reference methods.** These advanced welding techniques are highly relevant and promising for the aerospace sector due to their alignment with industry needs and recent technological advancements. FSW is renowned for producing high-strength, lightweight joints with minimal defects, which is essential for aerospace where material integrity and weight reduction are paramount. Its ability to weld dissimilar materials, such as aluminium and magnesium alloys, further demonstrates its relevance to the aerospace industry, continuously seeking to optimize performance through advanced material combinations.

Thermoplastic Induction Welding complements the industry growing reliance on thermoplastic composites. This method provides cost-effective, rapid processing while maintaining the essential material properties for aerospace components. Additionally, its potential to enable fusion bonding, eliminating the need for fasteners and adhesives, represents a significant advancement in manufacturing efficiency and weight reduction. Both welding techniques align with the aerospace sector goals for sustainable, high-performance, and cost-effective manufacturing, supported by ongoing research and industrial adoption, making them highly relevant for future aerospace applications.

2.4 Holistic Monitoring for Product Integrity Across Lifecycle

Ensuring product integrity throughout its lifecycle requires a comprehensive approach to monitoring at every stage, from design to disposal (**Figure 12**). This holistic monitoring framework encompasses both manufacturing and service life phases. During **manufacturing**, process and product monitoring are critical to maintaining quality and consistency, identifying inefficiencies, and minimizing defects. This ensures that each product meets the required standards before reaching the market [134], [135]. Once the product is **in service**, continuous conditions and health monitoring become essential to guarantee safety and operability. By tracking performance and detecting potential issues early, this approach helps in extending the product lifespan and enhancing customer satisfaction [136].

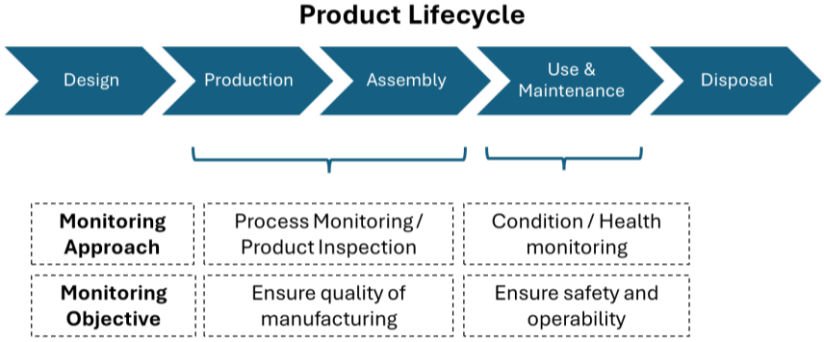

Figure 12 Product lifecycle stages and monitoring approaches.

2.4.1 Real Time Process Monitoring

In the manufacturing phase, the approach to inspection and monitoring can significantly impact overall efficiency and quality costs. In general, product inspection is relegated to the final component inspection (**Figure 13**), which often becomes the bottleneck of the process [134]. When process drifts occur during certain manufacturing operations, defective parts are generated and remain unnoticed until the final inspection. This typically results in high quality costs and increased workload for the Material Review Board (MRB). The MRB, consisting of quality and engineering members, must review, evaluate, and determine the proper disposition of nonconforming material. They decide whether the nonconforming material should be reworked, repaired, or scrapped and implement corrective actions.

Two possible approaches are seen as effective ways of ensuring a high-quality product with low manufacturing costs:

- **In-Process Inspection** (**Figure 13**). By inspecting products at different stages of production, defects can be identified and corrected early, preventing the build-up of defective parts. In this way, quality standards are maintained throughout the production cycle, resulting in more consistent and reliable products. This allows earlier detection of process drift and more timely corrective action, reducing the rate of production of poor quality parts. The availability of NDT and dimensional inspection results at an earlier stage enables a more proactive response to manufacturing problems, improving overall process control and quality [137].

- **Real-Time Process Monitoring** (**Figure 13**). Real-time process monitoring continuously collects, transmits, and analyzes data from various production stages with minimal latency. This technique uses sensor data to provide immediate feedback on process outputs, enabling quick detection of anomalies and immediate corrective actions. Key features include continuous data acquisition, immediate insights, low latency, and enhanced efficiency. Benefits include minimized operational costs due to early issue detection, consistent product quality through continuous monitoring, and increased confidence in process performance and product quality. This approach significantly reduces defects and the need for post-production inspection and rework [135].

The monitoring methods can be traditionally classified into two categories namely, **indirect** and **direct** [11].

Indirect means of monitoring sense physical quantities of machines such as current, power, force, torque, vibration etc. Although these methods are economical and practically more suitable for industrial use, they present the limitation of being less accurate respect to the direct ones. Moreover, a strong effort is required to build a robust correlation between the collected signal and the quality of the manufactured part.

Direct methods utilize NDT techniques, including optical, laser and camera vision, to directly assess the quality of produced components by detecting defects. Despite challenges like the need for a vibration-free environment and delicate handling, these methods offer high accuracy. Recent advancements in the NDT field have underscored their potential to enable real-time process control and certify components during production, potentially eliminating the need for end-of-process inspections.

Table 3 outlines various monitoring techniques employed for real-time process monitoring of **FSW**. The main NDT techniques found in literature are machine vision systems, Acoustic Emission (AE), Phased Array Ultrasonic Inspection (PAUT) and strain-based methods using fiber optic sensors. These methods were primarily used for detecting surface defects, gap defects, and analyzing weld regions.

Application of Digital Image Processing (DIP) techniques to FSW is mainly confined to the classification of defective and defect-free welds FSW [138]–[141] and they face the main limitations that are able to detect only surface defects. AE methods involve detecting transient elastic waves produced when a material undergoes irreversible internal changes [142]. AE monitoring offers a valuable approach for detecting and analyzing welding defects.

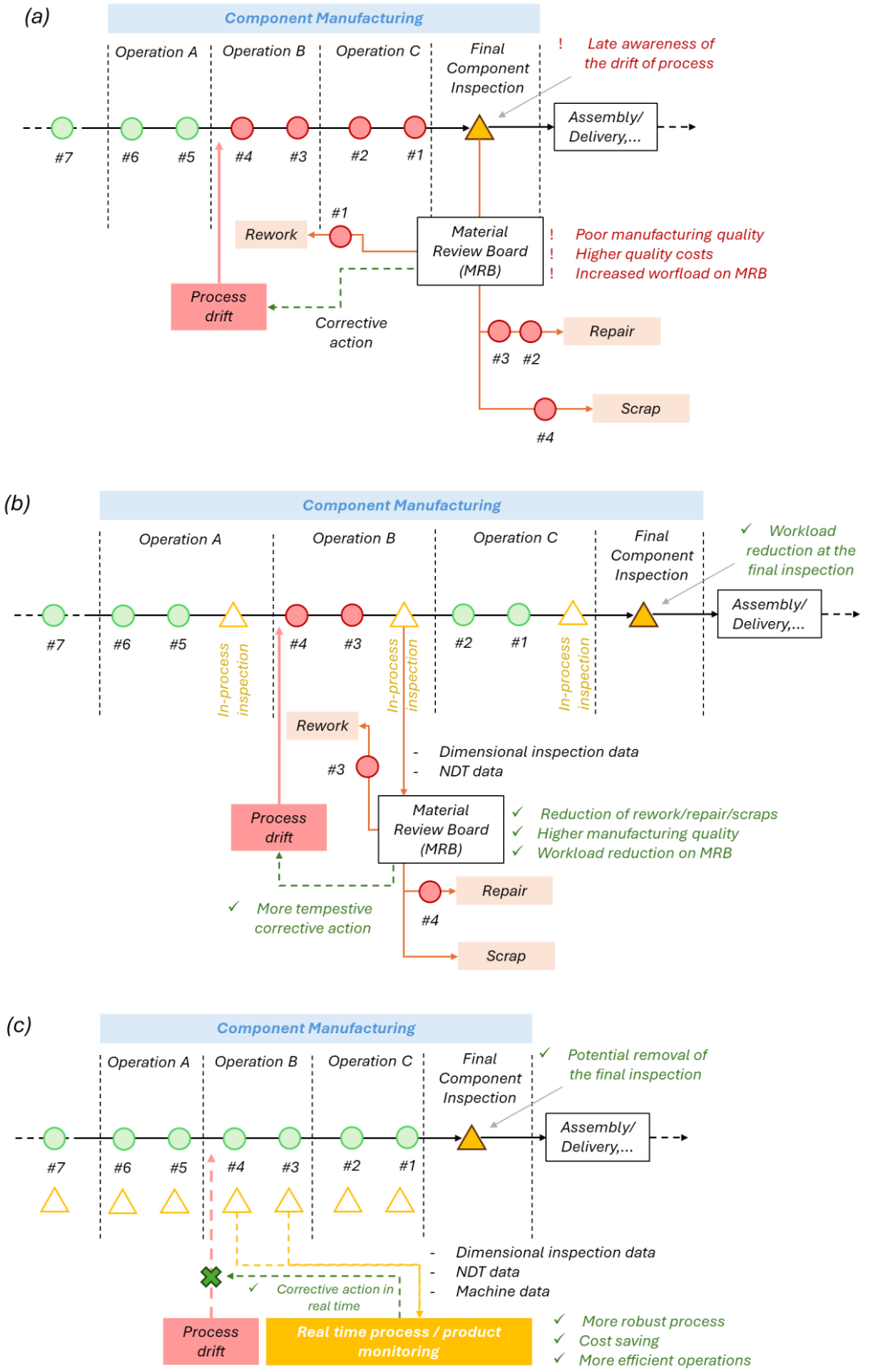

Figure 13 (a) Schematic representation of a conventional manufacturing process where inspections are performed only at the end, highlighting the challenges of detecting process drifts late in the production cycle. (b) Illustration of an enhanced process quality approach through the introduction of intermediate in-process inspections, which facilitates earlier detection of process drifts and enables prompt corrective actions. (c) Real-time process monitoring model that provides immediate process control and enhances the overall robustness of the manufacturing process.

Nevertheless, real-time monitoring and control of the FSW process using AE data presents a significant challenge due to the high computational demands associated with processing large volumes of data [11].

Kleiner and Bird [143] used a PAUT system to assess the quality of welds in 7xxx series aluminium alloy, helping to determine if the welds were properly forged. PAUT works by using multiple ultrasonic elements to create and control the direction of ultrasonic beams, allowing for detailed imaging and inspection of welds and materials. PAUT offers detailed inspection capabilities but comes with challenges, including the complexity of system management and the need to carefully select scanning parameters such as focal distance, inspection angle, and scan pattern, which may need adjustment based on defect location.

Strain-based methods using fibre optic sensors have also been employed for FSW monitoring. Richter-Trummer et al. [144] demonstrated the utility of these sensors in tracking both transient and residual strains during FSW processes, providing valuable insights into weld behaviour and process optimization. Bento et al. [145] further explored the integration of Bragg sensors in hybrid FSW welds, showing their effectiveness in continuous deformation monitoring and enhancing the assessment of weld quality. However, fibre optic sensors face limitations such as durability under high temperatures, complex data interpretation, and high implementation costs, which restrict their broader industrial adoption.

The main indirect methods employed for FSW monitoring used machine signals of vertical and horizontal tool forces, torque, and current signals from spindle and feed motors. These methods show good correlation with various weld defects and mechanical properties but rely heavily on trained neural networks, requiring extensive training datasets and specific welding parameters [146].

According to the author's effort, the use of indirect methods for monitoring the **thermoplastic induction welding process** was not found in literature. Current studies predominantly focus on direct methods such as thermography and fibre optic sensors (see **Table 4**). Flora et al. [147], [148] presented a novel real-time thermography system for composite welding, utilizing an undamaged baseline approach. The system efficiently detects alterations and defects during the welding process, leveraging infrared active thermography inspections. Nevertheless, the effectiveness of this technique can be limited by the inhomogeneity of the heat field and the need for customization for specific parts and materials. These factors may hinder the system performance and accuracy, particularly in complex welding scenarios where uniform heat distribution is challenging to achieve.

Fiber optic sensors have also been explored for monitoring thermoplastic induction welding, as demonstrated by Rahim et al [149], who developed a customized fiber optic sensor designed for permanent installation within a part to provide quicker feedback during fusion bonding processes. This sensor has shown promise in effectively monitoring temperature changes in real-time. However, it has not yet been validated for detecting defective cases within the weld. Additionally, the intrusive nature of fiber optic sensors, being embedded within the welded zone, could potentially impact the structural performance of the material, which may pose challenges for their application in certain scenarios.

Table 3 Monitoring methods found in literature and employed for real time process monitoring of FSW.

Monitoring method	Signal origin	Signal	Remarks	Limitations
Direct	NDT probe	Machine Vision System	Employed for classifying the defective and defect-free welds in FSW [138]–[141].	Only surface defects can be detected.
		Acoustic Emission (AE)	AE signals have been applied to detect gap defects [150] and to evaluate the impact of different tool pin profiles on process performance [151]–[153]. AE monitoring has the potential to be an effective method for identifying and analysing welding defects, providing critical insights into the FSW of dissimilar aluminium alloys [154].	Real-time monitoring and control of the FSW process using AE data is challenging, primarily due to the significant computational demands required to process large volumes of data.
		Phased Array Ultrasonic Inspection (PAUT)	The ultrasonic noise distribution was analysed and correlated with different weld regions [143].	Inspection with PAUT has certain limitations, including the complexity of operating the system and selecting appropriate scanning parameters, such as focal distance, inspection angle, and scan pattern. Additionally, these parameters may need to be adjusted during the inspection, as defects are not always confined to a specific location.
		Strain-based Methods by Fibre Optic Sensor (FOS)	Fiber Bragg Grating (FBG) sensors have been employed in monitoring strain and temperature during the welding process [144], [145]. Transient and residual strains were evaluated enabling precise control over the welding parameters and improving weld quality [145].	The integration of FBG sensors into the welding environment requires careful consideration of sensor placement and protection against the harsh conditions of the welding process, such as high temperatures and mechanical stress, which could affect the sensors' accuracy and durability. Moreover, FBG sensors face challenges relative to data interpretation in in complex welding scenarios and high implementation costs.

Table 3 (continued)

Indirect	FSW machine sensors	Vertical and horizontal FSW tool force and torque	Good correlation between extracted signal features and various weld defects such as surface [155], [156], gap [157] and wormhole defect [158], [159].	Most of these approaches rely on trained neural networks (NN) that can deliver precise defect predictions. However, they require extensive training datasets and are limited to inspecting welds that match the specific welding parameters and equipment used during the training process.
		Current signals from spindle motor and feed motor	The RMS of the current signal demonstrates a strong correlation with both ultimate tensile strength (UTS) and yield strength (YS), though the precision of these predictions has not been detailed [160], [161].	

Table 4 Monitoring methods found in literature and employed for real time process monitoring of thermoplastic induction welding process.

Signal origin	**Monitored physical quantity**	**Remarks**	**Limitations**
Thermographic camera	Temperature	The proposed thermography-based technique effectively detects defects in real-time during the induction welding of thermoplastic composites [147], [148].	The technique effectiveness can be hindered by the inhomogeneity of the heat field and the need for customization for specific parts and materials.
Fibre Optic Sensor		A customized fibre optic sensor was developed for permanent installation within a part with the aim to offer quicker feedback during fusion bonding processes. While the sensor has demonstrated its capability to monitor temperature, it has not yet been validated for detecting defective cases [149], [162]	Intrusive nature of fibre optic sensors: as embedded within the welded zone, it could impact the structural performance of the material.

2.4.2 Structural Health Monitoring

Once the product is in service, continuous condition and health monitoring become essential to guarantee safety and operability. Structural Health Monitoring (SHM) has emerged as a critical technology for ensuring the safety and reliability of structures throughout their operational life [25]. Unlike traditional NDT methods, which often require time-consuming inspections and may involve disassembling components, SHM offers a continuous, real-time assessment of a structure health by integrating sensors, data processing, and smart materials directly within the structure [13]. SHM not only monitors the current condition of a structure but also [163]:

- tracks the operational and environmental loads,
- assesses load-induced damages,
- monitors the progression of damage over time, and
- evaluates the overall performance as the structure ages.

This integration allows for the early detection of damage, enabling prompt corrective actions that can minimize downtime, reduce maintenance costs, and prevent catastrophic failures. Numerous classification schemes for different levels of SHM exist in the literature, with one of the most comprehensive outlining six fundamental levels [164], [165]:

- Level 1: detection of damage
- Level 2: localization of damage
- Level 3: definition of the kind of damage
- Level 4: quantification of the severity of the damage
- Level 5: estimation of the remaining useful life
- Level 6: develop capabilities for autonomous diagnosis and self-repair

To date, according to Kralovec et. al. [165], the most advanced SHM methods have successfully advanced to Level 4, with Level 5 damage assessment remaining in the conceptual stage.

The development of SHM systems has seen significant progress, particularly in applications involving rotating machinery [166]. However, advancements in SHM for health monitoring of transportation vehicles, including aerospace and automotive systems, have been slower. This lag is primarily due to the wide range of environmental and operational conditions these vehicles encounter, which are often variable and unpredictable [165]. Such variability makes it challenging to accurately identify both nominal and off-nominal operating scenarios, complicating the definitive detection of damage and increasing the risk of false positives. The complexity of these conditions, coupled with the uncertainty in diagnostic accuracy, makes it difficult to fully quantify the economic benefits of SHM in these applications [165].

One of the primary advantages of SHM is its ability to facilitate the transition from a scheduled-based maintenance approach to a Condition-Based Maintenance (CBM) approach. **Figure 14** schematically illustrates the inherent limitations of the traditional scheduled-based maintenance model and highlights the potential benefits of adopting a CBM approach.

In the aviation industry, regular maintenance is critical to prevent component and system failures during operation. Traditionally, aircraft maintenance is performed based on predefined intervals, determined by Flight Hours (FH), Flight Cycles (FC), or calendar days (DY) [167]. These usage parameters dictate when inspections occur, with airlines often adopting a top-down approach to plan maintenance. Major tasks are grouped into letter checks—A-, B-, C-, and D-checks—each associated with specific intervals (e.g., C-/D-checks every 3–5 years, A-checks every 6–12 months). Although B-checks are less common, their tasks are usually integrated into subsequent A-checks [168]

Figure 14 (a) depicts the scheduled-based maintenance approach, identifying three possible scenarios [13]. The first scenario is the ideal case, where damage initiates before the scheduled inspection, is detected, and is successfully repaired during the inspection. In the second scenario, damage occurs after the inspection, potentially leading to an in-flight failure if undetected, posing significant safety risks. Alternatively, the damage might be identified during external visual inspections, ground-based NDT, or routine checks, leading to unscheduled maintenance and increased costs and inefficiencies. Additionally, during scheduled inspections, components are often replaced before reaching their full service life, resulting in underutilization of their potential lifespan. This inefficiency is further compounded in large airlines, where maintenance planning becomes increasingly complex [167]. Maintenance planners may need to spend considerable time scheduling activities, further highlighting the limitations of the scheduled-based approach.

Figure 14 (b) illustrates the CBM approach, which represents a significant advancement over traditional scheduled-based maintenance. In the CBM model, on-board sensors continuously monitor the health status of aircraft components and systems, providing real-time data that informs maintenance decisions. This continuous flow of information enables maintenance to be performed only when necessary, based on the actual condition of the aircraft, rather than following predetermined intervals [169].

CBM offers several key advantages, including the prevention of unscheduled maintenance events by identifying potential issues early, before they escalate into serious problems. This proactive approach not only enhances safety but also allows for the extension or rescheduling of maintenance tasks based on the effective health condition of the components. By optimizing the timing of these tasks, CBM minimizes unnecessary replacements, thus maximizing the service life of each component and reducing overall maintenance costs.

Furthermore, CBM facilitates the efficient substitution of maintenance tasks and enables the optimization of maintenance schedules across entire fleets, ensuring that resources are allocated where they are most needed [163]. While ground-based NDT remains a valuable tool, under the CBM approach, it serves as a complementary source of data, contributing to a more robust Aircraft Health Management (AHM) system. This system is composed of two main elements: Usage Monitoring (UM), which collects data on operational conditions and environmental factors; and SHM, which provides insights into the health of the aircraft structure. As maintenance actions are driven by real-time data and a comprehensive understanding of the aircraft condition. This approach ultimately leads to more efficient fleet-level maintenance schedules, reducing downtime and ensuring higher operational readiness.

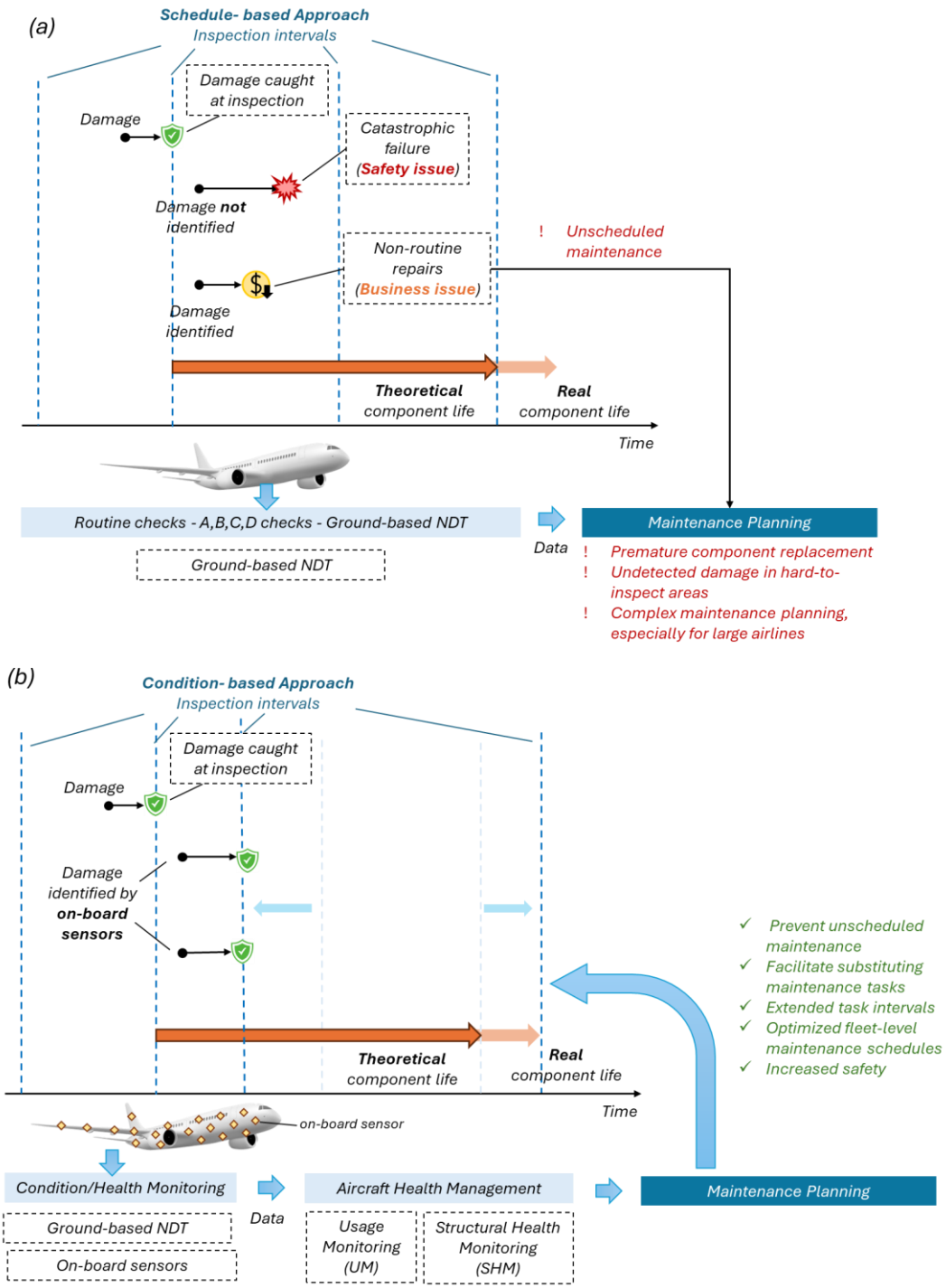

Figure 14 Comparison of Maintenance Approaches: (a) Scheduled-Based Maintenance vs. (b) Condition-Based Maintenance in Aircraft Health Management.

Many SHM techniques present promising capabilities for damage assessment, each leveraging a specific physical principle related to the structure under study as damage initiates and progresses. To address the need for robust detection of various damage types in both metallic and composite structures, a wide array of sensing techniques has been developed, with multiple methods often applicable to detecting a particular form of damage. This variety of techniques has led to growing interest in multi-sensor approaches that integrate multiple physical entities for enhanced detection capabilities. For instance, in 2018, the *International Journal of Distributed Sensor Networks* published a special issue focusing on multi-sensor data fusion for SHM [170]. This data fusion can involve

either homogeneous sensor data (from the same sensor type and physical principle) or heterogeneous sensor data (from different sensor types and physical principles). Kralovec et al. [165] demonstrated the effectiveness of combining various SHM methods, highlighting their high sensitivity to diverse structural properties and their potential for improved damage identification.

SHM methods can be broadly classified into passive and active approaches. Passive techniques rely solely on sensors embedded in the structure to monitor its condition over time. In contrast, active techniques involve both sensors and actuators, where actuators induce perturbations in the structure, and sensors monitor the resulting response [25]. Technologies are sometimes categorized by sensor type, such as Piezoelectric (PZT) transducers, eddy current sensors, fibre optic sensors, or accelerometers. However, since the same sensor type may be employed in multiple techniques, a more effective classification, as proposed by Güemes et al. [163], is based on the underlying physical principles of the technologies.

Table 5 presents the wide variety of sensing methods, categorized according to their physical principles and whether they are passive or active techniques. The table builds on the work of Güemes et al. [163], incorporating updates from recent review articles and key publications, as well as additional techniques. A concise overview of each method is provided as follows, with further details available in the referenced sources.

Vibration-based methods are among the most traditional approaches, relying on changes in the dynamic response of a structure to detect damage, such as shifts in natural frequencies or mode shapes [171]. **Strain-based methods** utilize sensors like strain gauges or fibre Bragg gratings to measure the strain distribution in a structure, providing direct insight into deformation and potential damage areas [172].

Ultrasonic Guided Waves (UGW) are an advanced technique involving the propagation of elastic waves through the structure, capable of detecting flaws such as cracks or corrosion over large areas with high sensitivity [173]. In contrast, **Acoustic Emission (AE)** is a passive method that monitors transient elastic waves generated by the rapid release of energy from localized sources within the material, offering real-time detection of crack initiation and growth without the need for external excitation [18]. **Phased Array Ultrasonics** is a sophisticated extension of ultrasonic testing, using multiple elements to steer the ultrasonic beam electronically, enabling detailed imaging of internal structures and precise flaw characterization [174]. **Comparative Vacuum Monitoring (CVM)** is a surface-based technique that detects the presence of cracks by monitoring changes in pressure in a vacuum-sealed area over the structure [175].

In **Resistance-Based Sensing**, variations in electrical resistance within materials doped with Carbon Nanotubes (CNT) or PZT particles, as well as through the application of CNT sensing skins, are monitored and directly correlated with mechanical strain or the presence of damage [176]. In contrast, **Electrical Impedance Tomography (EIT)** involves integrating a network of electrode arrays into the structure. By injecting alternating current and measuring the resulting potential differences across the electrodes, EIT generates detailed internal impedance maps, providing a comprehensive characterization of the material internal state [32].

Electromagnetic techniques encompass methods such as eddy current testing, which detects surface and near-surface defects through the interaction of induced currents and magnetic fields [177]. **Electromagnetic Acoustic Transducers (EMAT**) utilize electromagnetic fields to generate elastic waves, enabling the contactless generation of

guided waves. This method eliminates the need for physical contact or the strong coupling required by traditional PZT transducers, offering a distinct advantage in scenarios where direct contact with the material is challenging or impractical [178].

Table 5 Classification of SHM Technologies.

Physical principle	**Sensing method**	**Main sensor Type**	**Passive or active**	**Key publications and recent review articles**
Continuous mechanic	Vibration method	Accelerometers	Passive	[171], [179], [180]
	Strain-based methods	Strain gauges, PZT, fiber optic sensors	Passive or active	[172], [181], [182]
Elastic waves	Ultrasonic guided waves (UGW)	PZT	Active	[173], [183]–[185]
	Acoustic emission (AE)	PZT, AE probes	Passive	[18], [186]–[188]
	Phased arrays	PZT	Active	[174], [189], [190]
Fluid dynamics	Comparative vacuum monitoring (CVM)	Patch with microchannels	Passive	[175], [191]
Electromagnetism (Ohm's Law)	Electrical impedance tomography (EIT)*	Electrodes	Active	[32], [34]
	Resistance-based sensing	CNT-doped or PZT-doped resin, CNT sensing skin	Active	[176], [192]
Electromagnetism	Electromagnetic techniques	Eddy current sensors, magnectostrictive sensors, capacitive sensors	Active	[20], [177], [193]
Electricity + Elastic waves	Electromechanical impedance (EMI)	PZT	Active	[194], [195]
	Electromechanical impedance spectroscopy (EMIS)	Piezoelectric wafer active sensor (PWAS)	Active	[196], [197]
Electromagnetism + Elastic waves	Electromagnetic Acoustic Transducers (EMAT)	Coils, magnets	Active	[178]

*__Note__: Several variations of Electrical Impedance Tomography (EIT) are documented in the literature. EIT utilizes AC current to generate detailed internal impedance images, whereas Electrical Resistance Tomography (ERT) uses DC current for internal resistance mapping [32]. In contrast, Electrical Potential Mapping (EPM) also employs DC current but is specifically designed to map surface potential distribution [34].

Electromechanical Impedance (EMI) and **Electromechanical Impedance Spectroscopy (EMIS)** are closely related methods that utilize piezoelectric materials to monitor changes in mechanical impedance as a function of frequency, providing insights into structural integrity and the presence of damage [195]. These techniques are

distinguished by their use of high-frequency elastic waves and their ability to detect subtle changes in the material properties [196].

Despite the increasing interest in SHM, its application to FSW and thermoplastic welding remains relatively underexplored. A comprehensive literature review revealed only 17 publications that have addressed SHM in the context of these welding techniques. The search criteria were focused exclusively on studies that incorporated sensors directly attached to the material, facilitating on-board monitoring during service.

Figure 15 (a) presents the distribution of publications by welding type, with stacked columns illustrating the SHM techniques employed in each study. The majority of studies focus on FSW, particularly for aluminium alloys, with a smaller number of publications dedicated to ultrasonic welding of thermoplastics. Notably, only one study was found on microwave welding, while no research has been identified on SHM for induction welding.

Figure 15 (b) visualizes the types of sensors employed for each welding technique, underscoring the variability and potential of SHM in these contexts. The dominance of CNT films (7 papers) for monitoring changes in electrical resistance, particularly in detecting damage, is evident. Additionally, guided wave methods utilizing PZT transducers were reported in 5 papers. Other approaches include the use of fibre optics and the integration of PZT particles into the FSW process to create self-sensing capabilities for detecting induced damage.

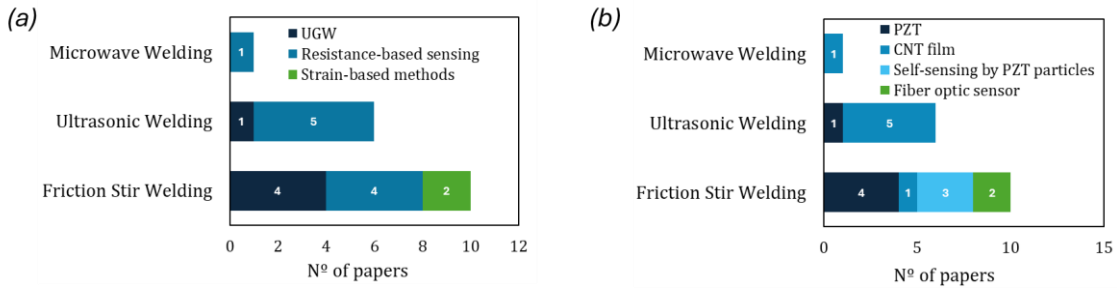

Figure 15 Literature distribution of SHM (a) techniques and (b) sensors type employed for the health monitoring of welded joints.

Specifically concerning the research conducted on FSW, Fakih et al. [198], [199] demonstrated the utility of UGW for detecting flaws in AZ31B magnesium FSW joints, using piezoelectric wafers to excite Lamb waves and applying advanced signal analysis methods. Their work confirmed the sensitivity of Lamb waves in detecting weld defects and quantifying internal flaws through CT scans and finite element modelling. Sorrentino et al. [200] utilize guided waves to accurately locate and quantify damage in aluminium FSW joints through the use of a damage index based probability method, thereby supporting on-board SHM systems in aerospace applications. Gautam et al. [201] explored Lamb waves for assessing weld quality in thin-section FSW joints, correlating wave transmission losses with weld parameters to predict structural integrity.

In the realm of strain-based methods, Richter-Trummer et al. [144] employed Fiber Bragg Grating (FBG) sensors to monitor transient and residual strains during Metal Inert Gas and FSW processes, offering insights into weld behaviour and process optimization. Bento et al. [145] extended this approach by integrating Bragg sensors in hybrid FSW welds, demonstrating their effectiveness in continuous deformation monitoring and weld quality evaluation throughout manufacturing and service phases.

For resistance-based sensing, Liu et al. [202] introduced a thin-film sensor with MXene and Single-Walled Carbon Nanotubes (SWCNTs) for real-time strain monitoring of Al 7075 FSW joints. This sensor effectively captured elastic and plastic deformations, correlating resistance changes with strain levels. Ferreira et al. [203]–[205] advanced Self-Sensing Materials (SSMs) by incorporating piezoelectric particles like PZT and Barium Titanate (BT) into aluminium through FSW. Their studies highlighted the superior sensitivity of PZT-based SSMs, despite some trade-offs in mechanical properties, and demonstrated the potential of SSMs for enhanced structural monitoring while addressing challenges related to brittleness and processing complexities.

Efforts in SHM of thermoplastic welded joints have concentrated on a different approach. Specifically, significant work has been dedicated to developing a multifunctional film that not only facilitates the welding process but also integrates resistance-based sensing for real-time monitoring.

Kravchenko et al. [206] introduced a novel microwave welding technique using Carbon Nanostructure (CNS) suspensions. This method created a conductive network at the welded interface, which enabled the detection of structural integrity during mechanical testing, proving effective across various thermoplastic substrates. Frederick et al. [207] further developed this concept by creating multifunctional energy directors using MWNT/PP films for ultrasonic welding. These films not only facilitated the welding process but also enabled SHM through resistance measurements during cyclic bending tests. The research underscored the films' multifunctionality, including their potential for disassembly and repair of welded joints, although they slightly reduced lap shear strength. Li et al. [208]–[210] explored the use of multifunctional nanocomposite polymer films containing Multi-Walled Carbon Nanotubes (MWCNTs) embedded in Glass Fiber/Polypropylene (GF/PP) joints, welded via ultrasonic methods. These films, capable of monitoring strain and damage through electrical resistance changes, demonstrated an increase in flexural strength by 20.6% and successfully detected crack propagation, highlighting their potential for integrated SHM in thermoplastic composite joints.

In the domain of UGW, Ochôa et al. [211] focused on understanding how weld manufacturing defects in ultrasonically welded thermoplastic composite joints affect wave transmission. By producing controlled defects such as unwelded areas and adherend fiber bundle distortion, the study demonstrated that UGW could effectively detect and distinguish these defects through changes in signal characteristics like Time-of-Flight and frequency shifts. This research is significant for advancing SHM capabilities in modern thermoplastic composite structures, particularly in aerospace applications where early detection of defects is critical to preventing unexpected failures.

2.5 Selection of Monitoring Case Studies and Research Contribution

After conducting an exhaustive review of the state of the art in real-time process monitoring and SHM techniques for FSW and thermoplastic induction welding, a critical knowledge gap has been identified in the application of electromagnetic techniques across four specific cases, as illustrated in **Figure 16**. These gaps include: **(1)** the use of electromagnetic techniques for real-time process monitoring of the FSW process, **(2)** their application in real-time monitoring of induction welding for thermoplastic composites,

(3) their deployment in SHM for friction stir welded joints, and **(4)** their use in SHM for thermoplastic induction welded joints.

<table>
<tr><th></th><th>Monitoring Approaches</th><th>Friction Stir Welding</th><th>Thermoplastic Induction Welding</th></tr>
<tr><td rowspan="7">Real Time Process Monitoring</td><td>Machine Vision System</td><td>[138]–[141]</td><td rowspan="4">Unexplored potential of alternative methods</td></tr>
<tr><td>AE</td><td>[150]–[154]</td></tr>
<tr><td>PAUT</td><td>[143]</td></tr>
<tr><td>Strain based methods by FOS</td><td>[144], [145]</td></tr>
<tr><td>Thermography</td><td rowspan="2">Unexplored potential of alternative methods</td><td>[147], [148]</td></tr>
<tr><td>Temperature measurement by FOS</td><td>[149], [162]</td></tr>
<tr><td>Electromagnetic Techniques</td><td>1 Knowledge gap & Research contribution</td><td>2 Knowledge gap</td></tr>
<tr><td colspan="4"></td></tr>
<tr><td rowspan="4">SHM</td><td>UGW</td><td>[198]–[201]</td><td rowspan="3">Unexplored potential of alternative methods</td></tr>
<tr><td>Resistance based sensing</td><td>[202]–[205]</td></tr>
<tr><td>Strain based methods</td><td>[144], [145]</td></tr>
<tr><td>Electromagnetic Techniques</td><td>3 Knowledge gap</td><td>4 Knowledge gap & Research contribution</td></tr>
</table>

Figure 16 Comprehensive mapping of NDT for real time process monitoring and SHM Techniques applied in FSW and Thermoplastic Induction Welding: identification of electromagnetic-based monitoring gaps and contributions of the present research.

Among these, the focus of the present investigation is **on the first** and **fourth cases** for the following reasons:

- Although numerous methods have been employed for real-time monitoring of FSW, there is a notable absence of research on the potential ECT for real-time control. ECT holds significant promise due to its **non-contact nature, rapid measurement capability, and sensitivity to microstructural changes**, offering distinct advantages over other techniques such as ultrasonic-based methods, which require good contact through couplants, or machine vision systems, which are limited to detecting only superficial defects.

- Regarding thermoplastic welding, the current state of real-time process monitoring is **still nascent**. Establishing a robust correlation between eddy

current sensor signals and the anisotropy of conductivity in composite materials like CFRP is essential before ECT can be effectively utilized. Furthermore, temperature monitoring, despite its challenges, offers considerable potential for process quality control in this context, with thermography techniques showing promise for real-time detection [148].

- The literature includes some investigations into SHM for friction stir welded joints using alternative techniques; however, the application of electromagnetic techniques for SHM in thermoplastic induction welded joints remains entirely unexplored. Developing a sensor capable of monitoring the health of thermoplastic joints during service life could be particularly beneficial, given the **limited understanding of damage propagation** in composite materials.

The following two paragraphs provide a detailed examination of the context surrounding the two selected cases and highlight key aspects that guided the investigation.

2.5.1 CASE I: Real time monitoring of FSW process

For the successful integration of ECT in the real-time monitoring of FSW, a critical first step is to establish a **robust correlation** between the ECT probe signal and the weld microstructural and mechanical properties, as well as the presence of defects. As illustrated in **Figure 17**, developing this correlation enables the precise interpretation of the ECT probe signal, facilitating the identification of process deviations and the underlying causes. This understanding allows for timely corrective actions through appropriate adjustments to process parameters. ECT high sensitivity to variations in electrical conductivity, caused by microstructural changes such as grain refinement and precipitate dissolution, not only enhances defect detection but also offers a non-invasive method for assessing the mechanical properties of the weld. This capability has the potential to reduce the workload in final inspection and significantly improve the reliability and efficiency of the welding process.

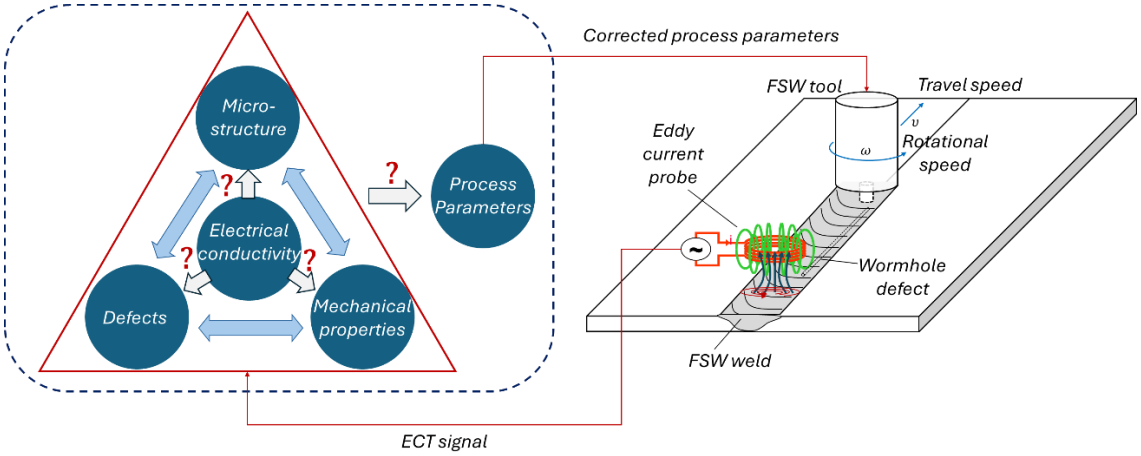

Figure 17 Correlation framework for ECT signal interpretation and process adjustment in real-time monitoring of FSW.

The FSW process induces significant changes in the electrical conductivity of the material due to the high temperatures involved. This dependency between conductivity and temperature requires the ECT probe to be positioned at an optimum distance from the FSW tool to ensure that the weld bead is measured under conditions of lower and more

uniform temperature (**Figure 17**). This approach minimizes the temperature effect on the ECT signal, ensuring more accurate detection of microstructural changes. While various compensation techniques can mitigate the influence of temperature on the ECT signal [212]–[215], the **essential prerequisite** is to first achieve a reliable correlation between the ECT signal and the microstructural and mechanical properties at room temperature. This correlation is fundamental for accurately interpreting the ECT signal and for the successful application of ECT in real-time monitoring.

In investigating this correlation framework, it is crucial to consider the variety of defects that may occur during the FSW process. Defects can be grouped into 3 main categories [11] as shown in **Figure 18**, which also illustrates their typical locations within the weld: defects caused by insufficient heat, excessive heat, and design flaws. An exhaustive description of defects encountered in the FSW process can be found in the following references [5], [11], [216], [217]

Among these, wormhole defects (**Figure 18 (c)**) are particularly significant due to their substantial impact on the mechanical properties of the weld and their sub-surface location, which makes them undetectable through visual inspection. The morphology of wormhole defects, characterized by a rounded cross-section, also poses a greater challenge for detection using ECT, compared to sharper defects like lack of penetration or kissing bonds.

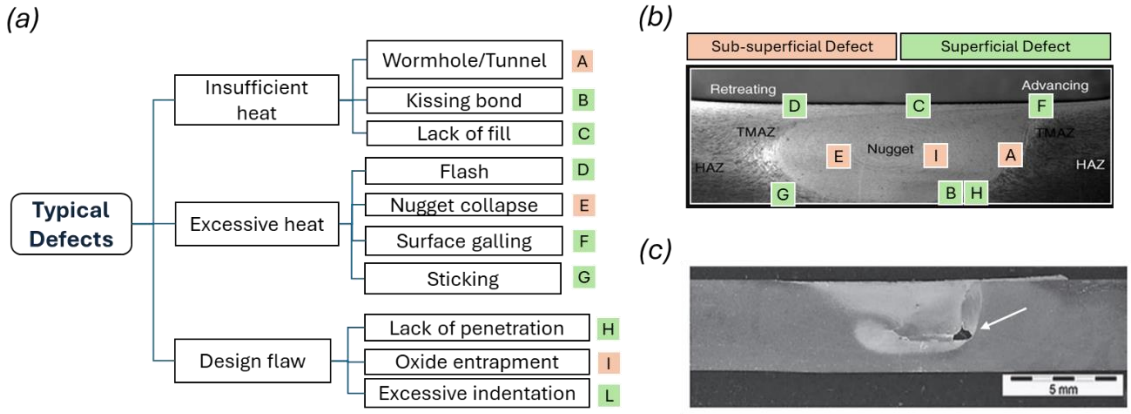

Figure 18 (a) Typical defect types encountered in FSW and (b) locations within the weld according to the classification of Mishra et. al [11]. (c) Cross-sectional view of a FSW weld illustrating a wormhole defect [218].

Given the significant impact of wormhole defects on weld integrity and the challenges they present for detection, **wormholes were chosen** as the **primary defect** for evaluating the **detection capabilities** of the developed **ECT probe**.

2.5.2 CASE II: SHM of thermoplastic welded joints

In the aeronautical sector, ensuring in-flight safety is paramount, and structures are designed with a fail-safe philosophy, where damage tolerance is built into the design to ensure that any damage detected does not compromise structural integrity below acceptable levels [219]. Understanding damage propagation in thermoplastic welded joints is essential for setting inspection intervals and maintenance schedules [13]. However, there is a notable scarcity of historical data on the fatigue behaviour of thermoplastic induction welded joints. Real-time access to the health status of these

joints—encompassing damage detection, localization, quantification, and residual life prediction—can shift maintenance practices from a scheduled-based approach to a condition-based approach, enhancing both safety and efficiency. As illustrated **Figure 19**, the health assessment of thermoplastic welded joints SHM enables the establishment of a quantitative damage indicator that reflects both the extent of damage and the residual strength of the joint. This damage indicator serves as a crucial metric for determining a safe operational threshold, based on the design life of the structure [13]. The projection of the remaining service life based on this indicator is inherently subject to the measurement uncertainties associated with the employed SHM technique. Nevertheless, as long as the damage indicator remains below the established safety threshold, the joint is considered to operate within safe operational limits. Conversely, when the damage indicator exceeds this threshold, it signals the onset of unsafe conditions and the potential for structural failure, necessitating immediate intervention.

In particular, electromagnetic-based SHM techniques leverage the fact that damage alters the local electromagnetic properties of materials, particularly electrical conductivity (σ) and dielectric permittivity (ε_r) in fibre-reinforced polymers. For carbon-epoxy structures, this capability is significant, as it facilitates the detection of various types of damage [193]:

1. **Mechanical Damage**: This includes impacts that cause delaminations and fibre breakage. Such damage induces distinct variations in local electrical conductivity, as it affects the carbon fibres directly.

2. **Thermal Damage**: Caused by proximity to high temperatures or electrical impacts such as sparks. In cases of high heat, the damage primarily alters conductivity. Smaller burns, however, may not change conductivity but affect dielectric permittivity due to resin pyrolysis.

3. **Damage from Liquid Ingress**: Exposure to liquids such as water, oil, or fuel can initiate chemical reactions that weaken the structure. This type of damage mainly affects dielectric permittivity, as the liquid introduces a medium with different dielectric properties.

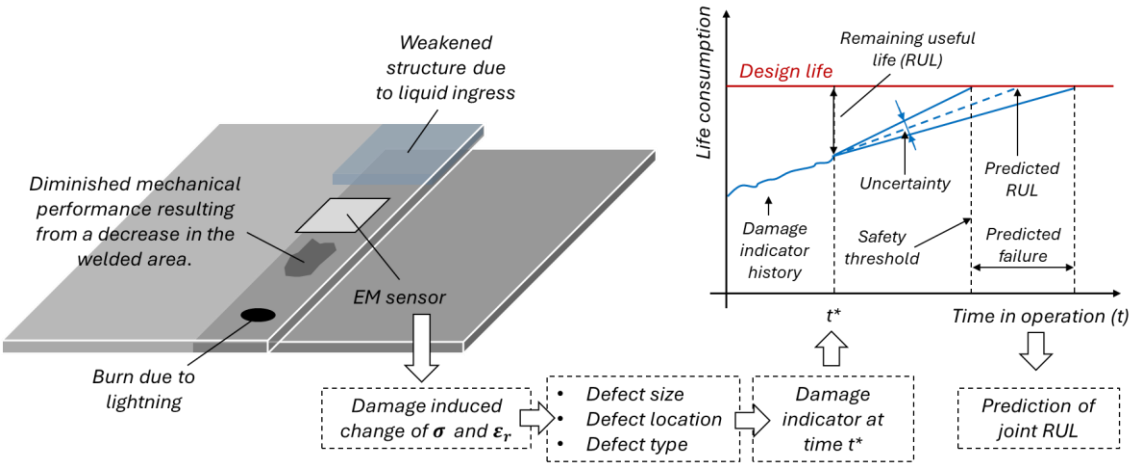

Figure 19 Damage indicator and SHM-based assessment of thermoplastic welded joints: establishing safety thresholds and detecting defects using electromagnetic properties (Life consumption vs. Time in operation graph adapted from [13]).

The development of sensitive systems to assess these properties and correlate them with specific types of damage can provide valuable insight into the condition of induction welded joints, while improving the understanding of damage propagation in such structures. Whitin this framework, establishing a robust correlation between changes in electrical properties and the sensor signal is crucial for accurate damage assessment.

To select the appropriate defect case for developing the EM sensor for SHM, careful consideration was given to the types of flaws that significantly impact the performance of thermoplastic induction welded joints. Most defects reported in the literature are manufacturing-related, with voids being a common issue due to suboptimal pressure application during the consolidation phase [129]. These voids can lead to delamination, particularly as they coalesce over time, causing separation between layers within the laminate.

Additionally, while limited data exists on the in-service behaviour of induction welded joints, insights from studies on similar thermoplastic welding methods, such as infrared welding [98], [220], [221], reveal that cracks typically initiate at the weld interface and propagate inward, eventually compromising the structural integrity of the joint.

Given this understanding, it becomes evident that the weld interface area represents the weakest point in the joint. A reduction in this area, whether caused by crack propagation or impact-induced delamination, poses a critical risk to the joint performance.

Therefore, the defect case study selected was **a delamination at the welding interface** to simulate a **reduced contact area**. This scenario was chosen to rigorously test the effectiveness of the proposed SHM method in detecting such critical conditions, ensuring the sensor capability to monitor and predict joint integrity in real-world applications.

2.6 Summary of Chapter 2

This chapter has explored the capabilities of ECT as a promising method for real-time process monitoring and SHM of welded joints in aerospace applications. ECT, characterized by its non-invasive nature and real-time capability, stands out as a promising electromagnetic technique, particularly suited for aluminium alloys FSW joints and CFRP laminates. Among various welding processes evaluated, FSW and thermoplastic induction welding have emerged as the most relevant and promising for the aerospace sector. These methods not only provide robust solutions but also align well with the industry stringent standards and requirements for quality and durability.

However, despite several investigations in real-time process monitoring and SHM of these welded joints, a significant knowledge gap has been identified in the application of electromagnetic-based techniques, pointing towards a need for further research and development. Focusing on the vast potential of this field, this investigation is specifically focused in investigating the correlation between electrical conductivity and microstructural characteristics, including the presence of damage and mechanical properties. Two key applications were selected: real-time process monitoring of FSW and SHM of induction welded joints.

Chapter 3

3 Background Theory

Chapter 3 lays the theoretical groundwork for understanding the electromagnetic phenomena used in material analysis and monitoring. It begins with Maxwell's Equations and constitutive relations, which describe the behaviour of electric and magnetic fields in various media. The chapter then introduces eddy currents and their role in electromagnetic testing, followed by an overview of numerical methods, including both analytical approaches and the Finite Element Method (FEM). Finally, it examines the electrical properties of CFRP and the variations in electrical conductivity due to microstructural changes in FSW processes.

3.1 Maxwell's Equations and Constitutive Relations

The problem of electromagnetic analysis on a macroscopic level is expressed by solving ***Maxwell's equation*** subject to certain boundary conditions and defined constitutive relations that describe the macroscopic properties of the medium.

Maxwell's equations are a set of equations, written in differential or integral form, stating the relationships between the fundamental electromagnetic quantities. These quantities are:

- Electric field intensity $\boldsymbol{E}$ (physical field that surround an electric charge and exerts force on all other charges in the field. Electric fields originate form electric charges or from time-varying magnetic fields).
- Electric displacement or electric flux density $\boldsymbol{D}$ (or electric induction, a vector field accounting for the effects of free and bound charges within material)
- Magnetic field intensity **H** (the part of the magnetic field in a material that arises from an external current and is **not intrinsic** to the material itself)
- Magnetic flux density $\boldsymbol{B}$ (a measure of **the actual magnetic field within a material** considered as a concentration of magnetic field lines, or flux, per unit cross-sectional area)
- Current density $\boldsymbol{J}$ (In the following $\boldsymbol{J_f}$ is the current associated to only **free charges**)
- Electric charge density ρ

The equations can be formulated in differential form or integral form. The differential form leads to differential equations that specific numerical method, such as the finite element method, can handle. The differential form is:

$$\nabla \times \boldsymbol{H} = \boldsymbol{J_f} + \frac{\partial \boldsymbol{D}}{\partial t} \qquad (Maxwell - Ampère's\ law) \tag{1}$$

$$\nabla \times \boldsymbol{E} = -\frac{\partial \boldsymbol{B}}{\partial t} \qquad (\text{Faraday's law}) \tag{2}$$

$$\nabla \cdot \boldsymbol{D} = \rho_f \qquad (\text{Gauss' law} - \text{electric form}) \tag{3}$$

$$\nabla \cdot \boldsymbol{B} = 0 \qquad (\text{Gauss' law} - \text{magnetic form}) \tag{4}$$

Implicit in the Maxwell equation is the equation of continuity for charge density and current density, obtained combining the derivative of *(iii)* with the divergence of *(i)*:

$$\nabla \cdot \boldsymbol{J} = -\frac{\partial \rho}{\partial t} \tag{5}$$

The relationship between the fundamental electromagnetic quantities is expressed by the **constitutive equations**. The general form of the constitutive relation is

$$\boldsymbol{D} = \boldsymbol{D}[\boldsymbol{E}, \boldsymbol{B}] \tag{6}$$

$$\boldsymbol{H} = \boldsymbol{H}[\boldsymbol{E}, \boldsymbol{B}] \tag{7}$$

The square brackets signify that the connection are not necessarily simple and may depend on past history (hysteresis), may be nonlinear,etc. A general way to express this relations could be [222]:

$$\boldsymbol{D} = \varepsilon_0 \boldsymbol{E} + \left(\boldsymbol{P} - \sum_{\beta} \frac{\partial Q'_{\alpha\beta}}{\partial x_\beta} + \cdots \right) \tag{8}$$

$$\boldsymbol{H} = \frac{\mathbf{1}}{\boldsymbol{\mu_0}} \boldsymbol{B} + (\boldsymbol{M} + \cdots) \tag{9}$$

Where ε_0 and μ_0 are respectively the electrical permittivity and magnetic permeability of vacuum. The electric polarization vector **P** describes how the material is polarized when an electric field E is present. It can be interpreted as the volume density of electric dipole moments. P is generally a function of E. Some materials can have a nonzero P also when there is no electric field present. The magnetization vector **M** similarly describes how the material is magnetized when a magnetic field H is present. It can be interpreted as the volume density of magnetic dipole moments. M is generally a function of H. Permanent magnets, for instance, have a nonzero M also when there is no magnetic field present.

The quantity $\mathbf{P}, \mathbf{M}, \mathrm{Q}'_{\alpha\beta}$ and similar higher order objects represent the macroscopically averaged electric dipole, magnetic dipole, electric quadrupole and higher moment densities of the material medium in presence of applied fields. In most material **electric quadrupoles and higher terms** are completely **negligible** and only the electric and

magnetic polarizations **P** and **M** are **significant**. In this case, the equations (8) and (9) becomes:

$$\boldsymbol{D} = \varepsilon_0 \boldsymbol{E} + \boldsymbol{P} \tag{10}$$

$$\boldsymbol{B} = \mu_0 (\boldsymbol{H} + \boldsymbol{M}) \tag{11}$$

In addition to the previous ones, for conducting media another important equation is the Ohm's Law. The general form of the Ohm's Law is:

$$\boldsymbol{J_f} = \boldsymbol{J_f}[\boldsymbol{E}, \boldsymbol{B}] \tag{12}$$

When the presence of an applied electric or magnetic field induces an electric or magnetic polarization proportional to the magnitude of the applied field, we then say that the response of the **medium is linear.** For **linear materials**, the polarization is directly proportional to the electric field ($\boldsymbol{P} = \varepsilon_0 \chi_e \boldsymbol{E}$, where $\boldsymbol{\chi_e}$ is the **electric susceptibility**) and the magnetisation is directly proportional to the magnetic field ($\boldsymbol{M} = \chi_m \boldsymbol{H}$, where $\boldsymbol{\chi_m}$ is the **magnetic susceptibility**). For such materials, the constitutive relations and the Ohm's law are:

$$\boldsymbol{D} = \varepsilon_0 (1 + \chi_e) \boldsymbol{E} = \varepsilon_0 \varepsilon_r \boldsymbol{E} = \varepsilon \boldsymbol{E} \tag{13}$$

$$\boldsymbol{B} = \mu_0 (1 + \chi_m) \boldsymbol{H} = \mu_0 \mu_r \boldsymbol{H} = \mu \boldsymbol{H} \tag{14}$$

$$\boldsymbol{J_f} = \bar{\sigma} \boldsymbol{E} \tag{15}$$

where ε_r , μ_r and $\bar{\sigma}$ are respectively relative permittivity, relative permeability and electrical conductivity.

$\bar{\sigma}$, χ_e and χ_m are tensors. For anisotropic materials, they could expressed:

$$\chi_e = \begin{vmatrix} \chi_{e11} & \chi_{e12} & \chi_{e13} \\ \chi_{e21} & \chi_{e22} & \chi_{e23} \\ \chi_{e31} & \chi_{e32} & \chi_{e33} \end{vmatrix} ; \chi_m = \begin{vmatrix} \chi_{m11} & \chi_{m12} & \chi_{m13} \\ \chi_{m21} & \chi_{m22} & \chi_{m23} \\ \chi_{m31} & \chi_{m32} & \chi_{m33} \end{vmatrix} ; \bar{\sigma} = \begin{vmatrix} \sigma_{11} & \sigma_{12} & \sigma_{13} \\ \sigma_{21} & \sigma_{22} & \sigma_{23} \\ \sigma_{31} & \sigma_{m32} & \sigma_{33} \end{vmatrix} \tag{16-18}$$

For orthotropic material:

$$\chi_e = \begin{vmatrix} \chi_{e11} & 0 & 0 \\ 0 & \chi_{e22} & 0 \\ 0 & 0 & \chi_{e33} \end{vmatrix} ; \chi_m = \begin{vmatrix} \chi_{m11} & 0 & 0 \\ 0 & \chi_{m22} & 0 \\ 0 & 0 & \chi_{m33} \end{vmatrix} ; \bar{\sigma} = \begin{vmatrix} \sigma_{11} & 0 & 0 \\ 0 & \sigma_{22} & 0 \\ 0 & 0 & \sigma_{33} \end{vmatrix} \tag{19-21}$$

For isotropic material:

$$\chi_e = \begin{vmatrix} \chi_e & 0 & 0 \\ 0 & \chi_e & 0 \\ 0 & 0 & \chi_e \end{vmatrix} ; \chi_m = \begin{vmatrix} \chi_m & 0 & 0 \\ 0 & \chi_m & 0 \\ 0 & 0 & \chi_m \end{vmatrix} ; \bar{\sigma} = \begin{vmatrix} \sigma & 0 & 0 \\ 0 & \sigma & 0 \\ 0 & 0 & \sigma \end{vmatrix} \tag{22-24}$$

where $\chi_e = \chi_{e_{11}} = \chi_{e_{22}} = \chi_{e_{33}}$, $\chi_m = \chi_{m_{11}} = \chi_{m_{22}} = \chi_{m_{33}}$, $\sigma = \sigma_{11} = \sigma_{22} = \sigma_{33}$.

Quasi-static field

To introduce simplifications to Maxwell's equations, it is essential to account for the electromagnetic wavelength. The wavelength (λ) is derived from the wave frequency (f) and the speed of light (c), a universal constant of 299,792,458 meters per second. This relationship forms the basis for analysing wave behaviour and allows for *appropriate approximations* in different electromagnetic regimes.

$$\lambda = \frac{c}{f} \tag{25}$$

When the wavelength λ is large enough compared with the characteristic size (L_c) of the device or object under study, the **displacement current** $\partial D/\partial t$ can **be neglected**. Under this condition, the electric field can be considered **quasi-static**, meaning changes in the field propagate instantaneously across the object, and wave-like phenomena are insignificant. This criterion is typically expressed as:

$$L_c > \lambda/10 \tag{26}$$

Therefore, the Maxwell – Ampere's law becomes:

$$\nabla \times \boldsymbol{H} = \boldsymbol{J_f} \tag{27}$$

Potential formulation of the Maxwell's equations

Under particular circumstances, it can be convenient to formulate the problems in terms of the electric scalar potential V and the magnetic vector potential $\boldsymbol{A}$. As a direct consequence of the electric and magnetic Gauss' law (eq. (3) and (4)) the electric and magnetic vector potential are given by the following equations:

$$\boldsymbol{B} = \nabla \times \boldsymbol{A} \tag{28}$$

$$\boldsymbol{E} = -\nabla \mathrm{V} - \frac{\partial \boldsymbol{A}}{\partial t} \tag{29}$$

In order to uniquely define the vector fields, an additional relation is established between V and $\boldsymbol{A}$. This mathematical procedure called **gauge fixing** allows to obtain a reformulation of the Maxwell's equations in which only the potential of the magnetic field appears. Following the equations (1) and (2), the equation to be solved becomes:

$$\nabla \times (\mu_r{}^{-1} \nabla \times \boldsymbol{A}) + \mu_0 \bar{\sigma} \frac{\partial \boldsymbol{A}}{\partial t} + \mu_0 \frac{\partial}{\partial t}\left(\varepsilon_0 \varepsilon_r \frac{\partial \boldsymbol{A}}{\partial t}\right) = 0 \tag{30}$$

Also in this case, for low frequencies the second order in time term corresponding to the displacement current can be neglected. This is valid when the power transfer is primarily **via conduction and not radiation**:

$$\nabla \times (\mu_r{}^{-1} \nabla \times \boldsymbol{A}) + \mu_0 \bar{\sigma} \frac{\partial \boldsymbol{A}}{\partial t} = 0 \tag{31}$$

For time-harmonic systems, the same governing equation can be expressed into the frequency domain:

$$\nabla \times (\mu_r{}^{-1} \nabla \times \boldsymbol{A}) + (j\omega\bar{\sigma} - \omega^2 \varepsilon)\boldsymbol{A} = 0 \tag{32}$$

3.2 Eddy currents

When an excitation coil carrying an alternating current is brought near a conductive material, it generates a time-varying magnetic field along the coil axial direction. According to Faraday's law of electromagnetic induction, this changing magnetic field induces eddy currents within the material, which flow perpendicular to the applied magnetic field. These induced currents, in turn, generate their own magnetic fields, which oppose the original field, in accordance with Lenz's law. This opposition results in changes to the coil impedance, allowing for the detection and analysis of variations in material properties such as defects or differences in conductivity.

These induced eddy currents, along with their interaction with the primary magnetic field, are fundamental to the operation of ECT, enabling the detection of subsurface defects and material inconsistencies. According to Maxwell's equations, it can be demonstrated that when an electromagnetic field interacts with a material, the amplitude of the induced eddy currents **decreases exponentially** as they penetrate deeper into the material.

Specifically, under the following assumptions:

- Quasi-static field conditions,
- Homogeneous and isotropic material properties,
- The absence of free electric charge in conductive materials (i.e., $\rho_f = 0$ in equation (3)),

the following governing equation can be derived:

$$\frac{\partial^2 E_x}{\partial x^2} + \frac{\partial^2 E_x}{\partial y^2} + \frac{\partial^2 E_x}{\partial z^2} = \mu_0 \sigma \frac{\partial E_x}{\partial t} \tag{33}$$

$$\frac{\partial^2 E_y}{\partial x^2} + \frac{\partial^2 E_y}{\partial y^2} + \frac{\partial^2 E_y}{\partial z^2} = \mu_0 \sigma \frac{\partial E_y}{\partial t} \tag{34}$$

$$\frac{\partial^2 E_z}{\partial x^2} + \frac{\partial^2 E_z}{\partial y^2} + \frac{\partial^2 E_z}{\partial z^2} = \mu_0 \sigma \frac{\partial E_z}{\partial t} \tag{35}$$

The detailed derivation of these equations can be found in [223]. These equations are valid regardless of the chosen coordinate system, as long as the material is assumed to be isotropic.

To simplify the problem, let's consider a planar case where the electric field is polarized in the x-direction (i.e., only the E_x component exists) and propagates in the z-direction, as illustrated in **Figure 20**.

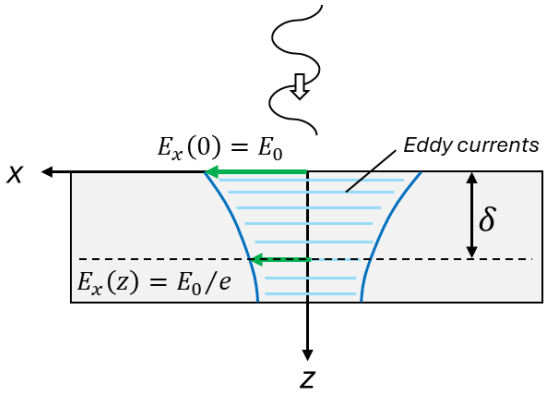

Figure 20 Exponential decay of electric field and eddy current density through material thickness.

Since E_x has a uniform distribution in the x-direction, equation (33) can be simplified as follows:

$$\frac{\partial^2 E_x}{\partial z^2} = \mu_0 \sigma \frac{\partial E_x}{\partial t} \tag{36}$$

Now, consider the case where $E_x = E_0 e^{-j\omega t}$ is applied at the surface (z = 0). As reported in [223], the solution to equation (32) is given by:

$$E_x = E_0 e^{-j\omega(t-\alpha z)} e^{-\beta z} \tag{37}$$

where:

$$\alpha = \sqrt{\frac{\mu_0 \sigma}{2\omega}}, \quad \beta = \sqrt{\frac{\mu_0 \sigma \omega}{2}} \tag{38}$$

The term αz in equation (37) represents the phase shift of the electric field caused by the distance (z) from the surface ($z = 0$), while the term βz indicates the attenuation of the amplitude of E_x due to the increasing distance from the surface.

By applying Ohm's law (Equation (15)), an expression for the distribution of the eddy currents can be derived, demonstrating the exponential decrease in amplitude (see **Figure 20**).

$$J_x = \sigma E_x = \sigma E_0 e^{-j\omega(t-\alpha z)} e^{-\beta z} \tag{39}$$

The **skin effect depth (δ)** is defined as the distance at which the amplitude of E_x decreases to 1/e of its value at the surface. This depth can be determined by solving the equation βz = 1 with respect to z:

$$\delta = \frac{1}{\sqrt{\pi f \mu \sigma}} \tag{40}$$

The skin effect depth, also referred to as the **depth of penetration**, determines how deeply the electromagnetic field penetrates the material. The depth of penetration is defined as the distance below the surface of the conductor at which the current density has fallen to 36.79% of its surface value [66]. It is influenced by several factors, including the frequency of the alternating current (*f*), the magnetic permeability (μ), and the electrical conductivity (σ) of the material [66]. In the presence of discontinuities, defects, or microstructural changes, localized variations in the electrical conductivity and magnetic permeability occur, facilitating the detection of these features through changes in the electromagnetic field.

Detection capability in ECT is strongly influenced by the depth of penetration. It is important to ensure that defects are not located deeper than the calculated penetration depth, as the sensitivity of detection decreases significantly beyond this limit.

The effectiveness of detection in ECT is primarily influenced by the material electrical conductivity (σ). Materials with **high conductivity**, such as metals, allow eddy currents to flow more easily, but at the same time limits the depth of penetration (δ) of the electromagnetic field. In these materials, the induced eddy currents are concentrated near the surface, restricting the inspection to shallow regions.

Conversely, in **low-conductivity materials** like **CFRP**, the reduced ability to conduct electric current allows the electromagnetic field to penetrate deeper into the material. However, to achieve the same depth of penetration as in more conductive materials, the frequency of the applied current must be increased. For this reason, the optimal frequency for inspecting CFRP is higher than for metals of the same thickness. By adjusting the frequency to suit the material conductivity, the inspection process can be optimized to ensure that subsurface defects are detectable within the desired depth range.

3.3 Numerical Methods

The accurate resolution of eddy current problems requires solving Maxwell's equations, which govern the behaviour of electromagnetic fields. These equations are inherently complex, particularly when applied to conductive materials with non-homogeneous properties or intricate geometries. To tackle such challenges, various numerical methods have been developed to approximate solutions.

This section explores the common approaches used to solve Maxwell's equations in eddy current problems. Initially, analytical methods are reviewed, highlighting their utility in specific scenarios with simplified geometries or boundary conditions. Despite their limitations, these methods offer valuable insights and can serve as reference for more advanced techniques. Following that, the FEM, the most widely used approach for solving complex eddy current problems, is discussed. FEM provides a versatile framework that allows for the discretization of complex domains, offering high accuracy and flexibility when dealing with real-world applications.

3.3.1 Analytical Methods

The first analytical solutions for the current-driven eddy current problem were derived by Dodd and Deeds [224] Dodd and Deeds provide an analytical solution for eddy-current problems involving a circular coil positioned above a semi-infinite conducting slab with a conductive coating as shown in **Figure 21**.

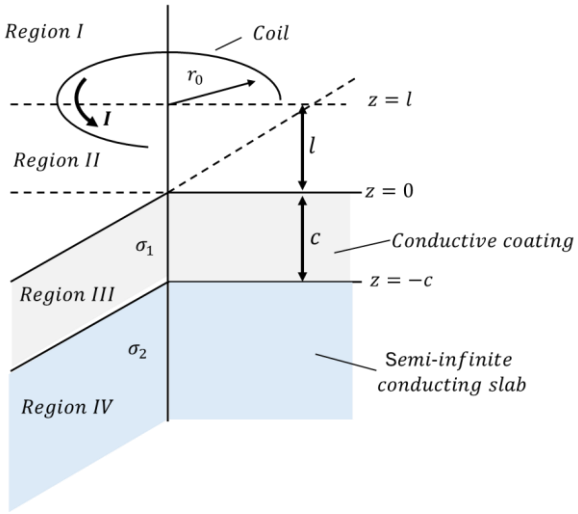

Figure 21 Coil above two-conductor plate (adapted from [224]).

The general solution involves solving the governing differential equation (31) but expressed assuming cylindrical symmetry:

$$\frac{1}{r}\frac{\partial}{\partial r}\left(r\frac{\partial A}{\partial r}\right)+\frac{\partial^2 A}{\partial z^2}-\frac{A}{r^2}-j\omega\mu\sigma A=0 \tag{41}$$

For a coil above a two-conductor plane, the solution $A(r,z)$ can be written as a superposition of Bessel functions of the first and second kinds J_1 and Y_1, that satisfy the boundary conditions. In cylindrical coordinates, the vector potential takes the following form:

$$A(r,z)=\int_0^\infty [C_1(a)e^{-\alpha_1 z}J_1(ar)+C_2(a)e^{\alpha_1 z}J_1(ar)]\,da \tag{42}$$

Where a is the variable of integration and $C_1(a)$ and $C_2(a)$ are constants that depend on the geometry and material properties of the conducting plane. The parameter $\alpha_1=\sqrt{a^2+j\omega\mu\sigma}$ represents the attenuation of the electromagnetic field as it penetrates the conducting medium.

For the case of a semi-infinite conductor or a conductor with a finite thickness, the boundary conditions at the interface between the air and the conductor, and possibly between the two conductors, must be applied. These boundary conditions ensure the continuity of the tangential components of the electric and magnetic fields at the interface.

The full solution, including the exact forms of $C_1(a)$) and $C_2(a)$, requires applying the boundary conditions specific to the two-conductor system and solving the integrals, which are often done numerically.

The vector potential is then used to calculate the physically observable electromagnetic quantities:

1. **Eddy current density** J:

$$J = -j\omega A \tag{43}$$

2. **Induced voltage V** in a single turn of the coil:

$$V = j\omega \int Ads \tag{44}$$

where the integral is taken over the area of the coil.

3. **Impedance of the coil:** The coil impedance can be calculated by relating the induced voltage to the current in the coil.

The pioneering analytical solutions developed by Dodd and Deeds for eddy current problems in isotropic materials have been extended to orthotropic materials, such as CFRP, by Bai et al. [225]. In their work, an analytical expressions for the vector potential was obtained, considering a circular drive current placed above a unidirectional CFRP plate, where the electrical conductivity is anisotropic. The conductivity of a unidirectional CFRP ply is described by a tensor, accounting for the directional properties of the material. The model is the same illustrated in **Figure 21** but in this case the conductivity $\overline{\sigma}_1$ of the region III is a tensor as expressed by the equation (21) for orthotropic materials. Assuming the fibers are aligned along the x-axis, the conductivity tensor can be expressed as:

$$[\overline{\sigma}_1{}'] = \begin{vmatrix} \sigma_l & 0 & 0 \\ 0 & \sigma_t & 0 \\ 0 & 0 & \sigma_{cross} \end{vmatrix} \tag{45}$$

where σ_l is the conductivity along the fibers, σ_t is the conductivity transverse to the fiber and σ_{cross} is the conductivity with overlapping of unidirectional layers. σ_{cross} becomes significant when multiple layers are stacked.
When fiber are oriented at an arbitrary angle θ as shown in **Figure 22**, the conductivity matrix is no longer diagonal and cross-coupling between components occurs. The transformed conductivity matrix is obtained using a rotational matrix $[R]$, which relates the rotated coordinate system to the original one:

$$[\overline{\sigma}_1] = [R^{-1}][\overline{\sigma}_1{}'][R] \tag{46}$$

where the rotational matrix is defined as:

$$[R] = \begin{bmatrix} cos\theta & sin\theta & 0 \\ -sin\theta & cos\theta & 0 \\ 0 & 0 & 1 \end{bmatrix} \quad (47)$$

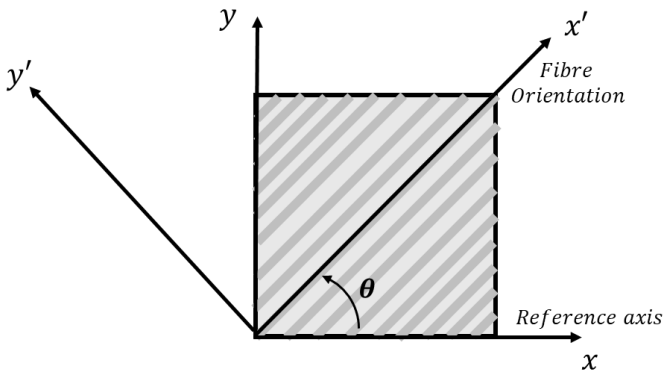

Figure 22 Relation between the principal axis, reference axis and fiber orientation.

Using the truncated region eigenfunction expansion (TREE) method, Bai et al. solved the vector differential equations by separation of variables, applying artificial magnetic insulation boundary conditions. The resulting series solution accurately captures the distribution of eddy currents in CFRP materials, demonstrating strong agreement with previous models, particularly in the anisotropic behavior of eddy currents along the fiber direction.

Following Bai et al., Mizukami et al.[226] developed analytical solutions for the eddy current distribution in CFRP induced by a line current. This approach differs from the circular current used by Dodd, Deeds, and Bai, addressing the anisotropic nature of CFRPs more effectively when subjected to a linear drive current. Mizukami's work highlights that the eddy current distribution in unidirectional CFRPs is dependent solely on the electrical conductivity in the direction of the drive current. Additionally, they showed that the skin depth of eddy currents is influenced not only by the frequency of the drive current but also by factors such as the lift-off and the width of the current source. The study further demonstrates that the sensitivity of eddy current sensors can be improved by optimizing the placement of the pickup coil in regions where the magnetic field from the eddy current dominates over that of the drive current.

While analytical methods provide valuable insights into eddy current problems, they are often limited by assumptions such as simplified geometries, homogeneity, and ideal boundary conditions. These methods can struggle to accurately model complex structures like CFRPs, where anisotropy, multi-layer configurations, and irregular geometries are prevalent. As a result, their applicability is constrained in many real-world scenarios. To overcome these limitations, numerical approaches such as the FEM offer a more versatile and accurate solution. FEM allows for the detailed modelling of complex geometries and material properties, making it an essential tool for analysing eddy current distributions in advanced materials like CFRPs.

3.3.2 Finite Element Method

For the vast majority of geometries and problems, the partial differential equations (PDEs) cannot be solved with analytical methods. Instead, different kind of discretization methods can be implemented in order to approximate the PDEs with numerical model equations. Among the different numerical techniques to solve electromagnetic problems, FEM yields stable and accurate solutions, is versatile, offers flexibility for modelling complex geometries and can handle nonlinearity well [22].

In FEM, the primary objective is to solve the vector potential equation for $\boldsymbol{A}$, which then allows for the derivation of related electromagnetic quantities such as $\boldsymbol{B}$, $\boldsymbol{J}$, $\boldsymbol{E}$ and $\boldsymbol{H}$.

Among the various methods employed in FEM formulations, two approaches are particularly common: the Galerkin method, a type of weighted residual technique, and methods based on energy functionals derived from the principle of energy conservation [227]. Instead of directly solving the governing differential equations, variational methods minimize an energy functional, which provides a practical framework for interpreting the physical behaviour of electromagnetic fields. This energy minimization approach simplifies complex electromagnetic problems and yields a clear physical interpretation. The general form of the energy functional for electromagnetic field problems is expressed as [227]:

$$\begin{aligned} \mathcal{F} &= magnetic\ field\ energy + electric\ field\ energy \\ &= stored\ energy + (dissipated\ energy - input\ energy) \end{aligned} \tag{48}$$

The energy stored within the system arises from the magnetic field, while the input energy is introduced through the applied current densities. Energy dissipation, on the other hand, occurs due to the eddy current densities within the conducting regions of the geometry. When expressed in terms of field variables, this energy relationship is represented by an energy functional, which captures the balance between stored, input, and dissipated energy:

$$\mathcal{F} = \int_v \frac{1}{2}\boldsymbol{H}\cdot\boldsymbol{B}dv + \int_v \frac{1}{2}\boldsymbol{J}\cdot\boldsymbol{A}dv \tag{49}$$

For the case of harmonic excitation, the equation is expressed as follows:

$$\mathcal{F} = \int_v \left[\frac{1}{2\mu}|\nabla\times\mathbf{A}|^2 + \frac{1}{2}j\omega\sigma|\boldsymbol{A}|^2 - \frac{1}{2}\boldsymbol{J_s}\cdot\boldsymbol{A}\right]dv \tag{50}$$

The integrand terms correspond to distinct energy contributions, namely, those associated with the magnetic field, eddy currents, and the source current densities ($\boldsymbol{J_s}$) respectively. For further details on deriving this expression, refer to [227].

The solution for the magnetic vector potential $\boldsymbol{A}$ is obtained by minimizing this functional with respect to $\boldsymbol{A}$, which provides the necessary conditions to resolve the field distribution in the system.

The next step in the finite element method involves subdividing the region of interest into smaller 2D areas or 3D volumes, referred to as **elements**, which are connected at specific points known as **nodes**. This process is called **discretization**. The energy

functional, once discretized, is expressed in the following in terms of the variable values at the mesh nodes in a Cartesian coordinate system (x, y, z):

$$\mathcal{F} = \sum_{i=1}^{n} \left[\frac{1}{2\mu} \left\{ \left| \frac{\partial A_{zi}}{\partial y} - \frac{\partial A_{yi}}{\partial z} \right|^2 + \left| \frac{\partial A_{xi}}{\partial z} - \frac{\partial A_{zi}}{\partial x} \right|^2 + \left| \frac{\partial A_{yi}}{\partial x} - \frac{\partial A_{xi}}{\partial y} \right|^2 \right\} + \frac{1}{2} j\omega\sigma |A_i|^2 - J_{si} \cdot A_i \right] \tag{51}$$

where *n* represents the total number of nodes in the solution region. To achieve energy equilibrium in the region, the energy functional is minimized for each individual element. This is done by setting the first partial derivative with respect to each component of the magnetic vector potential $\boldsymbol{A}$ at every node to zero:

$$\frac{\partial \mathcal{F}(A)}{\partial A_{ki}} = 0, \quad i = 1,2,3, \ldots\ldots n; \quad k = x, y, z \tag{52}$$

This results in a system of 3*n* simultaneous linear equations with 3*n* unknowns, which can be rearranged into a matrix form:

$$[G][A] = [Q] \tag{53}$$

In this expression, $[G]$ is a (3n x 3n) banded symmetric complex matrix, while $[A]$ and $[Q]$ are (3n x 1) complex column matrices. The **minimization** is performed **element by element**, and the **contributions** from all elements are **summed** to form the algebraic equations over the entire solution region. This assembly is carried out using the **connectivity matrix**, resulting in a **global matrix equation** in terms of all the unknowns in the system, which is solved for the nodal magnetic vector potential $\boldsymbol{A}$.

The system of equations is typically solved using standard techniques such as Gaussian elimination:

$$[A] = [G]^{-1}[Q] \tag{54}$$

Once the nodal values of **A** are obtained, they can be used to compute various physically measurable quantities, including the magnetic flux density $\boldsymbol{B}$, current density $\boldsymbol{J}$, electric field $\boldsymbol{E}$, and magnetic field $\boldsymbol{H}$.

3.4 Electrical properties of CFRP

CFRP are advanced materials composed of carbon fibres, which provide structural reinforcement, embedded in a polymer matrix, typically epoxy, that bonds the fibres and shapes the material. The carbon fibres, making up about 60% of the volume, are primarily responsible for the high strength and stiffness of CFRP, while the matrix provides resistance to environmental degradation and mechanical damage such as cracking and delamination.

CFRP comes in various configurations based on the fiber arrangement. **Unidirectional CFRP**, where fibers are aligned in a single direction, offers high strength along the fiber axis but displays significant anisotropy, meaning its properties vary greatly depending on the direction. To address this limitation, **multi-directional laminates** are produced by

stacking unidirectional layers in different orientations, which improves overall mechanical strength and balances directional properties. **Woven CFRP** is another configuration where fiber bundles are interwoven in multiple directions, similar to fabric, providing enhanced impact resistance and durability due to the interlocking fibre structure.

This variety of configurations allows CFRP to be tailored for different applications, though the anisotropic nature of these materials, particularly in their electrical properties, plays a significant role in determining their behaviour in various industrial applications.

Electrical properties of CFRP

CFRP exhibits electrical conductivity primarily due to the carbon fibres embedded in the composite. However, the distribution of eddy currents within CFRP laminates is strongly anisotropic, as the fibres **touch at various points** within the matrix, forming an electrical network (**Figure 23 (a)**). When two fibers in a CFRP laminate make contact, they create a conductive loop that facilitates the flow of eddy currents when exposed to an electromagnetic field. At lower frequencies, typically in the range of hundreds of kHz to a few MHz, the high capacitive reactance of the polymer matrix restricts significant current flow across it. As the frequency increases beyond the MHz range, the capacitive reactance diminishes, allowing capacitive coupling between fibers to become the preferred path for current flow.

In this context, **Figure 23 (b)** illustrates the elementary current flow within unidirectional CFRP, where R_f represents the fiber resistance and $Zc = RC + 1/j\omega C_m$ defines the impedance between fibers, with RC being the contact resistance and C_m the coupling capacitance.

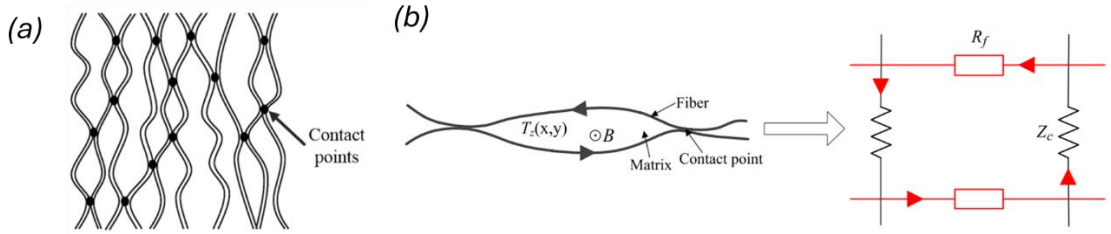

Figure 23 (a) Contact points between parallel fibers [228]. (b) Elementary impedance circuit in unidirectional laminate [229].

Electrical conductivity in CFRP depends on various factors such as fibre volume fraction, ply stacking sequence, and environmental conditions like temperature and humidity. In unidirectional CFRP, conductivity along the fibre direction ranges from 5×10^3 to 5×10^4 S/m, while in the transverse direction, it drops to 10–100 S/m [226]. The conductivity through the thickness is even lower due to the resin-rich interlaminar regions.

In cross-ply CFRP laminates, the carbon fibres from adjacent layers overlap at their interfaces, forming interconnected loops. These orthogonal fibres create a closed current loop, as depicted in **Figure 24**, where the current paths are indicated by arrows. The flow of eddy currents between neighbouring layers occurs through contact points and capacitive coupling among fibre bundles in the thickness direction. This interlaminar connectivity allows for current flow even across the resin-rich interlaminar regions, despite their lower conductivity, enhancing the overall conductive behaviour of the

laminate in multi-directional configurations. This significant variation highlights the strong electrical anisotropy of CFRP.

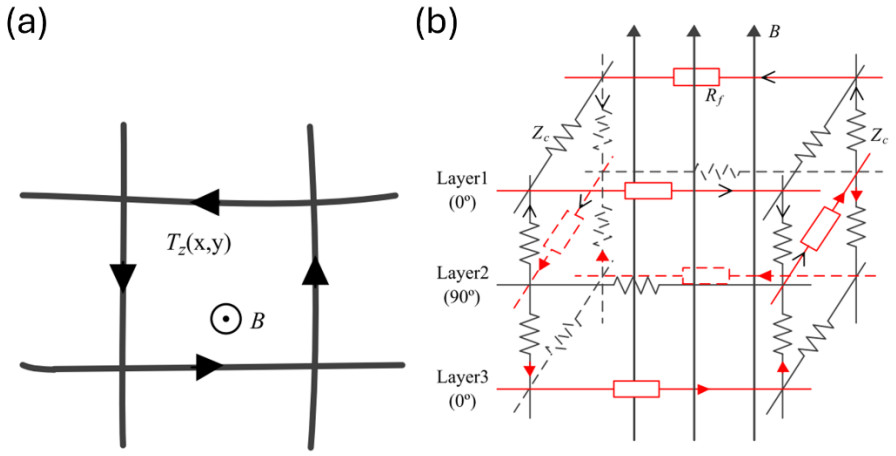

Figure 24 Representation of (a) eddy current flow and (b) impedance network in orthogonal CFRP laminate [229].

In the case of laminated CFRP, the skin effect for alternating electric current differs significantly from that in homogeneous isotropic materials due to the anisotropic nature of its electrical properties. Todoroki's work [223] demonstrates that the skin effect depth for CFRP can be described using Maxwell's equations while taking into account the orthotropic conductance of the material. Todoroki modifies the equation for penetration depth (equation 40) to account for the layered and anisotropic nature of CFRP, considering different conductivities for each direction. In CFRP, the depth of penetration for the transverse or through-thickness direction becomes:

$$\delta_{CFRP} = \frac{1}{\sqrt{\pi f \mu \sigma_t}} \tag{55}$$

This equation illustrates that the lower transverse conductivity in CFRP leads to a shallower penetration depth compared to metals. For laminated structures, such as cross-ply configurations, the overlap of orthogonal fibres creates complex current loops through capacitive coupling, which further affects the depth of penetration.

As Todoroki demonstrates, higher frequencies are required in CFRP to achieve the same depth of penetration as in metals. This highlights the importance of selecting the appropriate frequency to ensure effective eddy current testing, particularly when dealing with the low transverse and through-thickness conductivities of CFRP.

3.5 Electrical conductivity variation due to FSW microstructure

In FSW, the material undergoes significant microstructural transformations, which directly impact its electrical conductivity. These variations arise from the thermal and mechanical processes intrinsic to FSW, leading to distinct microstructural zones across the weld—each with unique characteristics.

FSW involves plastic deformation at high temperatures, which produces a distinct weld structure comprised of three main zones (see **Figure 25**): the Stir Zone (SZ) or nugget, the Thermo-Mechanically Affected Zone (TMAZ), and the Heat-Affected Zone (HAZ). The stir zone, located at the center of the weld, is subject to intense mechanical

stirring, leading to grain refinement and dynamic recrystallization. The surrounding TMAZ experiences both thermal exposure and deformation, though less intense, while the HAZ is exposed primarily to heat without mechanical deformation, causing over-aging or softening of the material in heat-treatable alloys like the 6000 series.

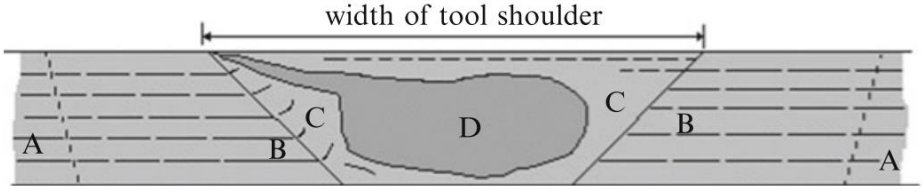

Figure 25 Various microstructural region in the transverse cross-section of a friction stir welded joint. A=base material, B=HAZ, C=TMAZ, D=SZ [5].

These microstructural changes have a direct effect on the electrical conductivity of the material. Electrical conductivity serves as an indirect indicator of microstructural properties, as it is sensitive to the presence of grain boundaries, dislocations, and precipitates [230]. As the FSW process alters these features, the electrical conductivity field across the weld varies accordingly.

- **Stir Zone (SZ):** The SZ typically experiences grain refinement due to dynamic recrystallization. Fine grains increase the overall grain boundary area, which scatters electrons, leading to a reduction in electrical conductivity. However, in heat-treatable aluminum alloys, the dissolution of precipitates during FSW can enhance electrical conductivity in this region by reducing electron scattering due to precipitate boundaries [231]. This phenomenon is particularly significant in alloys where precipitate distribution influences the conductivity, as demonstrated by studies on aluminum 6000 series alloys [231], [232].

- **Thermo-Mechanically Affected Zone (TMAZ):** In the TMAZ, the microstructure is partially deformed and experiences some grain refinement, though not as pronounced as in the SZ. The electrical conductivity in this region typically exhibits intermediate values between the stir zone and base material, as it reflects a combination of both mechanical deformation and thermal exposure [233].

- **Heat-Affected Zone (HAZ):** The HAZ is subject to thermal cycles without significant plastic deformation. In heat-treatable alloys, this often leads to over-aging, where the dissolution and coarsening of precipitates affect electron mobility. Coarser grains, as demonstrated by Cui et al. [231], tend to enhance conductivity by reducing the grain boundary surface area, thus improving electron flow . Conversely, the coarsening of precipitates can lead to a localized decrease in conductivity due to increased scattering at these larger boundaries.

Assessing electrical conductivity provides a powerful non-destructive method for evaluating the FSW process and understanding the microstructural changes it induces. The correlation between electrical conductivity and microhardness is particularly valuable, as both properties are influenced by the underlying microstructure, yet offer different insights. Electrical conductivity is governed by electron mobility, while hardness reflects the material resistance to plastic deformation, which is controlled by factors such as crystal structure, second-phase particles, dislocations, and grain size [66].

As shown in **Figure 26**, which compares the profiles of electrical conductivity and Vickers hardness across an AA7075-T6 FSW joint, there is a consistent relationship between the two properties. The hardness is affected by the presence of dislocations and the distribution of precipitates, which hinder crystal defect mobility, while electrical conductivity is more directly related to the ease with which electrons move through the material [66]. Despite these differences, a scale factor exists between these two properties because they both depend on the microstructure of the weld.

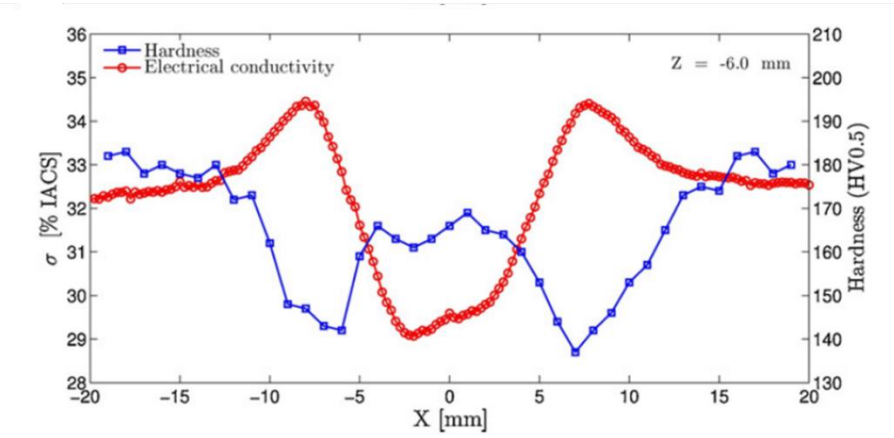

Figure 26 Comparison of the electrical conductivity and Vickers hardness profiles on a AA7075-T6 FSW joint [66].

Electrical conductivity measurements, however, offer greater precision in capturing small-scale microstructural variations [230]. In contrast, hardness measurements, such as Vickers microhardness, are more discrete due to the constraints of indentation testing, where standards like ISO 6507-1:2005 require a significant spacing between indentations [66]. This means that while hardness testing provides crucial qualitative information about mechanical strength, conductivity can offer a more detailed mapping of microstructural homogeneity. By correlating conductivity measurements with microstructural features such as grain size and precipitate distribution, it is possible to infer the mechanical properties of the weld, particularly hardness and strength, offering an effective alternative or supplement to traditional mechanical testing methods like hardness tests.

3.6 Summary of Chapter 3

Chapter 3 establishes a theoretical framework for the analysis of electromagnetic behavior in materials, specifically under quasi-static conditions where displacement currents are negligible. The simplification of Maxwell's equations for these scenarios is discussed, with particular emphasis on ECT as a key non-destructive evaluation technique. The chapter also addresses the complexities of anisotropic materials such as CFRP, where the directional variation of electrical conductivity plays a crucial role in determining current distribution and penetration depth, especially in cross-ply laminates.

A detailed discussion is provided on numerical methods, notably FEM, for solving Maxwell's equations in complex material systems. The chapter further explores the correlation between electrical conductivity and microstructural properties FSW, highlighting that changes in conductivity serve as indirect indicators of microstructural transformations. Variations in conductivity are linked to key factors such as grain size,

dislocation density, and precipitate distribution, providing a non-destructive method for assessing weld quality. This correlation is particularly useful as a complement to traditional mechanical testing methods such as hardness assessments, enabling a more precise evaluation of the microstructural integrity of FSW joints.

In conclusion, Chapter 3 links the theoretical foundations of electromagnetic analysis with the practical applications of ECT and microstructural evaluation, providing a basis for the experimental and numerical investigations that follow in the subsequent sections.

Chapter 4

4 Materials and Methods

Chapter 4 outlines the comprehensive approach undertaken to meet the research objectives, including both the design and experimental validation of monitoring systems for FSW and thermoplastic induction welding. The chapter begins by presenting the core methodology, highlighting the inputs, requirements, and numerical methods essential to the development of the ECT probes and EM sensors, which were designed for real-time process monitoring and SHM, respectively.

The subsequent sections focus on the experimental hardware used in two case studies. *CASE I* explores the material selection, fabrication of test specimens, complementary NDT, and ECT system setup for FSW defect detection. *CASE II* shifts the focus to thermoplastic welded joints, detailing the material selection, mechanical testing, sensor performance evaluation, and damage detection setup

4.1 Methodology

4.1.1 Inputs and requirements

This section details the specific inputs and technical requirements for the design and development of ECT probes intended for real-time process monitoring and EM sensors for SHM applications. Additionally, it addresses the selection of an optimal excitation frequency range necessary to achieve precise defect detection in aluminium alloys and CFRP laminates, ensuring comprehensive material evaluation and accurate monitoring of weld quality.

ECT Probe Requirements for Real-Time Process Monitoring

In designing an ECT probe for potential real-time process monitoring of FSW, several critical requirements must be addressed to ensure optimal performance, particularly in terms of sensitivity to variations in electrical conductivity. This is especially relevant in the context of correlating microstructural changes with weld quality, which forms a central theme of this work. The following requirements were considered:

- **Sensitivity to electrical conductivity variations**: The probe must exhibit high sensitivity to detect subtle changes in conductivity that arise from microstructural transformations such as grain refinement and precipitate dissolution. This sensitivity is crucial for establishing a correlation between conductivity and key weld properties, such as hardness and mechanical strength, providing an accurate and non-destructive means of assessing weld quality in real time.

- **Defect detection capability**: The probe must be capable of detecting flaws as small as 0.5 mm, in accordance with standards such as ISO25239-5 for FSW joints [234].

- **Through-Thickness Inspection Capability**: The probe should be designed to assess the full thickness of the material, with the ability to detect subsurface

defects, including wormhole/tunnel defects, even on the opposite side of the weld. This feature is essential for ensuring comprehensive quality control, particularly in industrial applications where both sides of the weld may not be accessible.

- **Signal-to-Noise Ratio (SNR)**: To guarantee reliable and unambiguous defect detection, the probe must achieve a Signal-to-Noise Ratio (SNR) of at least 3. This ensures that the signal response to defects significantly exceeds background noise, enabling accurate real-time monitoring under various operating conditions.

- **Minimization of the edge-effect**: The design of the probe must account for and minimize the edge effects that can distort eddy current flow near the edges of the weld or part. Reducing these distortions is crucial to avoid misinterpretation of signals and missed defect detection, particularly in complex geometries common in industrial applications.

- **Integration and practical application**: The probe must be compatible with existing FSW equipment, facilitating its use in industrial settings.

EM Sensor Requirements for SHM Applications

When developing an **EM sensor** for SHM of **thermoplastic induction welded joints**, several key requirements must be addressed to ensure optimal performance. The primary focus lies in ensuring sensitivity to changes in electrical conductivity and dielectric permittivity, which directly correlate with damage such as delamination or reduced contact area at the welding interface. The following requirements were considered:

- **Planar or flat design**: The sensor should feature a planar or flat configuration, allowing it to be easily attached to the surface or embedded within the CFRP layers.

- **High sensitivity to changes in conductivity and permittivity**: The sensor must be capable of detecting even minor changes in electrical conductivity and dielectric permittivity, which are indicative of damage such as delamination at the welding interface. Sensitivity to these variations is necessary for establishing robust correlations between the sensor response and the structural integrity of the joint, aiding in the prediction of residual useful life.

- **Capability to track damage progression**: The sensor should not only detect the presence of damage but also provide a measurable signal that changes in response to the **size, location, and type** of damage. This functionality allows for the establishment of a correlation between the sensor signal and the progression of the defect. Such sensitivity to the evolution of damage is crucial for building predictive models that can translate these signals into estimates of the remaining life of the joint.

- **Wide Frequency Range Capability:** The sensor must be capable of operating across a broad range of frequencies, allowing for effective detection of both surface and subsurface defects. Lower frequencies enable deeper penetration into the material, while higher frequencies provide enhanced surface resolution. This flexibility ensures optimal sensitivity for monitoring varying damage

characteristics in thermoplastic welded joints, especially for complex materials like CFRP, where conductivity and permittivity vary with frequency.

Frequency Range for Excitation

In defining the **optimum range of excitation frequency** for ECT, the key objective is to ensure that the eddy currents penetrate the material with sufficient intensity to thoroughly assess the **entire weld**. The penetration depth, as governed by equations (40) for isotropic material and (55) for anisotropic materials like CFRP, helps to define the necessary frequency range to achieve this coverage, ensuring that variations in the material microstructure or conductivity, which might indicate flaws or defects, are reliably detected.

The selection of appropriate frequencies is based on the specific properties and thicknesses of the 6082-T6 aluminum alloy and CFRP laminates used in this research, ensuring optimal sensitivity and accuracy in the weld assessment process.

As depicted in **Figure 27**, the penetration depth is shown as a function of frequency for both materials. The differences in electrical conductivity significantly affect how deeply the induced eddy currents can penetrate. **6082-T6 aluminum** has a relatively high conductivity (**24224 kS/m** [235]), which results in shallow penetration depths at higher frequencies, requiring lower frequency ranges for effective subsurface detection. In contrast, the **CFRP** laminate used in this study has a transverse conductivity of **10.6 kS/m**, typical of woven carbon fiber fabrics like the five-harness satin weave with a PPS polymer matrix [236].

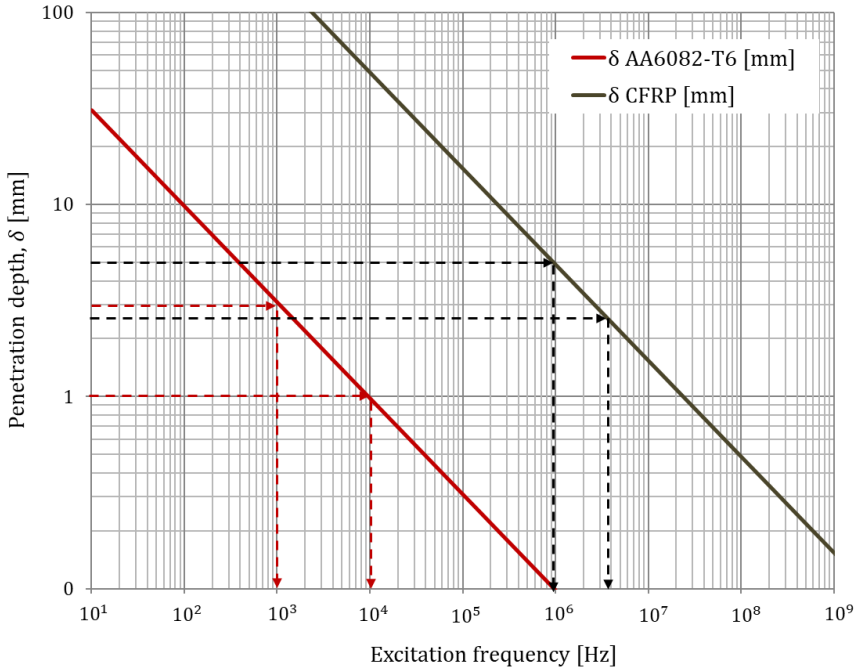

Figure 27 Penetration depth as a function of excitation frequency for 6082-T6 aluminum and CFRP laminates.

In the graph, the target thickness is used as an input to determine the necessary excitation frequency in order to obtain the required excitation frequency. This ensures that the eddy currents have sufficient intensity to fully cover the material depth, enabling comprehensive inspection and defect detection across the weld.

Commonly, aluminum alloy plates used in airframes range from 1 mm to 10 mm [237], depending on the structural role, with non-load-bearing fuselage skins typically being thinner and highly stressed components like landing gear being thicker. CFRP laminates, widely employed in areas requiring high strength-to-weight ratios, generally range from 2 mm to 6 mm [238]. For instance, CFRP is used in wings, tail sections, and fuselage panels.

In this research, the **material thicknesses** selected for study are:

- **3 mm** for 6082-T6 aluminum alloy plates welded by FSW in butt joint configuration.
- **2.54 mm** for CFRP laminates welded in lap joint configuration by thermoplastic welding.

For 6082-T6 aluminum alloy welded joints, the frequency must be selected to ensure a penetration depth of **1 mm to 3 mm**, depending on the specific inspection requirements. If high sensitivity to subsurface defects is needed, higher frequencies should be used to target shallow areas. Conversely, to detect defects on the opposite side of the weld, lower frequencies are required. This translates to a frequency range of **1 to 10 kHz** for optimal inspection across the material thickness. In the case of **CFRP**, particularly in a lap joint configuration, it is crucial to achieve at least **2.54 mm** penetration to assess the welded interface effectively, with an ideal depth reaching **up to 5 mm** for comprehensive coverage, if necessary. Given the lower conductivity of CFRP, the appropriate frequency range would typically fall between **1 to 4 MHz**, ensuring comprehensive assessment of the weld area.

Numerical simulations and experimental evaluations are conducted not only within this defined frequency range but also in surrounding ranges, as the penetration depth formulas are based on certain simplified assumptions and geometries.

4.1.2 Numerical methods

The primary objective of the numerical simulations is to guide the design process of the probes and sensors, optimizing their performance for specific applications. These simulations serve two key purposes: (1) to replicate the operation of the probe or sensor in order to analyze the distribution of eddy currents and the corresponding magnetic fields in the presence or absence of defects, and (2) to conduct sensitivity studies by varying critical design parameters, such as the slenderness of the coils, enabling the exploration of different probe configurations. By employing FEM simulations, the distribution of eddy currents and the probe sensitivity to various defect types can be better understood, ensuring that the final design maximizes detection capabilities in both real-time process monitoring and structural health monitoring scenarios.

Numerical simulations were performed using **COMSOL® Multiphysics**, utilizing the **AC/DC module** to conduct a frequency-domain analysis. The AC/DC module solves the governing equation (31), which is particularly suited for electromagnetic problems where the **quasi-static approximation** applies. As reported previously, this approximation holds when the characteristic size of the device (L_c) is significantly smaller than the wavelength of the propagating electromagnetic radiation (λ). This condition is typically expressed by the following relation:

$$L_c < \lambda/10 \tag{54}$$

Under the quasi-static assumption, variations in the electromagnetic field propagate instantaneously across the device, with wave-like phenomena becoming negligible. During the course of the current research, the largest dimension of the model was **50 mm**, and the maximum excitation frequency was **100 MHz**, which corresponds to a value of λ equal to **2.3 meters**. This wavelength is much larger than the size of the model, ensuring that the **quasi-static hypothesis** is fully satisfied, and wave propagation effects can be safely ignored (see **Figure 28**).

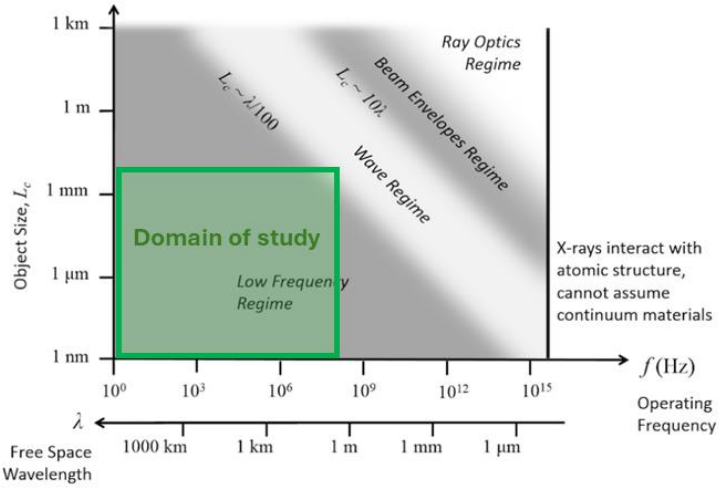

Figure 28 Study domain validating the quasi-static hypothesis for the present research (adapted from [239]).

In this study, the coil was modeled using two different approaches within COMSOL Multiphysics depending on the application and the computational needs [239]:

- the **Single Conductor Model** and
- the **Homogenized Multi-Turn Model**.

For probes and sensors with a large number of turns, the **Homogenized Multi-Turn Model** is employed to minimize computational costs while accurately capturing the electromagnetic behavior. As shown in **Figure 29**, this model represents coils as tightly wound wires and allows the analysis of their overall effect without modeling each turn individually, thus optimizing simulation performance. However, this method neglects certain physical effects, such as capacitive coupling and skin effect, due to the lack of detailed individual wire modeling.

In the case of coil configurations involving fewer conductor elements, the **Single Conductor Model** is generally employed. This model accounts for the physical behavior of a solid conducting material, allowing for a more detailed analysis of the current flow and resulting magnetic fields. This approach provides better accuracy in cases where detailed geometry and localized current distribution are critical for defect detection and sensor sensitivity.

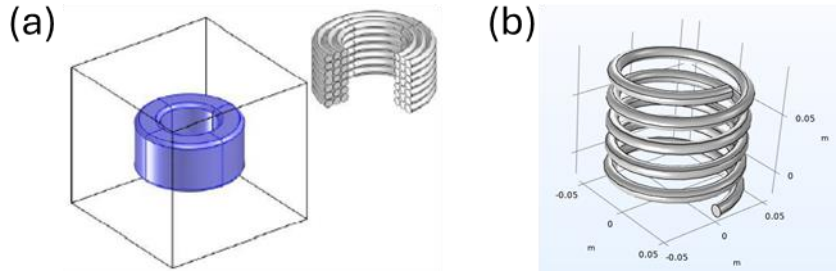

Figure 29 (a) Homogenized Multi-Turn Model and (b) Single Conductor Model [239].

Both models allow for two types of excitation: **current excitation** and **voltage excitation**. **Table 6** presents a summary of the key equations used for current and voltage excitation in both the homogenized multi-turn model and the single conductor model. The table highlights the relationships between the applied current, voltage, coil geometry, and other relevant parameters.

Table 6 Equation for current and voltage excitation for Homogenized Multi-Turn and Single Conductor Model [239].

Homogenized Multi-Turn Model	
Current excitation ($\boldsymbol{I_{coil}}$)	Voltage excitation ($\boldsymbol{V_{coil}}$)
$$J_e = \frac{N\boldsymbol{I_{coil}}}{A} \quad (55)$$ where: J_e = External current density in the direction of the wires N = Number of turns A = Cross sectional area of the coil domain	$$J_e = \frac{N(\boldsymbol{V_{coil}} + V_{ind})}{AR_{coil}} \quad (56)$$ where: J_e = External current density in the direction of the wires N = Number of turns A = Cross sectional area of the coil domain V_{ind} = Induced voltage calculated by integrating the electric field along the coil R_{coil} = total resistance of the coil calculated as $$R_{coil} = \int_A \frac{NL}{\sigma_{coil} a_{coil} A} \quad (57)$$ $\sigma_{coil} a_{coil}$ is the product of the wire bulk conductivity and wire cross-section area and L is the coil length
Single Conductor Model	
Current excitation ($\boldsymbol{I_{coil}}$)	Voltage excitation ($\boldsymbol{V_{coil}}$)
$$E_e = \frac{V}{L} \quad (58)$$ where: E_e = External electric field applied by the coils in the direction of the current flow V = Unknown potential voltage solved by constrains the total integrated current to be equal to the current values $\boldsymbol{I_{coil}}$ specified. L = Coil length	$$E_e = \frac{V_{coil}}{L} \quad (59)$$ where: E_e = External electric field applied by the coils in the direction of the current flow L = Coil length

For the homogenized multi-turn model, the external current density is calculated based on the number of turns and the cross-sectional area of the coil, ensuring that the

distribution of current in the wire bundle is properly represented. In contrast, for the single conductor model, the external electric field applied along the coil length is determined, reflecting the behavior of a solid conductor with a lumped current or voltage.

During this investigation, **homogenization techniques** were applied to the ECT probes, which involved a large number of turns to reduce computational complexity while maintaining accuracy. In contrast, the **Single Conductor Model** was used for the EM sensors for SHM applications due to their simpler geometry and fewer conductor elements, enabling precise modeling of the sensor electromagnetic characteristics. These methods provided the necessary balance between computational efficiency and the accuracy needed to capture the key phenomena related to defect detection and material properties.

To ensure the accuracy and reliability of the models employed, a validation process was undertaken using an aluminum plate with a pre-defined crack as the test base for the ECT probe. This allowed for the verification of the model performance before conducting a full parametric study. The results reported in Section 5.1.1 confirm that the model effectively captures the essential features of the eddy current distribution and defect sensitivity.

Regarding the EM sensor developed for SHM applications, the validation of the model relied heavily on how the electrical properties of CFRP were represented. As illustrated in **Figure 30**, different modeling strategies were considered based on the level of material detail. The most computationally intensive model involves explicitly defining the fiber and resin (**Figure 30 (a)**), whereas a simpler, homogeneous material model, with appropriately defined sigma, epsilon, and mu tensors, offers computational efficiency (**Figure 30 (b)**). An intermediate approach models each layer of CFRP with specific tensors for sigma, epsilon, and mu (**Figure 30 (c)**).

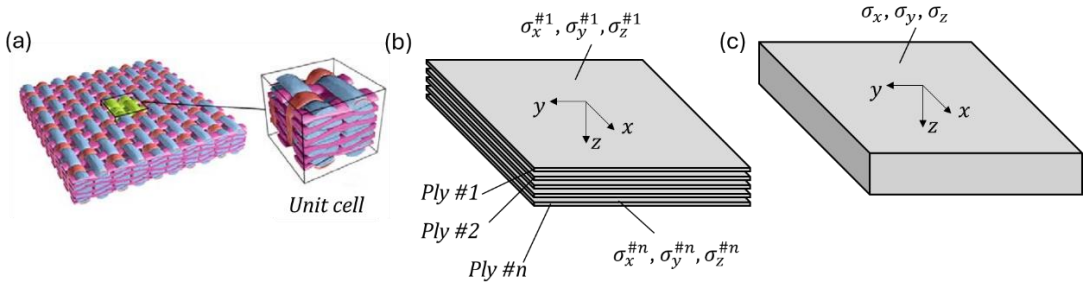

Figure 30 Approaches for modeling CFRP electrical properties: (a) fiber-resin detailed model [240], (b) ply-level homogeneous model with specific conductivity tensors, and (c) fully homogenized laminate model.

In accordance with the methodology outlined in Article 1 (section “Numerical methods”), the initial approach was to model the material as homogeneous. Nevertheless, the discrepancy between this model and experimental data led to further refinement by incorporating material anisotropy. This adjustment brought the model behavior closer to experimental reality, as detailed in both the "Experimental" section and in Figure 13 of Article 1. The validation results underscore the importance of accurately representing material anisotropy and in particular the importance to properly characterize the electrical conductivity of the CFRP used.

4.1.3 ECT probe for real time process monitoring

Given the specific requirements outlined for ECT probes in real-time monitoring applications, the decision to employ an **absolute probe with a double-function configuration** was driven by the following key factors.

Firstly, the absolute probe offers significant advantages in terms of sensitivity to electrical conductivity variations, which is a central focus of this work. Absolute probes are highly responsive to subtle conductivity changes caused by microstructural transformations such as grain refinement and precipitate dissolution. This feature is critical for establishing a reliable correlation between conductivity and important weld properties, such as hardness and mechanical strength, allowing for accurate and non-destructive real-time weld quality assessments.

Moreover, unlike differential probes, which are more suitable for detecting gradual changes, absolute probes excel in identifying abrupt variations in conductivity, making them particularly effective in detecting defects such as cracks and voids. This heightened sensitivity to sudden changes is crucial in FSW applications, where localized defects can have significant implications for the overall integrity of the weld.

When configuring ECT absolute probes, several critical parameters must be carefully evaluated to optimize performance (see **Figure 31**):

- Number of turns (N)
- Probe radius (r_o)
- Probe height (b)
- Coil slenderness ratio (b/h)**)**

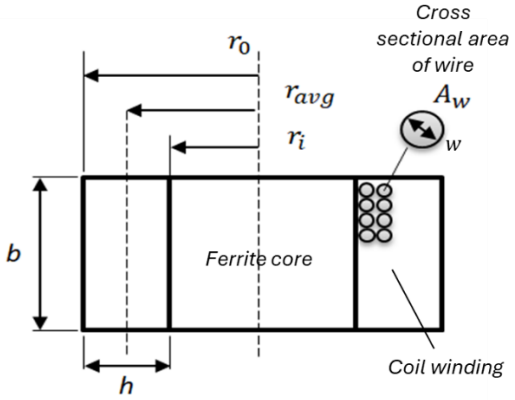

Figure 31 Main parameters of ECT absolute probe.

In adjusting these parameters, particular attention was given to the **fill factor**, which is the ratio of the area occupied by the electrical conductors to the total space available in the winding. The **fill factor** is always less than one due to gaps between the round wires and the necessary insulation between turns and layers. It can be calculated using the following formula, which relates the **cross-sectional area of the wire (including insulation)**, denoted as A_w, the number of turns N, and the coil dimensions (length b and width h):

$$F = \frac{A_w \cdot N}{b \cdot h} \tag{60}$$

Figure 32 presents curves corresponding to constant fill factor values for different numbers of turns. These curves were used to graphically determine the appropriate coil slenderness ratios. Each curve assumes a **fill factor** of **0.78**, which represents the theoretical limit for round wires. For any given number of turns, the feasible combinations of b and h lie above these curves, as values below indicate insufficient space for winding the specified number of turns within the coil.

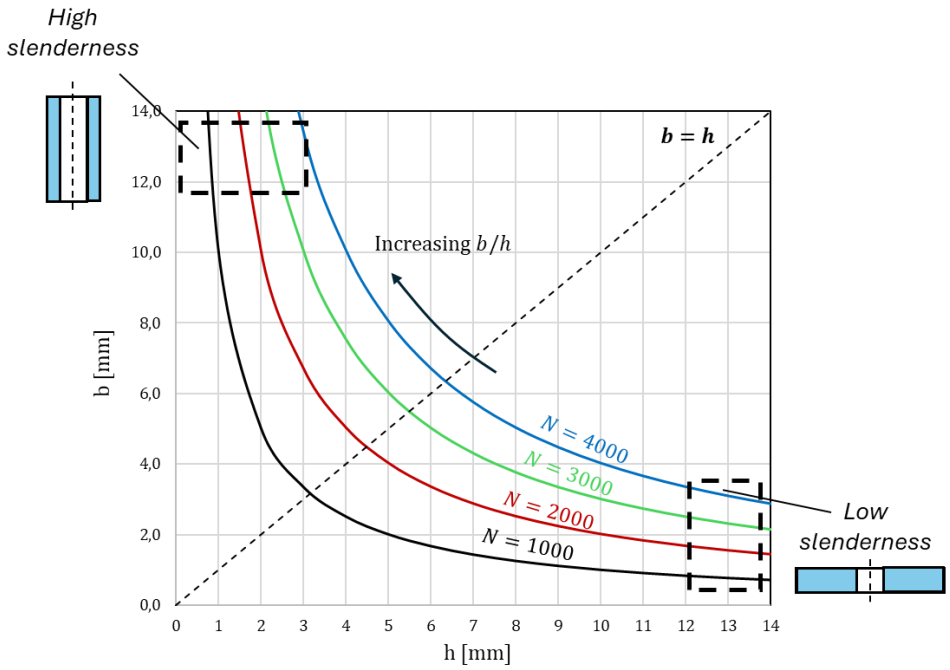

Figure 32 Curves at a constant filling factor of 0.78, theoretical limit for round wires.

Considering these factors, a series of simulations were conducted to assess the impact of varying parameters (N,b and h) on the probe sensitivity for detecting a defect positioned on the surface opposite to the ECT probe, as depicted in **Figure 33**. The defect was modeled with a height of **0.5 mm**.

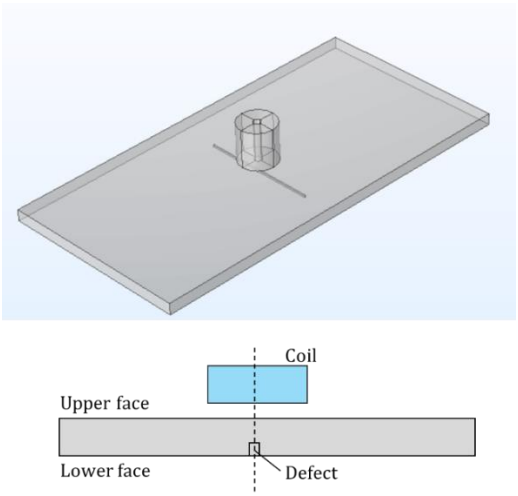

Figure 33 Numerical model employed during the sensitivity analysis of parameters N,b and h.

For each configuration, simulations were performed both with and without the defect in order to quantify changes in the probe impedance. The defect was modeled as a slot, with air conductivity assigned in the presence of the defect and aluminum conductivity assigned in its absence. To ensure the consistency of the results, the **geometry** and **mesh** were kept constant throughout the simulations, eliminating any potential influence of these factors on the outcomes.

Several parameters were held constant during the simulations, including the ferrite core radius of 1 mm (r_i) and the wire diameter of 0.1 mm (w). The combinations of N,b and h were chosen under the condition of maintaining a **constant fill factor** of **0.78**. This constraint implies that the N/bh **ratio** remains constant for all configurations, as dictated by the equation governing coil design. Additionally, the model used for the homogenized multi-turn coil follows Equation (55), and with a constant 1 A current, the current density is also fixed across all cases.

Thus, varying N,b and h results in different current distributions in space, with the objective of identifying the configuration that maximizes the probe sensitivity to the defect.

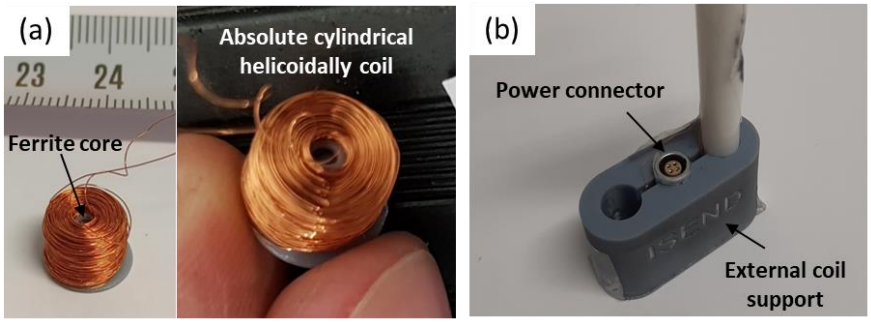

Figure 34 (a) Absolute cylindrical helicoidal probe used for conductivity measurements. (b) External support structure and power connector.

Table 7 Parameters of the manufactured ECT probe.

Coil parameters	
Wire diameter ,w [mm]	0.1
Ferrite radius, ri [mm]	1
Coil diameter, d [mm]	10
Number of turns, N [mm]	1230
Coil height, b [mm]	10
h	4
Fill factor, F	0.24

Section 5.1.1 presents the numerical simulations and corresponding analysis that lead to the definition of the optimal probe design parameters. These results guided the fabrication of the probe, as illustrated in **Figure 34**, with the finalized specifications detailed in **Table 7**. The combination of these parameters ensures that the probe meets the required sensitivity and performance for its intended application, as demonstrated by the results discussed in Section 5.1.

4.1.4 EM sensor for SHM application

The design of the EM sensor for SHM of thermoplastic induction welded joints was primarily driven by the need for a planar sensor configuration that could be easily attached to the surface of the joint or embedded within composite laminates.

A key design decision involved separating the electromagnetic field excitation and measurement into distinct elements to allow for independent optimization of each function. This approach ensured that both the excitation and sensing components could be fine-tuned for their respective roles, maximizing the sensor overall performance. The **excitation element** was represented by a **single-loop antenna**. The rationale behind this choice is the antenna capability to operate effectively not only in the low-frequency regime, where inductive phenomena dominate but also in high-frequency applications, where electromagnetic wave propagation becomes significant. Although the high-frequency operation was not a primary focus of the present research, the versatility of this design allows for future exploration of both regimes.

For **sensing**, **two distinct measurement methodologies** were employed to investigate the interaction between the changes in electrical properties of CFRP due to damage. The first method involved **measuring the magnetic field** using a sensing loop positioned on both the same side as the excitation loop (**reflection response**) and the opposite side (**attenuation response**) as shown respectively in **Figure 35 (a)** and **Figure 35 (b)**. In the preliminary phase, numerical simulations were conducted to optimize the design parameters of the excitation and sensing loops, such as the loop diameter respect to damage sensitivity.

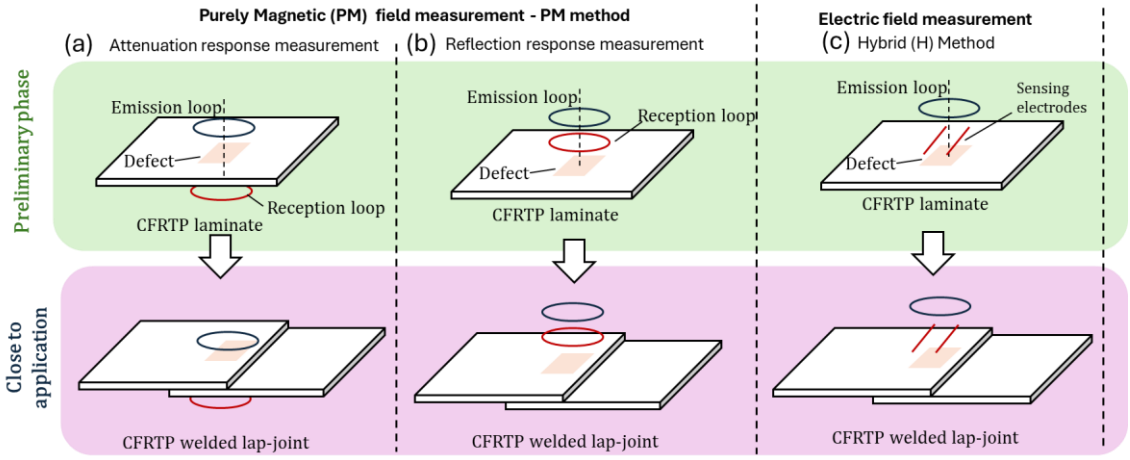

Figure 35 Methods for investigating electrical property changes in CFRP: (a) Magnetic Attenuation, (b) Magnetic Reflection, (c) Hybrid Approach.

By employing a simplified 2D model, the simulation allowed for efficient exploration of the electromagnetic response under different configurations while reducing computational costs. The results guided the definition of trade-off parameters, which are further detailed in the Section 5.2.1 and in "*Results and discussion - Numerical*" section of **Article 1.** Moreover, in **Article 1,** the comparison between attenuation and reflection methodologies was extended with a 3D model that accurately captures the geometry of the lap joints and approximates real experimental conditions. The analysis revealed that, despite its potential benefits, the attenuation response presented a significant limitation: it required access to both sides of the welded joint. In aerospace applications, such as airframe structures, this presents a critical challenge. Positioning sensors on the outer

surface could interfere with aerodynamic performance, increasing drag and compromising the design. These constraints led to the exclusion of the attenuation method in favor of the reflection approach, which only requires access to one side of the joint.

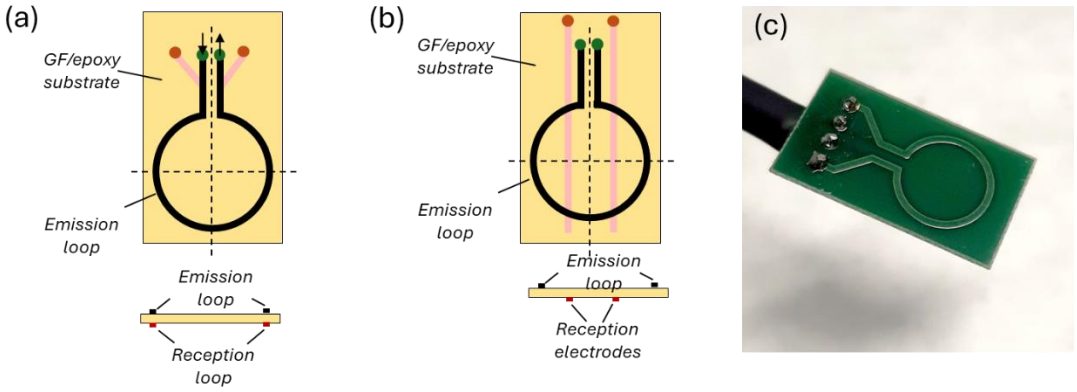

Figure 36 Schematic representation of (a) PM and (b) H sensor. (c) Photo of manufactured PM sensor.

The **second methodology** used to detect damage involved measuring the **changes in the electric field** due to defects, using a pair of **sensing electrodes** as shown **Figure 35 (c)**. These electrodes provided a complementary perspective on the detection process, enhancing the sensor sensitivity to changes in the dielectric properties of the material. **Figure 36** illustrates the schematics and photographs of the optimized sensors for both approaches. A detailed comparison of these two methodologies, including their sensitivity to damage, advantages, and limitations, is presented in **Article 2**.

4.2 CASE I: Experimental Hardware

The experimental setup employed in this case study was designed to establish a robust correlation between welding parameters, electrical conductivity, and mechanical properties. This represents a crucial preliminary step for ensuring the feasibility of future real-time process monitoring in FSW applications. The following section outlines the materials used, the characterization techniques applied, and the configuration of the hardware designed to evaluate conductivity and detect defects, ensuring a comprehensive analysis of the weld quality.

4.2.1 Material Selection and Test Specimen Fabrication

The material used for the experimental study is 6082-T6 aluminum alloy, presented as rolled plates with a thickness of 3 mm. Mechanical properties such as yield strength, ultimate tensile strength, and elastic modulus were determined according to ISO 6892-1 standards, and further detailed information about the chemical composition and mechanical properties of this base material can be found in **Table 1** and **Table 2 of Article 3**. This aluminum alloy is known for its high strength, making it a popular choice for structural applications in various industries, including aerospace.

For the fabrication of test specimens, plates were welded perpendicular to the rolling direction using a vertical milling machine, specifically designed for FSW, as illustrated in **Figure 2** of **Article 3**. The plates were securely positioned within the fixture to ensure precise alignment during welding. The welding tool, with a shoulder diameter of 11.5 mm

and a conical threaded pin with a diameter of 5 mm and a length of 2.7 mm, was used to join the plates.

Defect generation was an integral part of this study to assess the sensitivity and capability of the employed ECT probes, particularly in detecting **wormhole** defect.

Wormholes were obtained by **tuning the welding process parameters** to obtain deliberately this kind of defect. Detailed parameters of the welding process, specifically the ω/v ratio, were defined to ensure the production of joints both with and without wormhole defects. Further elaboration on the selection of these parameters can be found in **Table 3** of **Article 1** and **Section 2.1** of **Article 3**.

4.2.2 Complementary NDT Methods and Mechanical Characterization

In this study, X-ray inspections were utilized as a complementary NDT method to verify the presence of wormhole defects in FDW joints and to assist in interpreting the ECT signals. Conducted in accordance with ISO 17636 standards, the X-ray inspections allowed for the precise identification of internal "tunnel"-type defects by revealing lighter shaded regions in the weld zone, indicative of material voids (see **Figure 5** and **Figure 6** of **Article 3**). This method provided a reliable reference for the comparative analysis of ECT results, ensuring accurate defect characterization. Detailed procedures and results of these inspections are provided in **Section 2.1** and **3.1** of **Article 3**, respectively.
Mechanical properties of the welded joints were assessed using an MTS QTEST 159 Universal Testing Machine under controlled environmental conditions (23 ± 2°C and 50 ± 10% RH). In addition to tensile tests, Vickers microhardness was measured with a Buehler 1600/3600 hardness testing machine to evaluate the hardness profile of the base material.

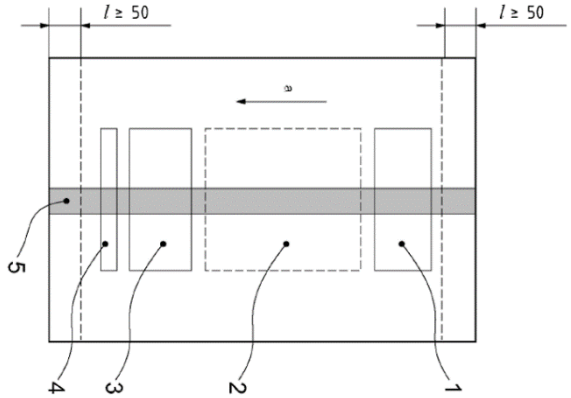

Figure 37 1) Designated zone for tensile, bend, or fracture specimen extraction; 2) Additional area for optional specimens; 3) Secondary zone for tensile, bend, or fracture specimen extraction; 4) Area allocated for macroscopic examination; 5) Weld seam; l: Discarded length at both ends of the weld to eliminate non-representative regions influenced by tool entry and exit [241].

Specimens for these tests were extracted according to the guidelines in UNE-EN ISO 25239-4 [241], ensuring representative results. Only the central section of the weld was used for specimen extraction, excluding the tool entry and exit regions, as these zones exhibit transient phenomena not reflective of the standard welding conditions (**Figure 37**). This rigorous methodology ensured accurate mechanical characterization and minimized the potential for erroneous conclusions.

4.2.3 ECT System Configuration for Electrical Conductivity and Defect Detection

Electrical conductivity measurements were performed using the absolute cylindrical helicoidally probe defined in **Table 7**, with signal generation and acquisition handled via the DEFdiscover® platform (ISEND S.A.). The electrical impedance of the probe, influenced by conductivity, lift-off, and frequency, was used to calculate the material conductivity. Given that the magnetic permeability in non-ferromagnetic materials like aluminium is constant, changes in impedance are directly correlated with variations in electrical conductivity. Calibration was carried out using AA6082-T6 standard reference materials with known conductivity values.

The selected frequency of 5 MHz ensured a penetration depth of 1.5 mm, optimizing the balance between surface and subsurface sensitivity. Inspections were performed along both the upper and lower surfaces of the weld seam (see **Figure 4 of Article 3**), ensuring that consistent probe orientation and lift-off were maintained. The process included inspections **along the weld** to simulate a real-time scenario for defect detection, particularly for artificial LOP on the opposite side of the weld.

Upper surface measurements aimed to map conductivity variations related to **microstructural changes** in the weld zone, focusing on correlating these values with microhardness measurements. On the **lower surface**, the selected frequency focused the eddy currents on subsurface regions, increasing **sensitivity for detecting defects** such as wormholes. Both inspections were conducted with a spacing of 30 mm between lines, excluding the outermost 40 mm of the weld, where transient phenomena could affect the accuracy of the measurements (**Figure 4 of Article 3**).

4.3 CASE II: Experimental Hardware

The experimental setup employed in this case study was specifically designed to evaluate the sensitivity of the developed EM sensors to damage-induced changes in the electrical properties of thermoplastic welded joints. The primary goal was to assess the sensors' ability not only to detect the presence or absence of defects but also to demonstrate a measurable response to variations in defect size and location. This comprehensive assessment aimed to validate the sensor performance in scenarios that closely resemble real-world applications. The following section outlines the materials and joints tested, the characterization methods applied, and the configuration of the hardware used to ensure accurate measurement of conductivity changes and defect detection in thermoplastic welded joints.

4.3.1 Material Selection and Test Specimen Fabrication

The materials used for fabricating the welded samples in this study comprised 2.5 mm thick CFRP laminates, featuring a Polyphenylene Sulfide (PPS) polymer matrix and 5-harness satin weave carbon fiber, provided by Toray Industries, Inc. Specimens with dimensions of 100 mm by 40 mm were prepared for the welding and testing procedures.

For the welded specimens, a commercial induction welding machine (Bielec S.L.) was utilized, with energy transferred via a solenoid inductor and temperature monitored using an infrared pyrometer (see **Figure 38 (a)**).

Step 1: Controlled Environment Evaluation of Sensor Capability

The first phase involved evaluating the EM sensor ability to detect defects and track changes in size and location in a controlled setting. A pristine CFRP laminate, alongside a defective version, was fabricated using a [(90º/0º/45º2/90º2/-45º2/0º/90º)]s lay-up of twenty unidirectional CF/PPS plies. The pristine laminate served as a reference for the sensor response, while the defective laminate, featuring embedded PTFE adhesive tapes (Tooltec® A005), was used to introduce controlled variations in the electromagnetic properties. The PTFE tapes, with varying sizes (15x15, 10x10, 8x8, 5x5, 2x2 mm) and positions within the laminate, simulated localized damage, allowing for a comprehensive assessment of the sensor sensitivity to defects (see **Figure 7** of **Article 2**).

Step 2: Realistic Application Testing

Subsequently, to evaluate the sensitivity of EM sensor to damage in a configuration closer to the final application, pristine and defective CF/PPS lap joints were manufactured. In order to reproduce the presence of a lack of weld, Glass fibres reinforced Polytetrafluoroethylene (PTFE) adhesive tapes (Tooltec® A005 supplied by AIRTECH Europe SARL) of 8x8 mm dimensions was collocated in the bond line before welding operations (**Figure 38 (b)**.).

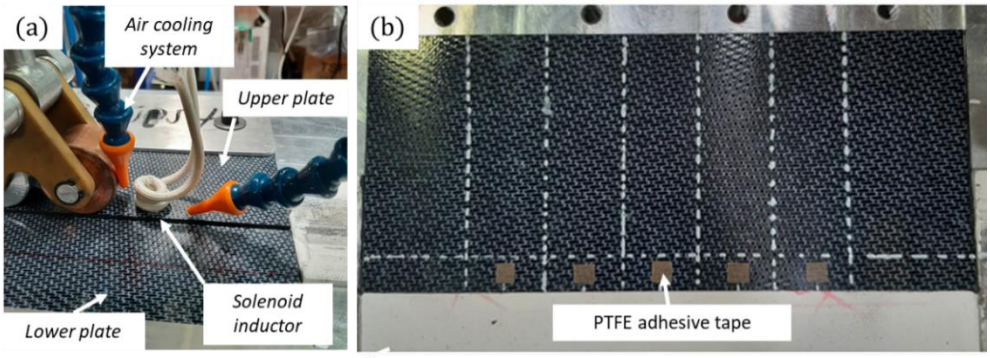

Figure 38 (a) Relevant components of Induction welding system. (b) PTFE adhesive tapes placed in the joint line for obtaining defective welds in a fully controlled way.

Three kind of welded lap-joints were manufactured as reported in **Table 8**: two different set of process parameters (set-up 1 and set-up 2) were selected to assess damage sensing techniques for two different mechanical joint properties; a third configuration was fabricated using the same welding process parameter of set-up 1 and employing the artificial defect placed in the joint line for obtaining defective welds in a fully controlled way (set-up 1-DEF).

Table 8 Induction welding process parameter employed for each manufacturing case.

Manufacturing cases	Travel speed [m/min]	Excitation coil voltage [V]	Frequency [kHz]	Distance coil-plate [mm]
Set-up 1	1.2	130	183	5
Set-up 2	1.6	147	183	5
Set-up 1-DEF	1.2	130	183	5

4.3.2 Mechanical Testing and Sensor Performance Evaluation

Five specimens were extracted from each welded sample for static and fatigue tests. **Figure 39** shows the useful section of the weld samples where specimens were extracted. In fact, the induced currents are distorted in these areas (edge effect) and consequently the resulting heat distribution is different from that one associated to the real process parameters.

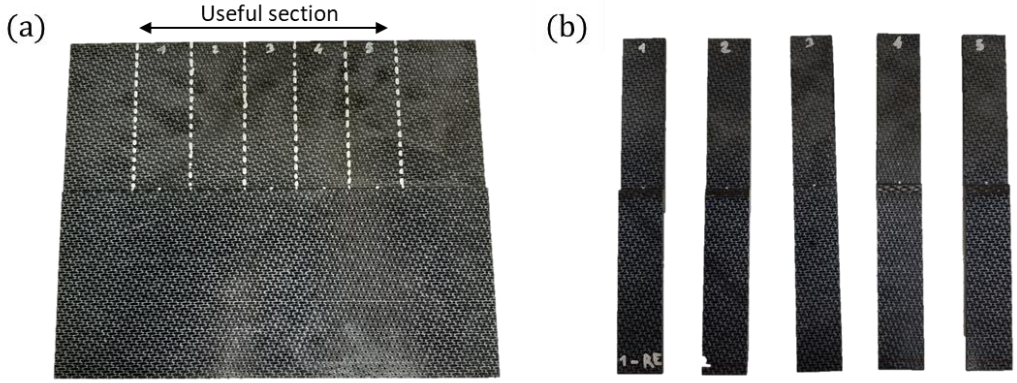

Figure 39 (a) Useful section of the weld samples where (b) specimens for quasi-static and fatigue tests were extracted.

Specimens per each case were tested according to ASTM D1002 in a MTS QTEST 159 Universal Testing Machine. Tabs were applied to the samples in order to ensure a load path parallel to the overlap line.

Sinusoidal tension–tension fatigue tests were carried out with load ratio R of 0.1 and a frequency of 2 Hz taking the ASTM D 1002 standard as a reference in a MTS 100 kN fatigue test bench. The fatigue test plan was defined with the aim of evaluating the ability of the investigated SHM approaches in detecting incipient and propagating damage rather than studying the dynamic properties of the obtained welds.

Set-up 1 and set-up 2 specimens were tested at a load level equivalent to the 70% of the lap-shear strength (LSS). Different life cycles were expected from these two cases and the employed sensing techniques were evaluated at different propagating scenarios. Welded specimen having embedded defects in the bondline (set up 1 – DEF) were tested at the same load level of set up 1 and an early break was expected due to artificially generated lack of welding in the bondline. With the aim of optimizing test times, a limit of around 36,000 cycles was established at the end of which, if the specimen had not broken, then the load level would have been increased to 80% of the LSS in order to speed up the achievement of the failure condition.

4.3.3 Damage Detection set-up

The developed EM sensors were strategically positioned on the specimens, as depicted in **Figure 40** to evaluate the changes in electrical properties due to the presence of defects. Signals were collected from both defective and pristine CFRP laminates, as well as from thermoplastic welded joints before and after the machining operations. Initially, the EM sensor was placed on the weld overlap zone, with measurements taken pre- and post-machining, to determine how sensor sensitivity to damage is influenced by the reduction in specimen width caused by the machining process

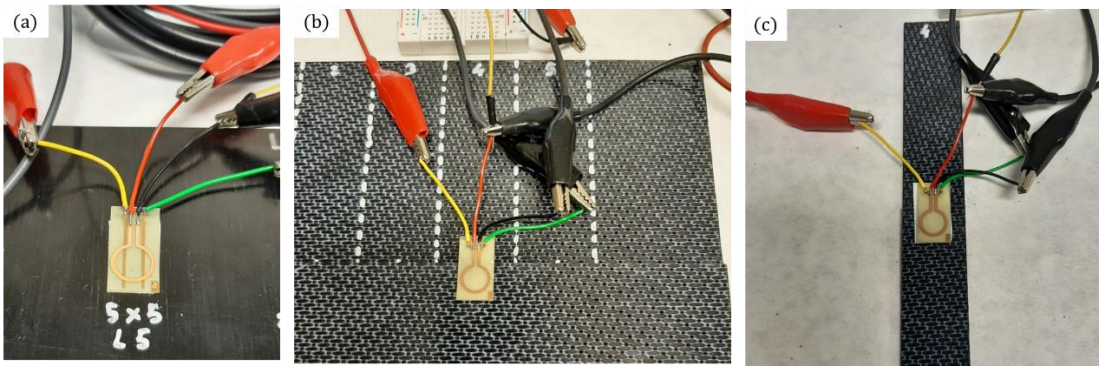

Figure 40 EM sensor placement on (a) defective CFRP laminate with embedded artificial defects and placement on thermoplastic welded joint (b) before and (c) after machining operation.

The frequency sweep, conducted using the built-in frequency response analyzer of the Moku Pro platform, generated a sinusoidal signal ranging from 0.1 to 10 MHz with an output voltage of 10 Vppk. This signal was applied to the emission loop of both sensors through coaxial cables, while the sensing elements' signals were collected by the Moku Pro inputs and displayed at each frequency point. For the PM sensor, the reception loop terminals were directly connected to the instrument, whereas, in the case of H sensors, coaxial cables were used to connect each sensing electrode.

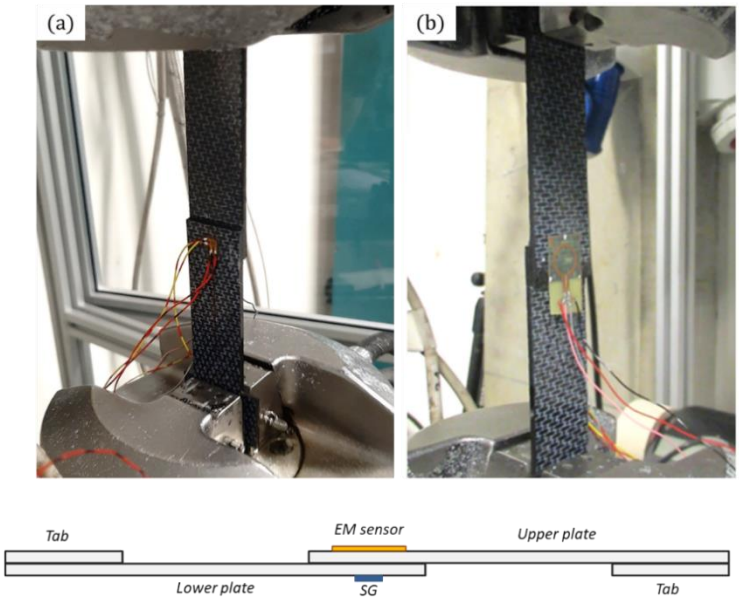

Figure 41 (a) SG and (b) EM sensor position on specimens during static and fatigue tests.

The setup enabled precise measurement of the potential difference between the electrodes. To ensure consistency and reliability, each frequency sweep was repeated 10 times, and no significant signal variation (below 2%) was observed, validating the accuracy of the data.

Additionally, PM sensor performance was assessed during static and fatigue tests. For comparative purposes, Strain Gauges (SGs) were installed as a complementary sensing technique. SGs were affixed to the backface of one of the adherents, centered in the overlap area, while the PM sensor was placed on the opposite face, with its emission and reflection loops aligned with the overlap zone (**Figure 41**).

For these tests, a sinusoidal signal ranging from 0.1 to 10 MHz, with an output voltage of 3.5 Vrms, was generated using the frequency response analyzer module of the Moku Pro platform. Insights from static and fatigue tests highlighted limitations in the PM sensor design, which informed the necessary adjustments to develop the more refined H sensor.

4.4 Summary of Chapter 4

Chapter 4 outlines the experimental methods and materials employed in the study, focusing on the design, fabrication, and testing of ECT probes for real-time monitoring and EM sensors for SHM. The chapter begins by establishing the methodological framework, detailing the specific inputs, requirements, and numerical simulations used to guide the sensor development for both applications.

Section 4.1 addresses the methodology, including the technical requirements for the ECT and EM sensors and the numerical methods used to optimize their designs. The process involved selecting key parameters such as coil configurations, frequency ranges, and sensitivity factors, with the goal of maximizing defect detection and minimizing noise in the resulting measurements.

In *CASE I*, described in *Section 4.2*, the chapter covers the selection of materials and fabrication of test specimens, specifically for the development of an ECT probe to monitor the FSW process. This section includes a detailed account of the materials used, specimen preparation, complementary NDT methods, and mechanical characterization techniques. Additionally, the configuration of the ECT system for measuring electrical conductivity and detecting defects is explained, highlighting the probe sensitivity to microstructural changes in the welded aluminum plates.

CASE II, detailed in *Section 4.3*, shifts the focus to the experimental validation of the EM sensors designed for SHM of thermoplastic welded joints. It provides an in-depth description of the materials used, including the fabrication of CFRP laminates with embedded artificial defects, and the setup for static and fatigue tests to assess sensor performance. The section concludes with a discussion of the damage detection setup, where the sensors' ability to detect and track changes in electrical properties caused by defect size and location is tested.

Chapter 5

5 Results and Discussion

Chapter 5 presents the results and discussion from two key case studies focused on real-time process monitoring with ECT probes and the application of EM sensors for SHM in thermoplastic induction welded joints. CASE I outlines the development of the ECT probe, its defect detection sensitivity, and findings from X-ray and mechanical testing. Key correlations between electrical conductivity and defect presence are discussed. CASE II covers the development and evaluation of EM sensors, exploring the effects of CFRP configuration on damage detection. The chapter also includes mechanical testing results, the performance evaluation of PM and H sensors, and sensor modifications to improve sensitivity. The chapter concludes with a summary of findings from both case studies.

5.1 CASE I: ECT Probe for Real-Time Process Monitoring

5.1.1 ECT Probe Development

The development of the ECT probe was initially characterized by a sensitivity study conducted through numerical simulations to evaluate the influence of key design parameters on the probe defect detection capabilities. First, a validation simulation was performed to confirm the accuracy of the model and its assumptions. A well-documented case of surface crack detection, supported by extensive experimental data from reference [242], was selected for comparison.

Figure 42 illustrates the model employed, where the calculation domain was modeled using air conductivity (**Figure 42 (a)**) and an aluminum plate containing a crack (**Figure 42 (b)**). The crack itself was modeled by assigning air conductivity values, as outlined in Section 4.1.2. The mesh refinement around the crack, crucial for accuracy, is depicted in **Figure 42 (c)**.

The results, as shown in **Figure 43**, present the variations in inductance (ΔL) and resistance (ΔR) with respect to the ECT probe position relative to the defect, which are defined as:

$$\Delta R = R_{def} - R_{free} \tag{61}$$

$$\Delta L = L_{def} - L_{free} \tag{62}$$

where the sub-index indicates the values of resistance and inductance evaluated in the presence (*def*) or absence (*free*) of the defect. A strong correlation between the numerical data and experimental findings was observed, affirming the reliability of the numerical model employed.

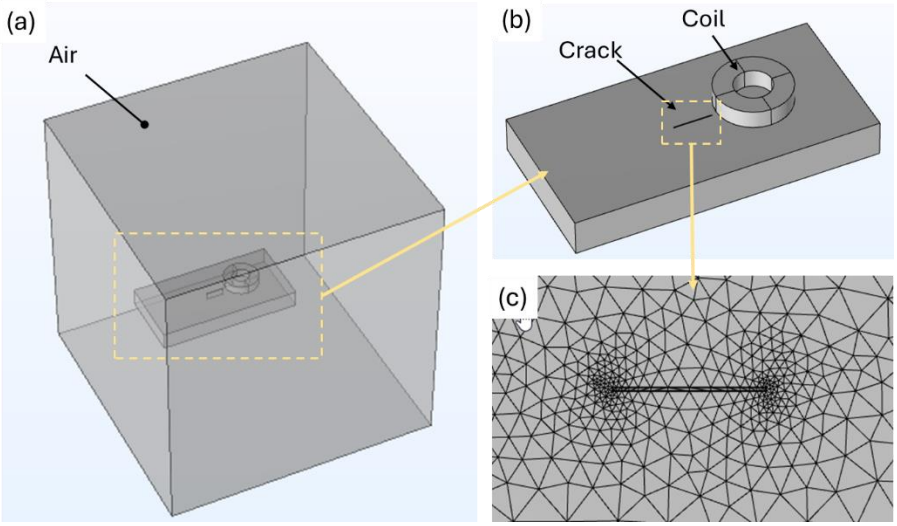

Figure 42 Numerical model used for surface crack detection in an aluminum plate (a) air domain, (b) aluminum plate with modeled crack, (c) mesh refinement near the crack.

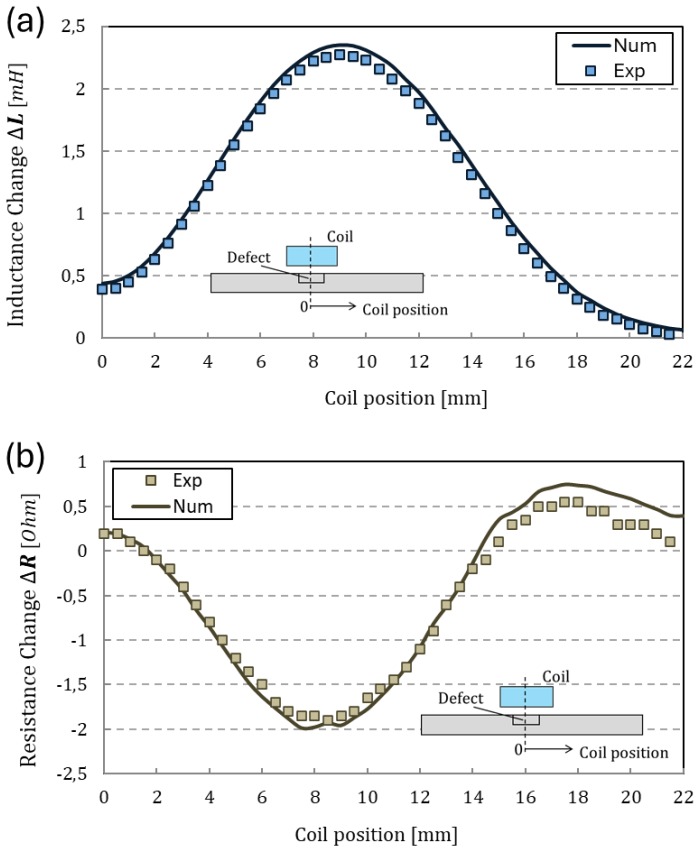

Figure 43 Variations in inductance and resistance as a function of ECT probe position relative to surface crack.

Following validation, a parametric study was conducted by varying key parameters such as the number of turns (N), the probe diameter (b), and the height (h). This allowed for the assessment of the impact of these variables on defect sensitivity, which is expressed as the variation in impedance by the following equation:

$$|\Delta Z| = \left|Z_{def} - Z_{free}\right| \tag{63}$$

$$\text{where} \qquad Z = \frac{V}{I} = R + j2\pi fL \tag{64}$$

Impedance, being directly measurable in practice, serves as a crucial metric for evaluating defect sensitivity. As discussed in Section 4.1.2, the evaluated scenario involves a defect positioned on the surface opposite to the inspection side (see **Figure 33**), simulating conditions similar to real-time inspection where only the upper surface is accessible. In such cases, defects like wormholes may be present on the lower surface, necessitating a probe capable of detecting through the full thickness.

Figure 44 (a) shows the impedance variation for different values of b/h and varying numbers of turns. It is evident that as the number of turns increases for a constant b/h, the probe sensitivity to the defect also increases. This outcome aligns with established understanding, as increasing the number of turns enhances the electromagnetic response, thereby improving defect detectability. With respect to slenderness (b/h), probes with a lower slenderness exhibited greater sensitivity, indicating that winding the turns closer to the inspection surface and maximizing the probe diameter enhances performance. This can be attributed to a higher concentration of the magnetic field (and consequently higher eddy currents concentration) near the inspection area, thus improving sensitivity. In designing the optimal probe, the objective was to maximize the number of turns while keeping the coil diameter large (**Figure 44 (b)**) and the height low.

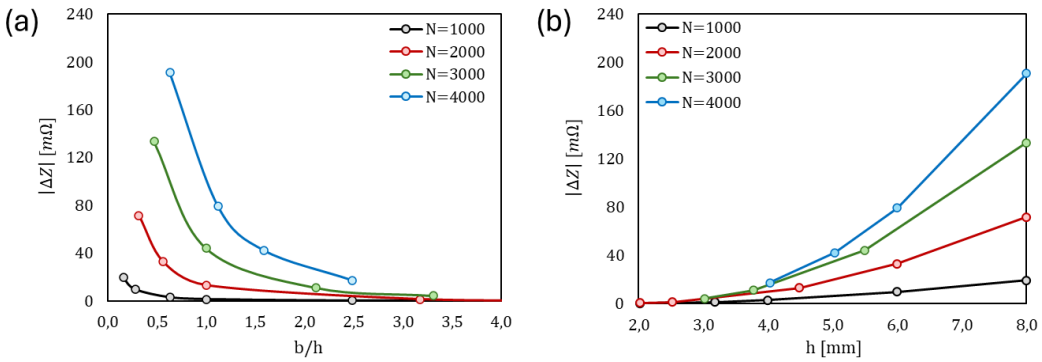

Figure 44 Defect induced impedance variation for different values of numbers of turns, (a) slenderness ratio and (b) design parameter h.

However, the coil diameter was limited to 10 mm, matching the FSW weld width used in this study, to ensure the probe focus remained on the weld region and reduced potential interference from the adjacent base material. As illustrated in **Figure 45**, configurations with a coil parameter h greater than 4 mm were excluded from consideration. Starting from this height, the design focused on maximizing the number of turns while minimizing the coil height to avoid compromising performance. It is crucial to note that achieving the theoretical fill factor of 0.78 in practice is challenging due to manufacturing tolerances. Factors such as variations in wire cross-section geometry, insulating coating thickness, and winding strategies all contribute to reducing the achievable fill factor. Although the design aimed for 4000 turns, only 1230 turns were wound, yielding a fill factor of 0.24 and a coil height of 10 mm, as shown in **Figure 45**. These trade-off parameters were carefully considered in the final probe design.

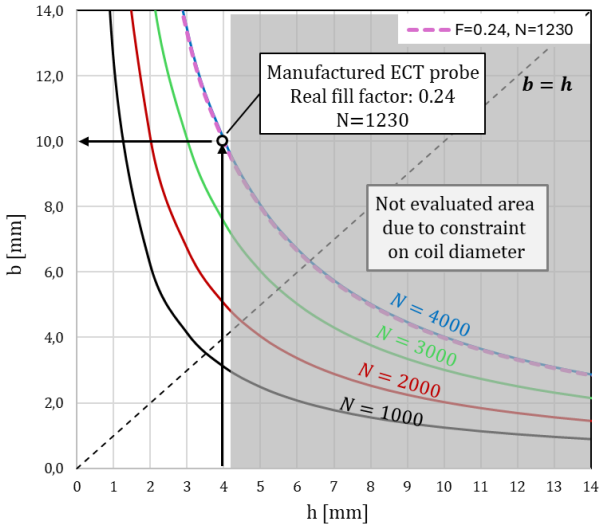

Figure 45 Design constraints and trade-off parameters for ECT probe sizing, with coil parameters *b* and *h* considered for the chosen configuration.

Figure 46 demonstrates the probe simulated defect sensitivity across various excitation frequencies. Two sensitivity peaks were observed: one at approximately 2 kHz, where the penetration depth aligns with the defect location, and another at 6 kHz, despite a smaller penetration depth.

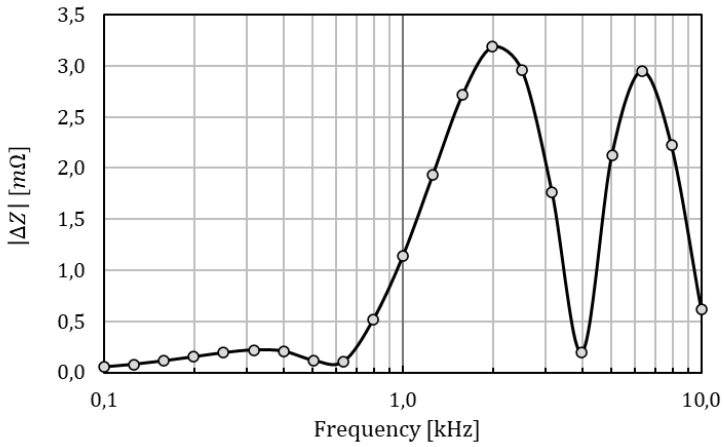

Figure 46 Simulated defect sensitivity for the manufactured ECT probe as a function of excitation frequency.

This second peak suggests that even with reduced penetration depth, the altered distribution of eddy currents at higher frequencies enhances interaction with the defect. These interactions produce notable variations in the magnetic field, suggesting that at different frequencies, current trajectories may either amplify or diminish the sensor ability to detect defects. Indeed, defect sensitivity is influenced not just by penetration depth but also by how the altered current paths interact with the defect, potentially enhancing or limiting detection. While these findings offer valuable insights into optimal frequency ranges, they are indicative since real-world defects may differ in size and geometry from those simulated. Nevertheless, this result provides essential guidance for the selection of the optimum ECT probe excitation frequency.

5.1.2 Defect Detection Sensitivity

The detection capability of the developed ECT probe for wormhole defects was thoroughly assessed, in particular using welded sample w1, which exhibited both defect-free regions and regions containing wormholes, as confirmed by radiographic inspection (see **Figure 6 of Article 3**). **Figure 47** reports the electrical conductivity measurements along the weld seam, taken on both the upper and lower sides of the joint at different frequencies (5 and 20 kHz). On the lower side, the probe demonstrated sufficient sensitivity to detect the presence of the wormhole, where the conductivity values decrease progressively as the defect size increases. Conversely, inspections on the upper side did not show any detectable variations in conductivity, indicating that the probe was unable to capture the defect in this orientation. However, the consistent conductivity values observed on the upper surface suggest the absence of any microstructural changes along the weld seam, confirming that the gradual reduction in conductivity on the lower surface is exclusively associated with the presence of the wormhole defect. This supports the conclusion that the probe primary defect detection capability is limited to the lower surface, while the upper surface is more suited for assessing microstructural properties, such as grain size and precipitate distribution. Fine-tuning parameters such as frequency, coil geometry, and lift-off distance may improve the resolution and effectiveness of ECT for detecting subtle conductivity variations associated with defects, performing the inspection from the upper side.

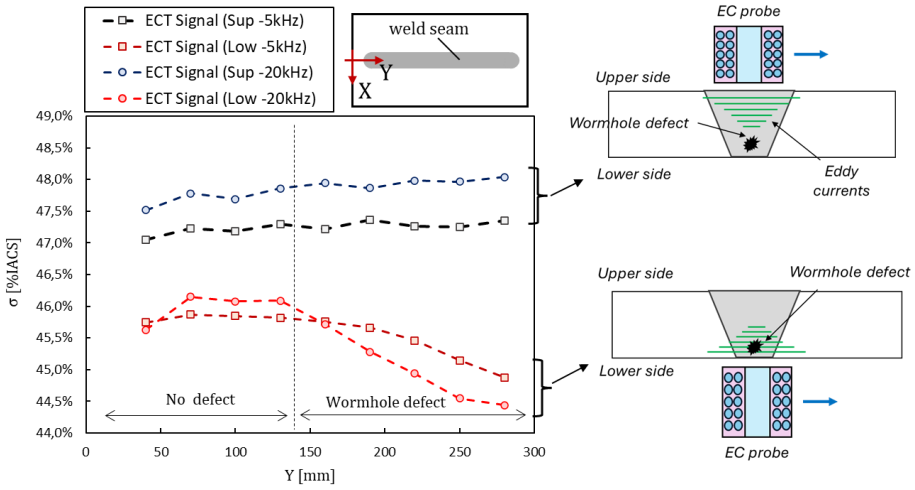

Figure 47 Variation of electrical conductivity in the SZ along the weld seam (X = 0) evaluated in both the upper and lower face of the w1 FSW welded joint and using an excitation frequency of 5 kHz and 20 kHz.

Figure 48 presents a comparative analysis of electrical conductivity in various defective and non-defective specimens (various ω/v ratio), revealing a notable trend: in samples with wormholes, conductivity values on the upper surface are consistently lower than those on the lower surface. Conversely, in defect-free specimens, this relationship is reversed. If we limit the analysis to scenarios where only the lower side of the weld is accessible during real-time FSW inspection, the data indicates that conductivity measurements on the lower surface alone fail to provide a clear distinction between defective and defect-free regions, with values fluctuating between 45.6% to 47.9% IACS for 5 kHz excitation and 45.0% to 48.5% IACS for 20 kHz. While the results suggest that inspecting the upper surface could offer an indirect indication of defect presence—given the differing conductivity levels between defective (average 48.3% IACS) and non-

defective (average 45.0% IACS) specimens—this is not universally reliable, as shown by a broader set of cases (refer to Figure 13 in Article 3).

However, the inverse relationship observed between upper and lower surface conductivity in all cases so far could serve as a promising indicator of defect presence. This consistent trend across various specimens suggests that future implementations of ECT for real-time monitoring may benefit from dual-surface inspection, as accessing both sides of the weld could significantly enhance the accuracy and reliability of defect detection.

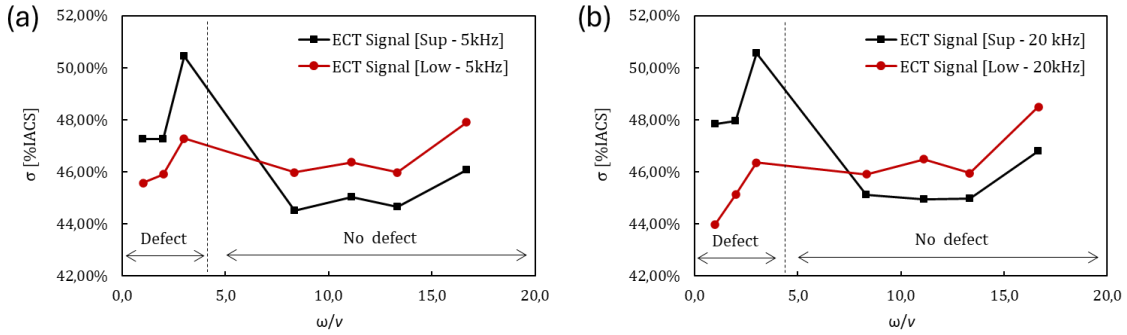

Figure 48 Variation of electrical conductivity in SZ with changing ω/ν ratio on upper and lower faces at (a) 5 kHz and (b) 20 kHz.

5.1.3 X-ray and Mechanical Testing Results

X-ray Inspection Results: Validation of Defect Location

The X-ray inspection revealed the presence of wormhole defects in six out of twelve manufactured samples, as summarized in **Table 4** of **Article 3**. These defects are attributed to inadequate material flow, caused by insufficient heat generation during the welding process. The inadequate thermal input typically stems from a low rotational speed (ω) combined with a high travel speed (v), resulting in insufficient contact time between the tool and the workpiece. Consequently, the material does not soften and mix effectively, leading to improper plastic deformation. Notably, wormhole defects were observed at the lowest ω/v ratio values. A transition zone exists at an approximate ω/v ratio of 4, where welds shift from defective to defect-free. This transition is governed by critical ω and v values, which directly influence the heat input during the process.

Figures 5(a) and **Figure 5(b)** of **Article 3** present typical X-ray radiographs for defect-free and wormhole-containing welded joints, respectively. The wormhole was consistently located approximately 0.5 mm from the lower surface, as shown in **Figure 5(d)** of **Article 3**. This positioning can be explained by limited material flow in the lower weld region, aligning with flow patterns observed in previous studies on FSW.

For additional details on the X-ray inspection results, see **Section 3.1** of **Article 3**.

Mechanical Testing: Tensile Strength and Microhardness

Tensile testing of the FSW specimens revealed a reduction in tensile strength compared to the base material, with joint efficiencies ranging from 62% to 70% for defect-free joints, and between 53% and 62% for joints containing defects (as shown in **Table 5** of **Article 3**). The reduction in mechanical properties is linked to the thermal

exposure inherent to the FSW process, which reaches temperatures between 400°C and 550°C in SZ due to friction and plastic deformation. This elevated temperature causes dissolution and coarsening of the second-phase precipitates responsible for the strengthening in heat-treatable aluminum alloys like AA6082-T6, thereby weakening the joint overall integrity.

Hardness measurements within the weld nugget reflect this decline in tensile properties, with reductions observed due to the disruption of the material artificial ageing treatment (T6) applied at approximately 180°C. For welded samples exhibiting wormhole defects (samples w1 to w6 in **Table 5** of **Article 3**), tensile properties were further degraded, with notable decreases in ultimate tensile strength (UTS) and significant reductions in elongation. The brittle behavior of defective samples was evidenced by the sharp decline in the stress-strain curves, with stress concentration points created by the wormhole defect likely contributing to premature failure during tensile testing.

This behavior aligns with previous studies, which have demonstrated that welding defects such as wormholes can act as sites for stress concentration, leading to crack initiation and propagation under tensile loads, thus compromising the overall structural stability of the weld.

Additional details on the mechanical testing results and the relationship between UTS and microhardness values as a function of heat input are provided in **Section 3.2** of **Article 3**.

5.1.4 Discussion of Correlations Between Electrical Conductivity, Mechanical Properties, and Defect Presence

The analysis of the electrical conductivity field using eddy currents for each joint was compared with microhardness, x-ray inspection, and tensile testing results, revealing significant correlations. Across all samples, substantial variations in electrical conductivity were detected due to the effects of FSW. These conductivity changes reflect microstructural alterations within different zones of the weld, showing a reciprocal trend with microhardness values as the ω/v ratio varies.

It was notably observed that as the heat input increases, indicated by a higher ω/v ratio, the weld seam cross-sectional area expands, accompanied by corresponding variations in electrical conductivity. Specifically, the width of the weld seam increases from approximately 15 mm to 25 mm as the heat input rises. Furthermore, welds that exhibit wormholes, or those near the transition zone between defective and non-defective regions, demonstrate a distinctive bell-shaped or V-shaped electrical conductivity distribution (**Figure 15** of **Article 3**). This pattern contrasts with defect-free joints, which typically display a W-shaped distribution (**Figure 17** of **Article 3**). where the peak conductivity values align with the regions prone to failure. This characteristic conductivity pattern could serve as an indicator for identifying defects.

Regarding the correlation between electrical conductivity and mechanical properties, **Figure 18** in **Article 3** presents the relationships between microhardness, ultimate tensile strength (UTS), and electrical conductivity. An inverse correlation was found between microhardness and conductivity, as well as between UTS and conductivity. These correlations highlight the potential for integrating electrical conductivity measurements into a process monitoring framework, allowing for real-time weld prognosis. Detecting process deviations driven by microstructural changes can enable timely corrective actions to ensure consistent weld quality.

Overall, these findings emphasize the value of using electrical conductivity as a non-destructive predictor of mechanical properties such as microhardness and UTS, which can facilitate real-time assessment of joint integrity.

Additional details on correlation analysis are provided in **Section 3.3** of **Article 3**.

5.2 CASE II: EM Sensors for SHM Applications

5.2.1 PM Sensor Development

As detailed in section 4.1.4, the excitation element was selected as a single-loop antenna, with the magnetic field measured by a sensing loop. Two configurations were analyzed: the reflection method (with both loops on the same side) and the attenuation method (with loops on opposite sides) as depicted in **Figure 36**.

The numerical analysis considered sinusoidal magnetic field excitation and evaluated the induced voltage in the reception loop for three cases:

(a) susceptorless joints,
(b) joints with a susceptor in the bond line, and
(c) joints with delamination in the joint layer.

This allowed for a comprehensive understanding of the magnetic field distribution and the sensitivity of the PM sensor to variations in conductivity, particularly those associated with defects.

For non-perfectly conductive CFRP joints, it was crucial to identify **the cut-off frequency** starting from the sensor sensitivity to defects grows abruptly. For both configurations, the optimal frequency for defect detection was found to be **between 2 and 3 MHz.** However, the attenuation response showed greater sensitivity to delamination than the reflection method, especially for smaller defects as shown in **Figure 7** of **Article 1**.

The **introduction of a susceptor** in the bond line notably reduced the sensor sensitivity to defects. **Figure 10** of **Article 1** illustrates that the presence of the susceptor, with an assumed conductivity of 400 kS/m, shifted the optimal sensitivity frequency and decreased the overall detection capability. This reduction in sensitivity was **more pronounced** in the **attenuation response** due to the susceptor influence on the electromagnetic field.

Additionally, the **loop radius** was found to have a significant impact on damage sensitivity. As shown in **Figure 8** of **Article 1**, smaller loops increased sensitivity to smaller defects. Nevertheless, a tradeoff was necessary to balance sensitivity with the need to cover the entire overlap area of the joint. Based on the analysis, a **loop radius of 10 mm** was selected for the final PM sensor configuration.

The **PM sensor reflection method** was ultimately chosen over the attenuation approach due to practical considerations. The attenuation method, while more sensitive, required access to both sides of the joint, a significant limitation in aerospace applications where surface-mounted sensors could interfere with aerodynamic performance. This critical challenge led to the exclusion of the attenuation method in favor of the reflection approach, which requires access to only one side of the joint. Additionally, the reflection

method proved unaffected by the presence of a susceptor, further supporting its selection for subsequent analyses.

5.2.2 Numerical Model Validation

The results of the previous numerical analysis highlighted that the modeling approach for CFRP has a significant impact on the agreement between numerical and experimental data (see "***Experimental***" section of **Article 1**). Once the final PM sensor configuration was established, featuring a 10 mm radius and reflection mode, it was necessary to eliminate the simplifications used in the earlier simulations (such as the axisymmetric model and the neglect of connection cables, as described in the "***Numerical Methods***" section of **Article 1**). A more detailed model was then developed, including a refined representation of the sensor geometry and a more accurate modeling of the anisotropy of the CFRP material.

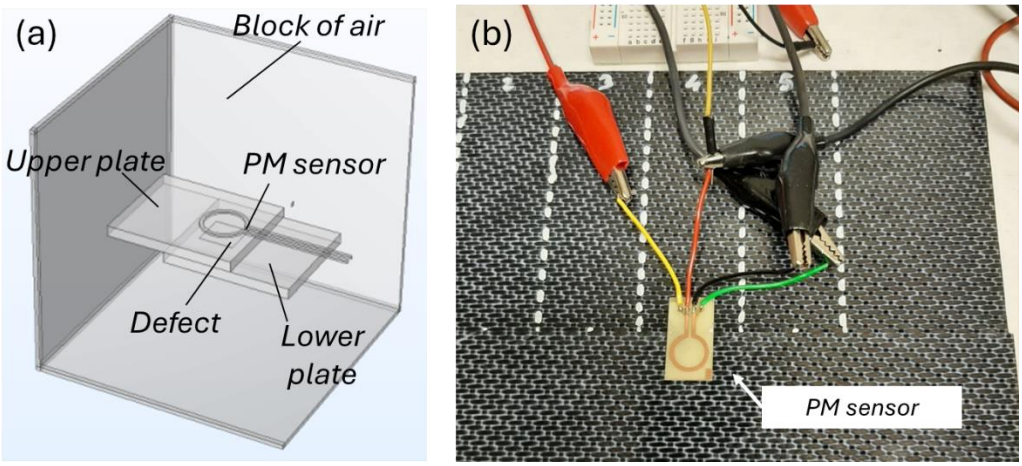

Figure 49 Numerical model employed to simulate the frequency response of PM sensor. (b) Experimental set-up for damage detection evaluation.

The AC/DC module in COMSOL® Multiphysics was employed to simulate the frequency response of PM sensors positioned over the joint overlap area (**Figure 49 (a)**). To simulate the presence of defects, such as a reduction in joint surface area, a 0.1 mm thick and 8x8 mm artificial defect was modeled in the bond line, assuming air conductivity for this region (**Figure 49 (a)**). The CFRP material was modeled with an orthotropic conductivity tensor, where σ_l= 11300 S/m, σ_t= 11300 S/m, and σ_{cross}= 44 S/m, to accurately reflect the anisotropy of the woven carbon fiber structure.

To validate the accuracy of this model, test specimens were fabricated using 5HS woven fabric CFRP laminates, and PM sensors were placed on the weld overlap zone to inspect the weld integrity. Voltage measurements were taken from the reception loop across a frequency range of 0.1 to 5 MHz, as depicted in (**Figure 49 (b)**).

Figure 50 shows that the numerical models provided a strong correlation with the experimental data, confirming the validity of the approach. With the validated model, further analysis was conducted to examine the impact of CFRP configuration on damage detection sensitivity. Fiber direction, stacking sequence, and the type of carbon fiber fabric have a significantly influence the distribution of eddy currents, and consequently, the effectiveness of the sensor in detecting damage.

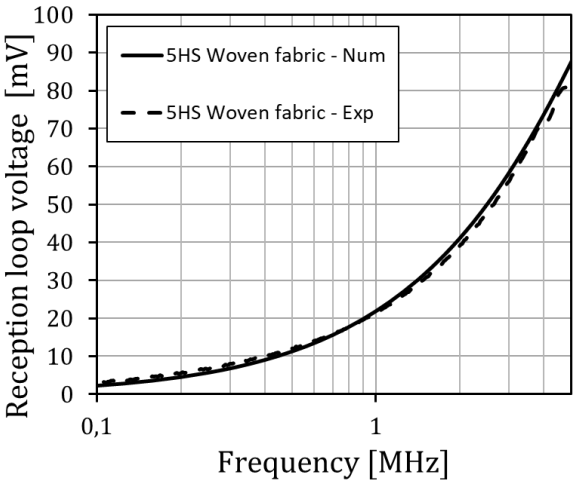

Figure 50 Numerical vs Experimental data.

5.2.3 Influence of CFRP Configuration on Damage Sensitivity

Building on the model presented in the previous section, further analysis was performed to evaluate the impact of different CFRP configurations on the sensitivity of damage detection. Three types of CF/PAEK lap joints were examined, varying the laminate configurations of the adherents:

(*i*) a stacking sequence of $[(0,30,60,90)]_{symm}$,
(*ii*) a stacking sequence of $[(0,45,70,90)]_{symm}$, and
(*iii*) 5HS woven fabric-reinforced laminates.

In each configuration, the CF/PAEK plates were assumed to have a uniform thickness of 2.48 mm. To accurately simulate the physical behavior of each joint type, the electrical properties of the CFRP laminates were appropriately defined, ensuring that the anisotropic nature of the materials was taken into account.

Table *9* summarizes the primary properties used in the FEM simulations, which allowed for a detailed examination of the effects that different fiber orientations and laminate types have on eddy current distribution and, consequently, on damage detection sensitivity.

In SHM applications, detecting damage is typically achieved by observing changes in a reference signal corresponding to the undamaged structure. *Damage sensitivity* is evaluated by comparing the induced voltage in the reception coil in the presence and absence of defects, as described by the following parameter (ΔV):

$$\Delta V = 20log_{10}\left[\frac{V_{defect}}{V_{sound}}\right] \quad (65)$$

where V_{defect} and V_{sound} are, respectively, the induced voltage ofthe reception coil in the presence and absence of a defect.

Figure 51 illustrates the damage sensitivity of PM sensor, revealing how frequency response varies with different CF thermoplastic composite joints. Notably, for joints

made with 5HS woven fabric laminates, a peak in maximum sensitivity is observed around 2 MHz.

Table 9 Electrical properties used in FEM simulations (data estimated from [243]–[245])

Material properties	**Laminates configuration**		
	$[(0,30,60,90)]_{symm}$	**$[(0,45,70,90)]_{symm}$**	**5HS woven fabric**
Electrical conductivity [S/m]	σ_l =11300, $\sigma_t = 105$, $\sigma_{cross} = 44$	$\sigma_l = 11300$, $\sigma_t = 105$, $\sigma_{cross} = 44$	$\sigma_l = 11300$, $\sigma_t = 11300$, $\sigma_{cross} = 44$
Magnetic permeability	$\mu_r = 1$	$\mu_r = 1$	$\mu_r = 1$

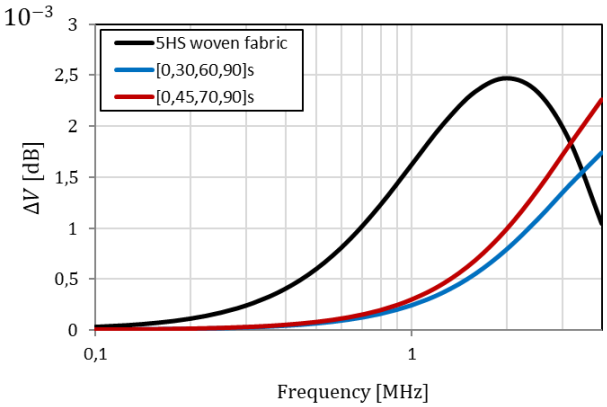

Figure 51 Damage sensitivity of EM sensor inspecting the three different welded CF thermoplastic composites.

In contrast, for thermoplastic welded joints using stacked laminates, the damage sensitivity increases progressively with frequency for both stacking sequences. At equal frequencies, PM sensor display a higher sensitivity for laminates with a [0,45,70,90]s stacking sequence compared to the [0,30,60,90]s sequence. However, across the considered frequency range, the highest sensitivity is consistently achieved when inspecting 5HS woven fabric laminates, indicating its superior performance in detecting damage.

The observed differences in damage sensitivity trends can be attributed to the varying anisotropy in the electrical conductivity of the adherents, which leads to distinct distributions of induced currents. These variations in current intensity and orientation relative to the defect produce different magnitudes of changes in the magnetic field measured by the PM sensor when transitioning from a sound to a defective joint.

Figure 52 illustrates the intensity and trajectories of the induced currents for the three cases, both in the presence and absence of a loss in the welded area. In the case of the 5HS woven fabric laminates, which exhibit homogeneous electrical conductivity within the plane, the induced currents tend to follow circular paths in sound structures (**Figure 52 (a)**). Conversely, for stacked laminates, the induced currents align parallel to the longitudinal direction of the carbon fiber (CF) orientation, which is characterized by higher conductivity values (**Figure 52 (b)** and **(c)**). This alignment results in different

current distributions and, consequently, distinct EM sensor responses in detecting damage across various laminate configurations.

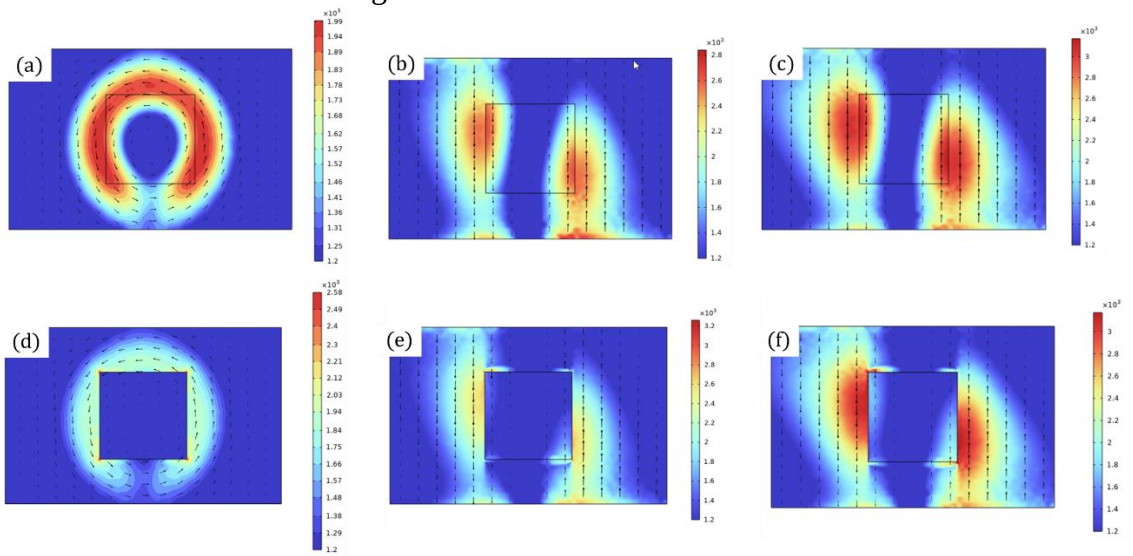

Figure 52 Intensity and distribution of current density on the welded interface for (a-c) sound and (d-f) defective joint when the CF thermoplastic materials of the adherents are (a, d) 5HS woven fabric laminates (at 1.99 MHz)., (b, e) unidirectional CF laminates with stacking sequence [0,30,60,90]s (at 3.98 MHz) and (c, f) [0,45,70, 90]s (at 3.98 MHz).

Examining **Figure 52 (d)**, the presence of a defect (modeled as an area with near-zero conductivity) significantly diminishes the current flow in the bondline, resulting in a maximum current density reduction of 0.59 x 10^3 A/m². In contrast, for stacked laminates, the defect is located in regions with lower current density, meaning its influence on the overall current distribution is minimal. The wider areas of high-intensity current in the [0,45,70,90]s stacking sequence compared to the [0,30,60,90]s configuration explain the superior damage sensitivity of PM sensor, as observed in **Figure 51**. This suggests that the stacking sequence of the laminates plays a crucial role in determining the sensor sensitivity to detecting defects.

5.2.4 Mechanical Testing and Fracture Analysis of Thermoplastic Induction Welded Joints

Figure 53 presents the results of the single-lap shear tests for the thermoplastic induction welded joints. Welds produced using Set-up 1 parameters exhibit an average ultimate load of approximately 2.8 kN. In contrast, the same process parameters applied to joints with artificially generated defects (Set-up 1-DEF) result in lower ultimate loads, around 2.1 kN, as expected due to the reduced weld area. Set-up 2 yields significantly higher static mechanical properties, achieving an average ultimate load of 5.8 kN. The high statistical dispersion observed in lap shear test results is attributed to the sensitivity of the induction welding process to factors such as material type, thickness, and overall substrate quality. This is due to the fact that electromagnetic waves must pass through the adherents to reach the weld interface, and variations in these conditions can significantly affect the induction process.

In Set-up 1, the lower power input (see **Table 8**) limits the movement of polymer chains across the weld interface, potentially leading to less effective bonding. The reduced heat generation restricts the ability of the polymer to flow and consolidate

properly, resulting in a weaker weld. In contrast, the higher power input in Set-up 2 provides sufficient energy to promote better polymer chain mobility, enhancing the interfacial bonding between the layers and leading to improved mechanical performance. This increase in power enables more thorough consolidation, which translates into better weld quality and higher ultimate loads observed in Set-up 2. The apparent lap shear strength (LSS), calculated as the ultimate load divided by the actual welded area (determined through optical microscopy), reveals comparable values for Set-up 1 (20.6 ± 10.7 MPa) and Set-up 1-DEF (21.3 ± 4.4 MPa), as both used the same processing parameters. However, Set-up 2 shows a significantly higher LSS (38.2 ± 10.8 MPa), corroborating the observed differences in ultimate load. It is important to interpret these LSS values cautiously, as intrinsic characteristics of the welds or potential substrate deformation can alter the stress distribution at the bondline [246].

Figure 53 displays the results of the single-lap shear tests. Induction welds manufactured by Set-up 1 processing parameters have an average ultimate load around 2.8 kN. Corresponding welds obtained with the same process parameters but having an artificially generated defect (Set-up 1-DEF) have lower static properties (around 2.1 kN) as expected due to the smaller welding area. Set-up 2 processing parameters give better static mechanical properties than Set-up 1 ones with an average ultimate load of 5.8 kN. It must be considered that for this welding technique, electromagnetic waves travel through the adherents to reach the welding interface and inductive phenomena are quite sensitive to the nature of the substrates such as type of material, thickness and quality. This aspect could explain why lap shear test results present a scatter so high.

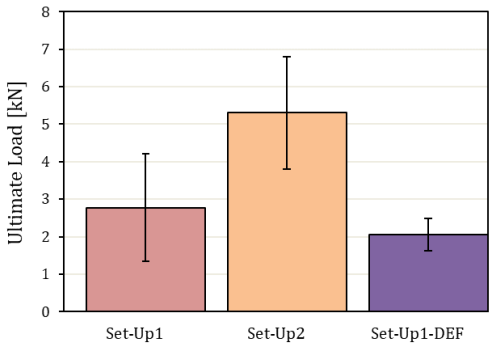

Figure 53 Quasi-static single-lap shear tests results.

Figure 54 presents the strain measurements recorded by SG during quasi-static tests. The results reveal a compressive stress state concentrated in the central overlap zone of the joint, corresponding to the SG position. Comparing Set-up 1 specimens with and without defects at the weld interface, both fail under the same imposed displacement. Nevertheless, the defective specimen exhibits higher stiffness, likely due to variations in the distribution of peel and shear stress concentration at the overlap edge. In the case of Set-up 2 specimens, higher surface deformation levels were observed, reflecting the increased stress state characterizing this setup.

Figure 55 presents representative fracture surfaces of specimens from Set-Up 1, Set-Up 2, and Set-Up 1-DEF batches.

The fracture surface analysis, depicted in **Figure 56**, indicates that all cases showed relatively resin-rich areas. However, Set-up 1 exhibited less impregnation between resin and fiber (**Figure 56 (a)**), resulting in interfacial failure, which supports the hypothesis of reduced polymer chain movement across the weld interface.

In contrast, Set-up 2 (**Figure 56 (b)**)predominantly displayed intralaminar failure and fiber tearing, indicative of better resin-fiber impregnation and superior weld consolidation. Interestingly, similar intralaminar failure and fiber tearing were observed in the welds containing artificial defects (intended to simulate an absence of weld - **Figure 56 (c)**). Despite utilizing the same parameters as Set-up 1, the presence of the PTFE adhesive tape appears to have influenced the thermal distribution during welding, potentially contributing to localized consolidation improvements.

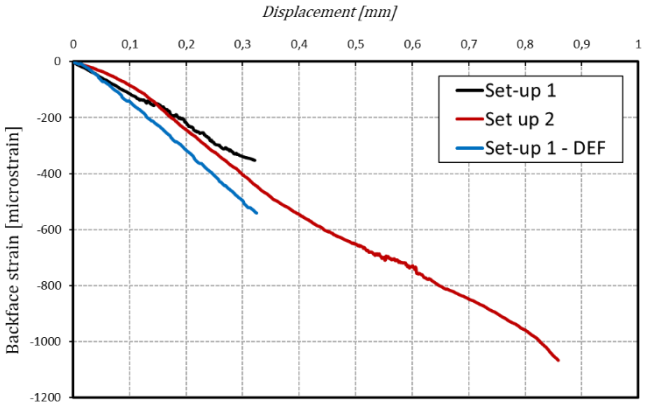

Figure 54 SG measurement during quasi-static tests.

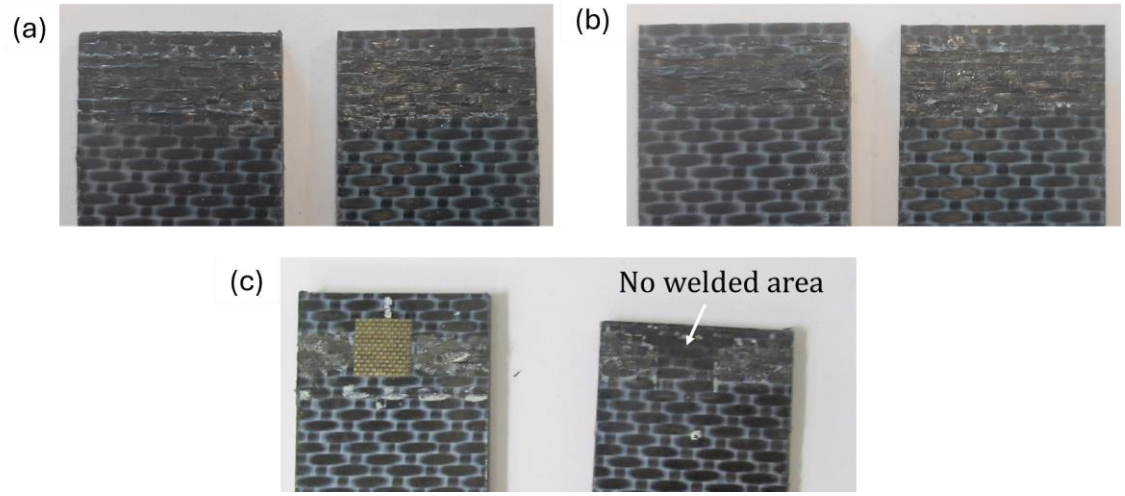

Figure 55 Fracture surfaces of representative specimens from (a) Set-Up 1, (b) Set-Up 2, and (c) Set-Up 1-DEF batches.

For each welding configuration, a specimen was selected and instrumented with both a SG and PM sensor, and subjected to cyclic fatigue loading. The primary aim of these tests was not to study the fatigue behavior of induction-welded joints per se, but rather to evaluate the performance of the PM sensor under fatigue conditions. **Table 10** presents the cycles to failure for each tested specimen, providing reference data for the analysis of damage sensing results discussed in Section 5.2.5.

As anticipated, Set-up 1-DEF, with its reduced welded area, exhibited fewer cycles to failure compared to Set-up 1 under the same applied load. Interestingly, the Set-up 2 specimen experienced premature failure, likely attributable to a significantly lower actual LSS compared to the average, which resulted in a more severe stress state within the bondline.

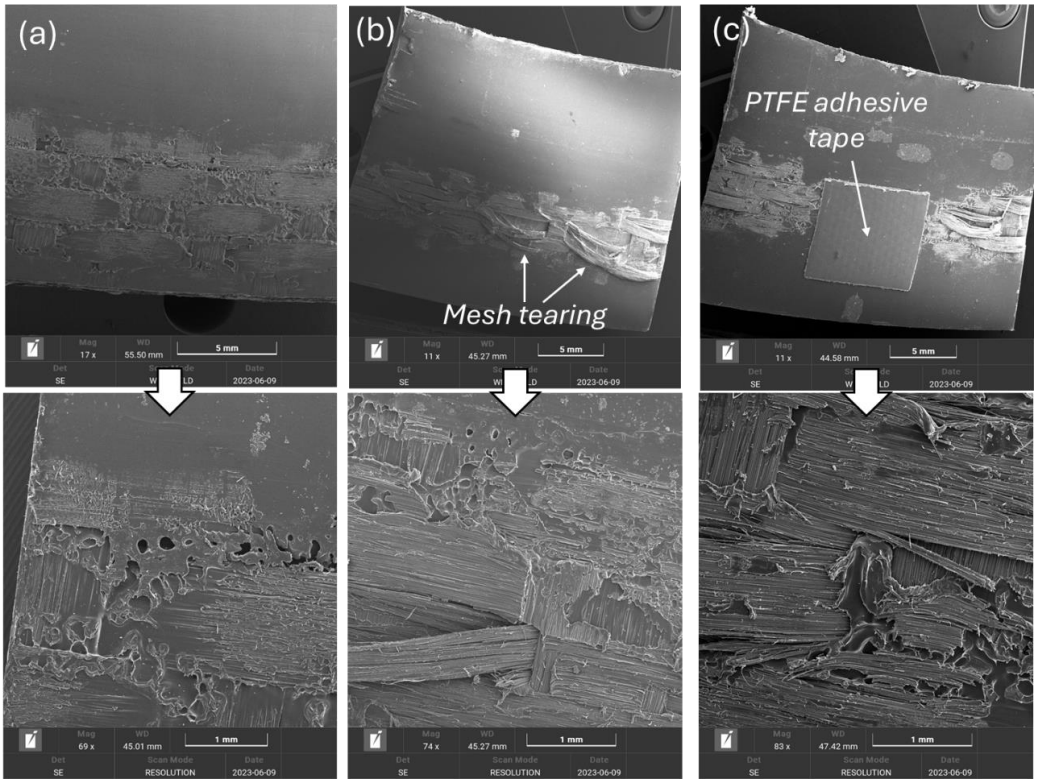

Figure 56 SEM micrographs of fracture surfaces for (a) Set-up 1, (b) Set-up 2, and (c) Set-up 1-DEF thermoplastic induction welded joints after quasi-static single-lap shear tests.

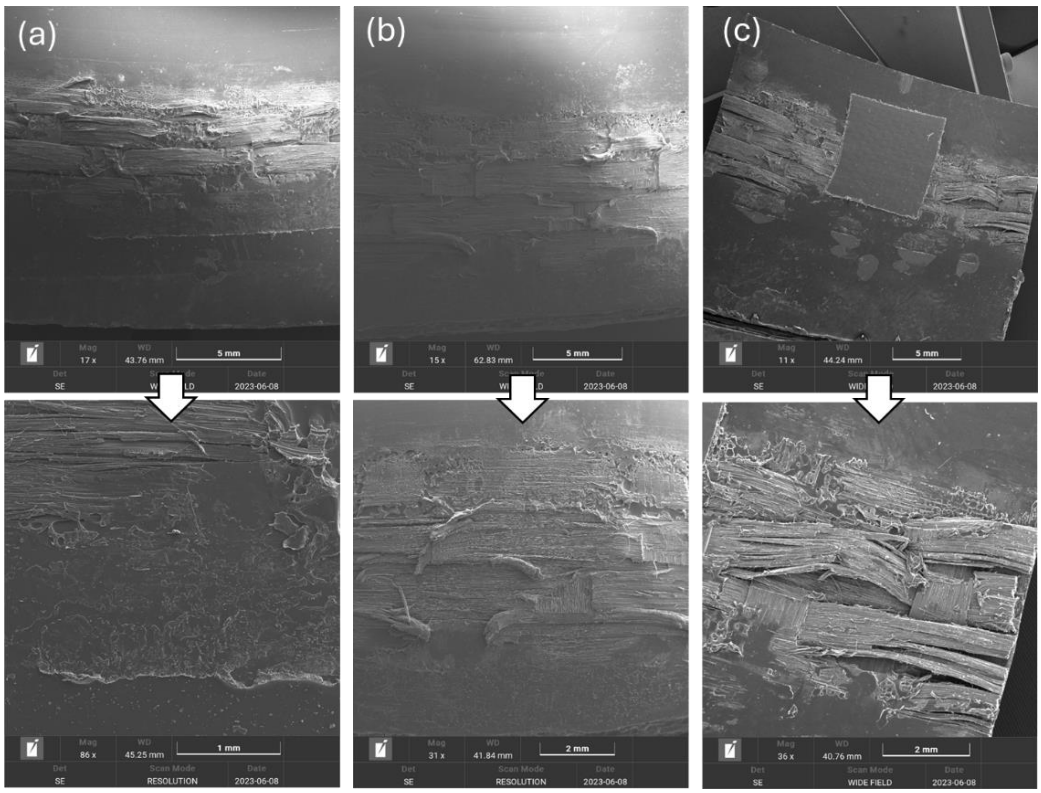

Figure 57 SEM micrographs of fracture surfaces for (a) Set-up 1, (b) Set-up 2, and (c) Set-up 1-DEF thermoplastic induction welded joints after fatigue lap shear tests.

Table 10 Fatigue test load configuration and cycles to failure**.**

Manufacturing cases	% of static LSS	Applied load level [KN]	Cycles to Failure
Set-up 1	70%*	1,93	53303
Set-up 2	70%	3,7	3049
Set-up 1-DEF	94%	1,93	33609

* test stopped at 36000 cycles and restarted at 80% LSS

Figure 57 shows the fracture surfaces of the three tested configurations (Set-up 1, Set-up 2, and Set-up 1-DEF) after fatigue tests. In the case of Set-up 1, the fracture surface reveals the coalescence of multiple cavities and porosities (**Figure 57 (a)**), indicating fatigue-induced damage accumulation. This suggests that, over the course of the cyclic loading, voids and micro-defects formed and merged, progressively weakening the joint.

The presence of these defects likely reduced the joint overall fatigue life by accelerating crack initiation and growth. In contrast, Set-up 2, despite showing some fiber-matrix debonding, displayed significantly less mesh tearing compared to the quasi-static test case as illustrated in **Figure 57 (b)**. This suggests a different failure mode under fatigue loading, likely driven by more distributed stresses in the bondline that inhibited the propagation of tearing through the fiber mesh. On the other hand, the specimen with the artificially introduced defect (Set-up 1-DEF, **Figure 57 (c)**) exhibited clear signs of mesh tearing, which were more prominent than in Set-up 1. The localized tearing observed is indicative of a predominantly intralaminar failure mechanism, likely triggered by the presence of the PTFE adhesive tape acting as a stress concentrator.

5.2.5 PM Sensor Performance Evaluation

Detection Sensitivity: Size Estimation and Defect Localization

The evaluation of the PM sensor detection sensitivity, in terms of defect size estimation and localization, reveals a promising capability for identifying variations in the electromagnetic properties of CFRTP laminates. As demonstrated in **Figure 15 (a)** and **Figure 16 (a)** of **Article 2**, the sensor effectively responds to changes in defect size and position, providing valuable insights for SHM applications.

At a lower frequency of 3 MHz, **Figure 15 (a)** of **Article 2**shows a slight increase in the reception loop voltage **as defect size increases**, a trend that is more pronounced at the higher frequency of 5.3 MHz, where the sensor demonstrates its highest sensitivity. The underlying mechanism is related to the local changes in the laminate electrical properties, where an increase in defect size reduces the intensity of the induced currents. This reduction in current intensity diminishes the magnetic field opposing the excitation loop, resulting in a greater magnetic flux being concatenated to the reception loop, thereby increasing the induced voltage.

In terms of **defect localization**, **Figure 16 (a)** of **Article 2** highlights the variation in sensor response as the defect is positioned at different depths within the material. A consistent decrease in voltage is observed as the defect moves deeper, following the exponential attenuation of induced current density with depth. When the defect is closer to the surface, higher-intensity induced currents are affected more prominently, altering the trajectory of the magnetic flux and increasing the induced voltage in the reception

loop. However, as the defect is placed deeper within the laminate, the impact on induced currents diminishes, leading to less significant changes in the measured magnetic flux.

These results underscore the effectiveness of the PM sensor in both estimating defect size and localizing damage within CFRP laminates. The sensor sensitivity to electromagnetic property variations shows considerable potential for SHM applications, particularly in detecting and tracking defect propagation in laminated composites.

Performance in Near-Real Application Conditions

The performance of the PM sensor under near-real application conditions was evaluated by **inspecting thermoplastic welded joints** both before and after the machining operation used to prepare the lap-joint specimens. The purpose of these inspections was twofold: **first**, to assess the **sensor sensitivity** in detecting damage (specifically, the lack of weld in set-up 1-DEF, **Table 8**), and **second**, to evaluate the **effect of reduced specimen size** on the sensor performance, as this would be the size used during subsequent fatigue tests aimed at assessing sensor capability under cyclic loading.

Before the machining operation, the PM sensor demonstrated the ability to detect the lack of weld across almost the entire frequency range as illustrated by the black line in **Figure 58**, with the exception of the very lowest frequencies, where the presence of noise obscured defect detection. Notably, the damage sensitivity (ΔV) peaked at around 6 MHz, indicating the optimal performance of the sensor at this frequency for detecting defects.

Following the machining operation, the PM sensor was again placed in the overlap zone to assess how the reduced sample width impacted sensitivity, as shown by the red line in **Figure 58**. The results indicated a significant reduction in defect detection sensitivity, attributed to the distortion of the induced eddy currents caused by the narrower sample width. Although a sensitivity peak remained identifiable, its intensity was markedly diminished, highlighting the challenges posed by specimen size reduction on sensor performance. This factor was considered during the interpretation of results obtained in the subsequent fatigue tests.

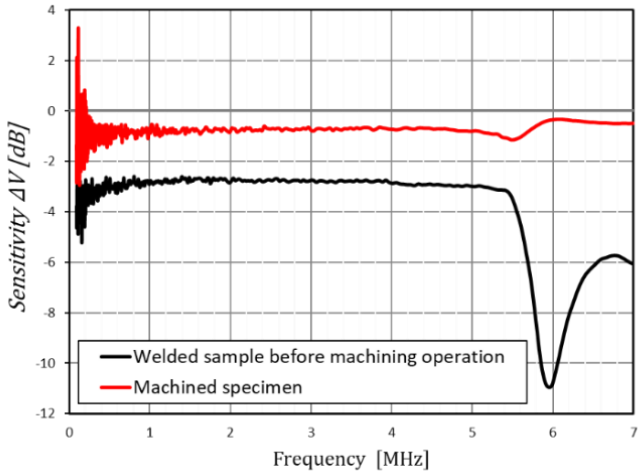

Figure 58 Frequency response of PM sensor when placed on both welded samples before machining operations and machined specimen.

Subsequent **fatigue tests** were performed on specimens with the PM sensor attached, aiming to evaluate its ability to detect the nucleation and propagation of damage. **Figure 59** illustrates the post-processed signals from both the SG and PM sensor during the fatigue test on a Set-up 1 specimen. The SG was effective in detecting the approaching failure, with its signal drifting noticeably towards the final cycles. The PM sensor signal exhibited the same oscillatory pattern as the SG signal, as the SG, being a conducting material through which current flows, generated a magnetic field that influenced the voltage induced in the PM sensor reception loop.

However, as the specimen approached failure, the SG clearly captured the deformation and the progressive drift, indicating damage propagation. In contrast, the PM sensor did not capture this drift. The reduced sensitivity of the PM sensor, likely due to the edge effect, limited its ability to fully assess damage progression. This diminished sensitivity highlights the need to eliminate the edge effect by conducting tests on larger specimens, which would also bring the experimental setup closer to the sensor operational conditions during its working life.

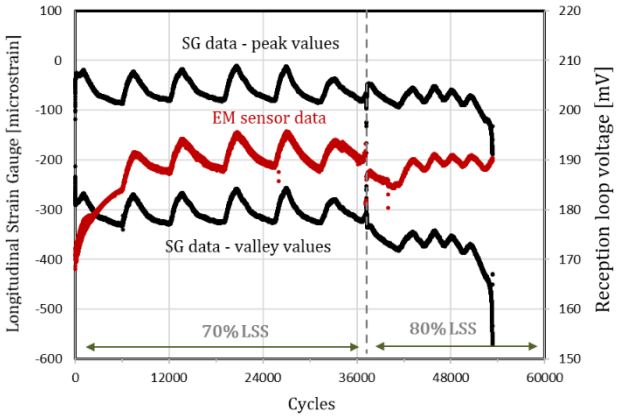

Figure 59 SG and PM sensor data collected during the fatigue tests of set-up 1 specimen.

In conclusion, the current design of the PM sensor did not exhibit a significant level of sensitivity in detecting damage during fatigue testing. The following section will provide insights into the factors contributing to this limitation and explore potential modifications to improve the sensor performance.

5.2.6 Modification of the Sensing Approach: H Sensor

During the fatigue tests conducted to assess the performance of the PM sensor, it became evident that the sensor, in its current configuration, was unable to detect damage nucleation and propagation. As a purely magnetic method, the expectation was that damage mechanisms such as mesh tearing and intralaminar fractures would alter the distribution of eddy currents in the carbon fiber—the conductive element of the composite. This disturbance in the eddy currents would, in theory, be detectable by the PM sensor. However, the analysis of fracture surfaces, as shown in **Figure 57**, revealed that the primary damage mechanisms during fatigue occurred predominantly in the matrix of the composite, which is primarily composed of resin, an insulating material with negligible conductivity. This concentration of damage within the dielectric matrix rather than in the carbon fiber likely explains the PM sensor inability to detect these changes, as the eddy current distribution in the conductive fibers was minimally affected.

These observations suggest that the current sensor configuration may not be sensitive enough to detect damage in the matrix-dominated failure modes of CFRP materials. Given the nature of damage propagation in the resin, a modification of the sensor to measure changes in dielectric permittivity—rather than relying solely on changes in conductivity—could potentially improve its damage detection capability. By shifting focus to dielectric properties, the sensor might better capture the matrix-related damage phenomena that dominate in these fatigue scenarios.

In light of the limited sensitivity of the PM sensor, it was decided to modify the sensing element by replacing the loop with two electrodes capable of measuring the electric field. **Figure 6** of **Article 2** provides a schematic representation of this updated sensor, and its working principle is detailed in **paragraph 4** of the same article. This revised approach is commonly referred to as a **hybrid method** because it combines magnetic induction with the analysis of the resulting electric field [193]. This modification is based on the fact that the electric field generated in the sensor is influenced by both the material electrical conductivity and dielectric permittivity. As can be demonstrated (see paragraph 2.1 of Article 2):

$$\boldsymbol{E} = \frac{\boldsymbol{J_f}}{\sigma} + (\varepsilon_r - 1)\boldsymbol{E_{applied}} \tag{66}$$

where $\boldsymbol{E_{applied}}$ is the local electric field induced inside a conductive structure by magnetic induction. Thus, the measured electric field $\boldsymbol{E}$ is a function of these two material properties, enhancing the sensor ability to detect damage by accounting for variations in both electrical conductivity (σ) and dielectric properties (ε_r) of the composite.

5.2.7 H Sensor Performance Evaluation

Detection Sensitivity: Size Estimation and Localization of Defects

In evaluating the detection sensitivity of the H sensor for size estimation and defect localization, **Figure 15 (b)** and **Figure 16 (b)** of **Article 2** demonstrate its capability to identify anomalies affecting the electromagnetic properties of CFRP laminated composites as defect size and position vary. Unlike the PM sensor, the H sensor signal does not exhibit a straightforward trend because its measurements are influenced by both local electrical conductivity and dielectric permittivity, as represented by equation (66). These two properties contribute to the electric field in ways that may either reinforce or oppose each other, complicating the interpretation of signal variations as the defect size increases.

From **Figure 15 (b)** of **Article 2,** a noticeable increase in voltage across the electrodes is seen for an excitation frequency of 5.7 MHz when the defect size reaches 25 mm². This increase is likely due to a rise in local dielectric permittivity as the size of the PTFE adhesive tapes embedded in the laminate increases. Smaller defects, such as the 4 mm² defect, exhibit an elevated voltage due to a stronger contribution from free charges in the carbon fiber reinforcement. For larger defects, the polarization effect dominates, while for smaller ones, the conduction phenomena also play a significant role. This combination of influences results in an overall increase in the measured electric field. Conversely, at 3 MHz, where lower damage sensitivity is expected, the sensor does not show significant voltage changes as defect size varies.

Figure 16 (b) of **Article 2** explores the sensor response when the defect position is changed along the thickness of the material. At 3 MHz, a gradual reduction in voltage across the electrodes occurs as the PTFE adhesive square approaches the surface, driven by an increase in dielectric permittivity and a corresponding amplification of the measured electric field. However, at 5.7 MHz, the sensor response becomes less consistent, likely due to variations in the distribution of free charges along the carbon fibers and shifts in the alignment of electric dipoles within the polymer matrix and PTFE tape. This highlights the complex interaction of the electric field components in detecting and localizing defects based on the position and size of the anomaly.

Performance Evaluation in Near-Real Application Environments

The performance evaluation of the H sensor for SHM in thermoplastic welded joints focused on assessing its ability to detect damage and characterize the electromagnetic response under near-real application conditions. **Figure 18 of Article 2** illustrates the H sensor response across 0.1 to 7 MHz frequency range, comparing the sensor behavior in pristine versus defective welded joints.

For frequencies below 5 MHz, the sensor did not exhibit significant signal variations from the baseline, similar to the earlier observations with the PM sensor. Nevertheless, in the frequency range of 5 to 7 MHz, the H sensor demonstrated a notable increase in damage sensitivity, with peak values exceeding those detected by the PM sensor.

When analyzing the electric field variations with the H sensor as defect size and position varied, the results showed less clarity compared to the PM sensor. However, the H sensor sensitivity to defects in thermoplastic welded joints was significantly higher, with signal deviations from the baseline reaching around 8 dB at an excitation frequency of 5.9 MHz, compared to the PM sensor 1.5 dB. This demonstrates the H sensor improved capability in identifying defect-induced changes in electromagnetic properties in welded CFRP joints.

In conclusion, combining magnetic and electric field measurements offers a promising method for detecting changes in damage-induced electrical properties in thermoplastic welded joints. While the purely magnetic approach provides valuable insights into damage localization, the hybrid method incorporating both fields shows superior sensitivity to damage, making it a potential tool for SHM applications.

5.3 Summary of Chapter 5

Chapter 5 presents the results and discussions for both **CASE I**, involving the development of an ECT probe for real-time process monitoring, and **CASE II**, focused on EM sensors for SHM applications in thermoplastic welded joints.

In **CASE I**, a sensitivity analysis led to the final configuration of the ECT probe, which exhibited strong performance in detecting wormhole defects. Lower-side inspections revealed a progressive reduction in conductivity correlating with the increasing defect size, while upper-side inspections failed to detect the defects. Interestingly, an inverse relationship between conductivity values on the upper and lower surfaces was consistently observed, suggesting potential indicators for defect presence. Furthermore, a correlation between microhardness, UTS, and conductivity was established, offering valuable insights for integrating electrical conductivity measurements into process

monitoring frameworks. This enables real-time prognosis of weld quality by detecting process deviations related to microstructural changes.

In **CASE II**, the PM sensor development began with a focus on the reflection method, which was selected due to practical considerations. The sensor demonstrated strong performance in detecting defects in CFRP laminates and thermoplastic induction welded joints. Numerical models validated the sensor sensitivity, showing that 5HS woven fabric laminates had higher sensitivity to defects than other configurations. However, fatigue testing highlighted limitations in the PM sensor sensitivity, leading to modifications in the sensor design.

The introduction of the H sensor, which measures the electric field, showed promise in improving damage detection capabilities. Unlike the PM sensor, the H sensor exhibited more complex interactions between the electric field components, leading to an unclear correlation between the sensor signal and defect size or location. Nevertheless, the H sensor demonstrated enhanced sensitivity to defects, particularly when capturing variations in dielectric permittivity. This hybrid approach, combining magnetic and electric field measurements, demonstrated superior damage sensitivity, making it a strong candidate for SHM applications in thermoplastic welded joints.

Chapter 6

6 Author's Indexed Scientific Publications

6.1 Scientific Publications 1

Title:	Monitoring of thermoplastic induction welding defects. Use of electromagnetic properties as a predictive tool
Authors:	M. Mazzeschi, K. C. Nuñez, E. Cañibano, and J. C. Merino
Journal:	Structural Health Monitoring - An International Journal (ISSN: 1475-9217)
Journal Metrics:	Index Base JCR, Impact Index 6.6, Quartile Q1 Instruments & Instrumentation 6/63
Volume:	22
Number:	3
Pages:	1-15
Date of publication:	8 July 2022
DOI:	https://doi.org/10.1177/14759217221111979

Abstract: The health of thermoplastic induction welded joints was evaluated by monitoring the electromagnetic response to a time variant magnetic field through a local measurement of the attenuated and reflected field. For this purpose, a numerical model was developed to study how the joint interface affects this response in the presence and absence of a delamination and as a function of the electromagnetic characteristics of a susceptor. Using a single loop coil geometry as local magnetic field excitation and measurement, the frequency range at which the highest damage detection sensitivity occurs has been identified for different sizes of a delamination in the bond line. It has been found that the presence of a susceptor reduces the capability of damage detection for the considered values of electromagnetic properties. The obtained results are the starting point for further research activities aimed at developing an electromagnetically based sensitive layer for monitoring the health of thermoplastic joints, capable of detecting and quantifying joint damage and assessing residual fatigue life.

6.2 Scientific Publication 2

Title:	Structural health monitoring of composite laminates in thermoplastic induction welded joints using electromagnetic field technique
Authors:	M. Mazzeschi, S. Farhangdoust, E. Cañibano, J. C. Merino, and K. C. Núñez
Journal:	Sensors & Actuators: A. Physical (ISSN: 0924-4247)
Journal Metrics:	Index base JCR, Impact Index 4.1, Quartile Q1 Instruments & Instrumentation 16/76
Volume:	375
Number:	2024
Pages:	115540
Date of publication:	31 May 2024
DOI:	https://doi.org/10.1016/j.sna.2024.115540

Abstract: This research paper explores the assessment of electrical property changes resulting from damage in a Carbon Fiber Reinforced Polymers (CFRP) laminate and its thermoplastic induction-welded joints. Controlled variations in electrical conductivity and dielectric permittivity were achieved by incorporating square Polytetrafluoro- ethylene (PTFE) adhesive tapes into both CFRP laminates and the bondline interfaces of induction-welded components. Two elementary and effective sensors, capable of measuring magnetic (Purely Magnetic sensor) and electric fields (Hybrid sensor), were employed to detect these property changes induced by a sinusoidal magnetic field generated by a nearby coil. Both sensors exhibited remarkable sensitivity in identifying variations induced by the smallest artificial defects, measuring 2×2 mm in size. Furthermore, the PM sensor displayed a discernible signal trend corresponding to changes in defect size ranging from 4 to 225 mm square, as well as variations in position within the thickness of the CFRP laminate, extending to a depth of 1.7 mm. These findings underscore the potential of electromagnetic-based structural health monitoring (ESHM) techniques for moni- toring the condition of a thermoplastic composite structure and its induction-welded joints.

6.3 Scientific Publication 3

Title:	Electrical conductivity field analysis: A prognostic instrument for real time monitoring of friction stir welding process
Authors:	M. Mazzeschi, M. Sanz, J. C. Monge, E. Cañibano, C. P. Rodriguez-Juan, and K. C. Núñez
Journal:	Journal of Manufacturing Processes (ISSN: 1526-6125)
Journal Metrics:	Index base JCR, Impact Index 6.1, Quartile Q1 Engineering, Manufacturing 12/68
Volume:	131
Number:	2024
Pages:	93-110
Date of publication:	9 September 2024
DOI:	https://doi.org/10.1016/j.jmapro.2024.09.005

Abstract: Constant monitoring of manufacturing processes is crucial for ensuring high-quality products and cost-effectiveness. Non-destructive testing (NDT) techniques, such as eddy current testing (ECT), offer a direct and accurate means of evaluating weld quality in real-time. ECT can assess microstructural changes in welded materials by measuring electrical conductivity. Establishing a robust correlation between electrical conductivity and microstructural changes induced by FSW process parameters remains a critical step to bridge existing knowledge gaps. In this study, electrical conductivity field analysis using eddy currents was conducted on AA6082-T6 FSW joints. A pivotal factor controlling process heat input and influencing defect formation and weld microstructural features is the ratios of FSW tool rotational speed (ω) to travel speed (v). Previous works often evaluated only one set of process parameters, while our study examines multiple combinations of ω and welding speed v to develop a more robust correlation between electrical conductivity and microstructural changes. Both defective and defect-free joints were obtained employing various ω/v ratio and electrical conductivity results were compared with hardness measurements and tensile test results. The analysis reveals a consistent trend between electrical conductivity variations, microstructural changes in weld zones, and microhardness as the ω/v ratio varies. Our findings show that, at a constant travel speed, an increasing ω/v ratio is associated with enhanced microhardness and decreased electrical conductivity, attributed to grain refinement. Conversely, at a constant rotational speed, a higher ω/v ratio leads to increased electrical conductivity, due to the enhanced dissolution of strengthening precipitates. Furthermore, analyzing electrical conductivity profiles and identifying local maxima corresponding to weld failure zones

could strengthen the correlation. This approach suggests the potential to assess variations in mechanical properties resulting from process drift, specifically influenced by changes in the ω/v parameter over time. Microstructural analysis through electrical conductivity evaluation emerges as a valuable and predictive tool for assessing weld properties, with promising applications in process monitoring.

Chapter 7

7 Conclusions and Future Works

The overall objective of this research was to **advance** the **application of electromagnetic-based** monitoring approaches, specifically ECT and electromagnetic SHM sensor, in manufacturing and structural health monitoring of aerospace structural joints. This goal has been approached through both theoretical and experimental investigations, targeting specific applications in FSW aluminium alloys and thermoplastic welded CFRP joints.

The first step in achieving this goal involved identifying key aerospace structural joints where the use of electromagnetic-based monitoring techniques remains underdeveloped, leading to significant potential for improvement. **Chapter 2** provided the exhaustive review of the state of the art that was conducted, emphasizing the critical role of **FSW** and **thermoplastic induction welded joints** in the aerospace sector. This review highlighted the gap in existing methodologies and the potential for significant improvements through the application of electromagnetic monitoring. As a result, two specific cases were selected for focused research: **CASE I**, which targets real-time monitoring of the FSW process by ECT, and **CASE II**, dedicated to the SHM of thermoplastic welded joints using EM sensors.

In **CASE I**, the research aimed to correlate ECT signals with the microstructural properties of welded joints, a key element for facilitating the application of this NDT method in a real-time process monitoring of FSW. In **Chapter 5**, through a comprehensive sensitivity analysis based on numerical simulations, an **optimized ECT probe** was designed. The probe demonstrated its effectiveness in detecting subsurface defects (particularly wormhole-type defects) of the FSW joints, proving its capability for defect detection in these critical areas. The research also found a notable correlation between electrical conductivity, microhardness, and mechanical properties such as UTS, suggesting that ECT measurements can serve as a robust tool for real-time monitoring of welding quality. These findings, detailed in **Article 3**, provide a solid foundation for future developments in the application of the method for real time monitoring applications.

In **CASE II**, the focus shifted to SHM applications for thermoplastic welded joints. Two sensor configurations were developed during the course of investigation: the **PM sensor**, based on a purely magnetic approach, and the **H sensor**, which combines magnetic and electric field measurements. An extensive comparison between purely magnetic methods, specifically attenuation and reflection, was also conducted, as detailed in **Article 1**. This comparison laid the foundation for selecting the most appropriate sensing configuration for detecting damage in CFRP laminates, helping to inform the design choices for the PM sensor and subsequently H sensor. While the PM sensor provided valuable insights, its sensitivity was limited when detecting dielectric variations within the welds, prompting the development of the H sensor. The H sensor exhibited significantly better sensitivity to changes in dielectric properties caused by damage, as evidenced in **Chapter 5** and more extensively in **Article 2**, enabling more precise defect localization and assessment of damage propagation in CFRP laminates. This

enhancement not only demonstrates the utility of hybrid electromagnetic sensors in SHM applications but also paves the way for broader use in detecting damage in complex thermoplastic composite structures.

Limitation of the proposed approaches

The proposed electromagnetic-based approach is a promising tools for real-time process monitoring and SHM in aerospace applications. However, the developed sensors have limitations that must be addressed to maximize their efficacy in the field.

One significant limitation of ECT probes/EM sensors is their **localized inspection range** compared to other techniques, such as guided waves, which can cover larger areas. This limitation means that electromagnetic monitoring typically requires the placement of multiple sensors at critical locations to obtain sufficient coverage. While effective, this approach can be cost-prohibitive if large areas need continuous monitoring, especially in complex aerospace structures.

Penetration depth constraints are particularly relevant for NDT methods that rely on electromagnetic phenomena. In aerospace applications, material thickness typically ranges between 3 mm and 10 mm for both aluminum alloys and CFRP, though specific thicknesses vary by application. Due to the skin effect, ECT penetration depth is inherently limited in these materials, reducing its effectiveness in detecting subsurface defects at greater depths or for components with thicknesses near the upper end of the range. This limitation makes it challenging to conduct deeper inspections compared to other NDT methods with broader depth capabilities, thereby necessitating complementary techniques or additional design considerations when testing thicker sections.

Temperature sensitivity represents another challenge that varies between real-time process monitoring and SHM applications. In **FSW process monitoring**, temperature changes are manageable; monitoring equipment can record variations in process temperature, and external disturbances can be minimized in a controlled manufacturing environment. However, for **SHM applications**, where sensors monitor in-service components, unexpected temperature changes can significantly impact sensor accuracy and signal interpretation. Without local temperature evaluation, these sudden variations can introduce signal errors, underscoring the need for reliable temperature compensation or additional thermal sensors when monitoring aerospace structures in varying environmental conditions.

The potential for **electromagnetic interference (EMI)** presents another critical limitation for electromagnetic-based monitoring techniques. In real-world aerospace environments, interference from external electromagnetic sources can degrade sensor accuracy, leading to false positives or noise in the data. To address this, electromagnetic shielding is essential to reduce susceptibility to EMI and ensure reliable measurements, although this can increase system complexity and cost.

Edge effects also impact sensor performance, particularly by reducing sensitivity when monitoring near geometrical features or edges. Edge effects can create signal distortions, masking or weakening the detection of defects. This issue is particularly pronounced in complex joint geometries where edges and corners are critical inspection points. As a result, the design of ECT probes and EM sensors may need to be tailored to

address edge sensitivity, especially in applications requiring precise boundary assessments.

Future Research Directions

The author has identified several key areas for future research based on the findings of this investigation.

1. **Enhanced Numerical Models:** Future models should integrate variations in conductivity linked to weld microstructure to move beyond simple defect detection. By considering microstructural phenomena like grain refinement and thermal gradients, these models could more accurately predict weld integrity and mechanical properties such as UTS and microhardness. This comprehensive modeling could also extend to more complex materials, like FSW of CFRP, which presents additional challenges in conductivity due to its anisotropy and fiber-matrix interaction.

2. **Real-Time Monitoring Implementation:** Established correlations between electrical conductivity and weld integrity highlight the feasibility of developing real-time monitoring systems. However, addressing ECT sensitivity to temperature changes is crucial for accurate measurement in practical FSW processes. Compensating for these effects is essential for data reliability, especially in real-time applications. Integrating the ECT probe into an actual FSW machine for process trials will help refine defect detection and improve weld quality assessment during production.

3. **AI Integration:** Leveraging physics-based machine learning algorithms can enhance ECT data interpretation by combining it with FSW signals and other NDT data. Such AI models would optimize real-time monitoring without requiring large data sets for training. The objective is to develop an AI-based system capable of detecting subtle changes in weld quality, predicting defects, and enhancing process optimization, potentially leading to a digital twin that simulates and corrects the FSW process in real time.

4. **Hybrid Approaches:** The combined use of magnetic and electric field measurements, as demonstrated with the H sensor, offers a robust method for detecting damage-related changes in electrical properties. This hybrid approach should be further optimized for sensitivity and applicability across a broader range of materials and joint types. Extending these techniques to monitor complex joints like CFRP or similar composites could enhance SHM capabilities, improving detection accuracy and reliability. Additionally, coupling this approach with advanced analytics and machine learning can provide real-time insights for various aerospace structural applications. and provide more precise diagnostics for structural health monitoring.

5. **Evaluation of EMI Impact on Sensor Performance**: As electromagnetic-based monitoring systems are increasingly integrated into real-time and SHM applications, assessing the influence of EMI on sensor performance becomes essential. EMI can compromise data accuracy, particularly in environments with multiple electrical systems. Future research should focus on characterizing EMI

effects across varying operational conditions and develop effective shielding strategies or interference mitigation techniques.

This research presents significant advancements in the development and application of ECT probes and EM sensors for defect detection and structural health monitoring in aerospace applications. The work establishes a strong foundation for integrating these technologies into real-time process monitoring and SHM systems, with clear future directions for enhancing their performance and reliability. By refining the sensors and integrating advanced AI techniques, these systems can significantly improve the safety and efficiency of aerospace manufacturing processes.

References

[1] G.-G. M. Estimates, “eVTOL Aircraft Market,” 2024. [Online]. Available: https://www.globalmarketestimates.com/market-report/evtol-aircraft-market-3771

[2] A. Acket-Goemaere, R. Brukardt, J. Klempner, A. Sierra, and B. Stokes, “Space: The $1.8 trillion opportunity for global economic growth,” 2024. [Online]. Available: https://www.mckinsey.com/industries/aerospace-and-defense/our-insights/space-the-1-point-8-trillion-dollar-opportunity-for-global-economic-growth

[3] H. Nishida, V. Carvelli, T. Fujii, and K. Okubo, “Thermoplastic vs. thermoset epoxy carbon textile composites,” *IOP Conf. Ser. Mater. Sci. Eng.*, vol. 406, p. 12043, Sep. 2018, doi: 10.1088/1757-899X/406/1/012043.

[4] I. A. Institute, “Global Aluminium Recycling : A Cornerstone of Sustainable Development,” 2009.

[5] R. S. Mishra and Z. Y. Ma, “Friction stir welding and processing,” *Mater. Sci. Eng. R Reports*, vol. 50, no. 1–2, pp. 1–78, 2005, doi: 10.1016/j.mser.2005.07.001.

[6] T. Majeed, M. Atif, N. Alam, Y. Mehta, and A. Noor, “Friction stir welding : A sustainable manufacturing process,” *Mater. Today Proc.*, vol. 46, pp. 6558–6563, 2021, doi: 10.1016/j.matpr.2021.04.025.

[7] M. Bevilacqua, F. Emanuele, A. D. Orazio, A. Forcellese, and M. Simoncini, “Sustainability analysis of friction stir welding of AA5754 sheets,” *Procedia CIRP*, vol. 62, pp. 529–534, 2017, doi: 10.1016/j.procir.2016.06.081.

[8] A. Shrivastava, M. Krones, and F. E. Pfefferkorn, “Comparison of energy consumption and environmental impact of friction stir welding and gas metal arc welding for aluminum,” *CIRP J. Manuf. Sci. Technol.*, vol. 9, pp. 159–168, 2015, doi: https://doi.org/10.1016/j.cirpj.2014.10.001.

[9] K. Mehta, “Sustainability in Welding and Processing,” 2019, pp. 125–145. doi: 10.1007/978-3-030-03276-0_6.

[10] S. Azeez and E. Akinlabi, “Sustainability of manufacturing technology: friction stir welding in focus,” *Prog. Ind. Ecol. An Int. J.*, vol. 12, p. 419, Jan. 2018, doi: 10.1504/PIE.2018.097188.

[11] D. Mishra, R. B. Roy, S. Dutta, S. K. Pal, and D. Chakravarty, “A review on sensor based monitoring and control of friction stir welding process and a roadmap to Industry 4.0,” *J. Manuf. Process.*, vol. 36, no. November, pp. 373–397, 2018, doi: 10.1016/j.jmapro.2018.10.016.

[12] M. Liu, S. Fang, H. Dong, and C. Xu, “Review of digital twin about concepts, technologies, and industrial applications,” *J. Manuf. Syst.*, vol. 58, no. June, pp. 346–361, 2021, doi: 10.1016/j.jmsy.2020.06.017.

[13] R. W. Ross, *Integrated vehicle health management in aerospace structures*. Elsevier, 2016. doi: 10.1016/B978-0-08-100148-6.00001-9.

[14] J. García-Martín, J. Gómez-Gil, and E. Vázquez-Sánchez, “Non-destructive techniques based on eddy current testing,” *Sensors*, vol. 11, no. 3, pp. 2525–2565, 2011, doi: 10.3390/s110302525.

[15] S. Kumar, M. Vishwakarma, and P. Akhilesh, “Advances and Researches on Non Destructive Testing : A Review,” *Mater. Today Proc.*, vol. 5, no. 2, pp. 3690–3698, 2018, doi: 10.1016/j.matpr.2017.11.620.

[16] E. B. Shell, R. G. Buchheit, and B. Zoofan, “Correlation of residual fatigue life

with quantified NDE measurements," *Int. J. Fatigue*, vol. 27, no. 2, pp. 105–112, 2005, doi: 10.1016/j.ijfatigue.2004.06.007.

[17] A. Wronkowicz, K. Dragan, and K. Lis, "Assessment of uncertainty in damage evaluation by ultrasonic testing of composite structures," *Compos. Struct.*, vol. 203, no. July, pp. 71–84, 2018, doi: 10.1016/j.compstruct.2018.06.109.

[18] M. Saeedifar and D. Zarouchas, "Damage characterization of laminated composites using acoustic emission: A review," *Compos. Part B Eng.*, vol. 195, no. January, p. 108039, 2020, doi: 10.1016/j.compositesb.2020.108039.

[19] F. Ciampa, P. Mahmoodi, F. Pinto, and M. Meo, "Recent advances in active infrared thermography for non-destructive testing of aerospace components," *Sensors (Switzerland)*, vol. 18, no. 2, 2018, doi: 10.3390/s18020609.

[20] A. N. AbdAlla, M. A. Faraj, F. Samsuri, D. Rifai, K. Ali, and Y. Al-Douri, "Challenges in improving the performance of eddy current testing: Review," *Meas. Control (United Kingdom)*, vol. 52, no. 1–2, pp. 46–64, 2019, doi: 10.1177/0020294018801382.

[21] H. Towsyfyan, A. Biguri, R. Boardman, and T. Blumensath, "Successes and challenges in non-destructive testing of aircraft composite structures," *Chinese J. Aeronaut.*, vol. 33, no. 3, pp. 771–791, 2020, doi: 10.1016/j.cja.2019.09.017.

[22] A. Kroworz and A. Katunin, "Non-destructive testing of structures using optical and other methods: A review," *SDHM Struct. Durab. Heal. Monit.*, vol. 12, no. 1, pp. 1–17, 2018, doi: 10.3970/sdhm.2018.012.001.

[23] Q. Wu, K. Dong, X. Qin, Z. Hu, and X. Xiong, "Magnetic particle inspection: Status, advances, and challenges — Demands for automatic non-destructive testing," *NDT E Int.*, vol. 143, no. December 2023, p. 103030, 2024, doi: 10.1016/j.ndteint.2023.103030.

[24] C. Harding and G. Hugo, "Review of Literature on Probability of Detection for Liquid Penetrant Nondestructive Testing," *DSTO Def. Sci. Technol. Organ.*, pp. 0–40, 2011, [Online]. Available: http://oai.dtic.mil/oai/oai?verb=getRecord&metadataPrefix=html&identifier=ADA560011

[25] D. Balageas, "Introduction to Structural Health Monitoring," 2006, pp. 13–43.

[26] C. Farrar and K. Worden, *Structural Health Monitoring A Machine Learning Perspective*. 2013. doi: 10.1002/9781118443118.

[27] D. A. Tibaduiza Burgos, R. C. Gomez Vargas, C. Pedraza, D. Agis, and F. Pozo, *Damage identification in structural health monitoring: A brief review from its implementation to the use of data-driven applications*, vol. 20, no. 3. 2020. doi: 10.3390/s20030733.

[28] C. P. Fritzen, "Vibration-Based Techniques for Structural Health Monitoring," *Struct. Heal. Monit.*, pp. 45–224, 2010, doi: 10.1002/9780470612071.ch2.

[29] P. Jiao, K. J. I. Egbe, Y. Xie, A. M. Nazar, and A. H. Alavi, "Piezoelectric sensing techniques in structural health monitoring: A state-of-the-art review," *Sensors (Switzerland)*, vol. 20, no. 13, pp. 1–21, 2020, doi: 10.3390/s20133730.

[30] A. Güemes and J. M. Menendez, "Fiber-Optic Sensors," in *Structural Health Monitoring*, D. Balageas, C. Fritzen, and A. Güemes, Eds., Wiley-ISTE, 2006, pp. 225–285.

[31] M. Giglio, A. Manes, and C. Sbarufatti, *MEMS for structural health monitoring in aircraft*. Woodhead Publishing Limited, 2013. doi: 10.1533/9780857096487.2.220.

[32] T. N. Tallman and D. J. Smyl, "Structural health and condition monitoring via electrical impedance tomography in self-sensing materials: A review," *Smart*

Mater. Struct., vol. 29, no. 12, 2020, doi: 10.1088/1361-665X/abb352.
[33] D. P. Barton, "Comparative Vacuum Monitoring (CVM^{TM})," in *Encyclopedia of Structural Health Monitoring*, 2009. doi: https://doi.org/10.1002/9780470061626.shm132.
[34] V. Giurgiutiu, "Other Sensors for SHM of Aerospace Composites," *Struct. Heal. Monit. Aerosp. Compos.*, pp. 297–315, 2016, doi: 10.1016/b978-0-12-409605-9.00008-8.
[35] S. Liu, Y. Sun, M. Gu, C. Liu, L. He, and Y. Kang, "Review and analysis of three representative electromagnetic NDT methods," *Insight Non-Destructive Test. Cond. Monit.*, vol. 59, no. 4, pp. 176–183, 2017, doi: 10.1784/insi.2017.59.4.176.
[36] Z. Li and Z. Meng, "A review of the radio frequency non-destructive testing for carbon-fibre composites," *Meas. Sci. Rev.*, vol. 16, no. 2, pp. 68–76, 2016, doi: 10.1515/msr-2016-0010.
[37] B. Feng, J. Wu, H. Tu, J. Tang, and Y. Kang, "A Review of Magnetic Flux Leakage Nondestructive Testing," *Materials (Basel).*, vol. 15, no. 20, 2022, doi: 10.3390/ma15207362.
[38] Y. Sun, Y. Kang, and C. Qiu, "A permanent magnetic perturbation testing sensor," *Sensors Actuators, A Phys.*, vol. 155, no. 2, pp. 226–232, 2009, doi: 10.1016/j.sna.2009.08.023.
[39] C. H. Gur, "Review of Residual Stress Measurement by Magnetic Barkhausen Noise Technique," *Mater. Perform. Charact.*, vol. 7, no. 4, pp. 504–525, Oct. 2018, doi: 10.1520/MPC20170080.
[40] S. Bao, M. Fu, S. Hu, Y. Gu, and H. Lou, "A Review of the Metal Magnetic Memory Technique." Jun. 19, 2016. doi: 10.1115/OMAE2016-54269.
[41] A. Sophian, G. Tian, and M. Fan, "Pulsed Eddy Current Non-destructive Testing and Evaluation: A Review," *Chinese J. Mech. Eng. (English Ed.*, vol. 30, no. 3, pp. 500–514, 2017, doi: 10.1007/s10033-017-0122-4.
[42] C. Sun, Y. Yu, H. Li, F. Wang, and D. Liu, "Quantitative Detection for Fatigue Natural Crack in Aero-Aluminum Alloy Based on Pulsed Eddy Current Technique," *Appl. Sci.*, vol. 14, no. 10, 2024, doi: 10.3390/app14104326.
[43] P. Boldrin, G. Fornasari, and E. Rizzo, "Review of Ground Penetrating Radar Applications for Bridge Infrastructures," *Ndt*, vol. 2, no. 1, pp. 53–75, 2024, doi: 10.3390/ndt2010004.
[44] S. Kingston *et al.*, "A sstdr methodology, implementations, and challenges," *Sensors*, vol. 21, no. 16, pp. 1–17, 2021, doi: 10.3390/s21165268.
[45] X. Li, "Eddy Current Techniques for Non-destructive Testing of Carbon Fibre Reinforced Plastic (CFRP)," *Univ. Manchester*, pp. 1–185, 2012, [Online]. Available: https://www.research.manchester.ac.uk/portal/files/54522762/FULL_TEXT.PDF
[46] Q. Liu, H. Sun, T. Wang, and X. Qing, "On-site health monitoring of composite bolted joint using built-in distributed eddy current sensor network," *Materials (Basel).*, vol. 12, no. 7, 2019, doi: 10.3390/ma12172785.
[47] Y. Si, J. P. Rouse, and C. J. Hyde, "Potential difference methods for measuring crack growth: A review," *Int. J. Fatigue*, vol. 136, no. March, 2020, doi: 10.1016/j.ijfatigue.2020.105624.
[48] N. Merah, "Detecting and measuring flaws using electric potential techniques," *J. Qual. Maint. Eng.*, vol. 9, no. 2, pp. 160–175, 2003, doi: 10.1108/13552510310482406.
[49] H. Brauer, K. Porzig, J. Mengelkamp, M. Carlstedt, M. Ziolkowski, and H. Toepfer, "Lorentz force eddy current testing: A novel NDE-technique,"

COMPEL - Int. J. Comput. Math. Electr. Electron. Eng., vol. 33, no. 6, pp. 1965–1977, 2014, doi: 10.1108/COMPEL-11-2013-0383.

[50] J. M. Otterbach, R. Schmidt, H. Brauer, M. Ziolkowski, and H. Töpfer, "Comparison of defect detection limits in Lorentz force eddy current testing and classical eddy current testing," *J. Sensors Sens. Syst.*, vol. 7, no. 2, pp. 453–459, 2018, doi: 10.5194/jsss-7-453-2018.

[51] A. Raine and M. Lugg, "Review of the alternating current field measurement inspection technique," *Sens. Rev.*, vol. 19, no. 3, pp. 207–213, 1999, doi: 10.1108/02602289910279166.

[52] R. E. Beissner, M. J. Sablik, and C. M. Teller, "Electric Current Perturbation Calculations for Half-Penny Cracks," *Rev. Prog. Quant. Nondestruct. Eval.*, pp. 1237–1254, 1983, doi: 10.1007/978-1-4613-3706-5_80.

[53] A. Tsuda, H. Kawai, Y. Yamaguchi, K. Inagaki, H. Hatanaka, and M. Tagami, "Fiber Waviness Detection by Electromagnetic Testing in Carbon Fiber Reinforced Plastics," pp. 1–6, 2016, [Online]. Available: http://creativecommons.org/licenses/by-nd/3.0/

[54] S. A. Grammatikos, M.-E. Kouli, G. Gkikas, and A. S. Paipetis, "Structural health monitoring of aerospace materials used in industry using electrical potential mapping methods," *Smart Sens. Phenomena, Technol. Networks, Syst. Integr. 2012*, vol. 8346, p. 83461K, 2012, doi: 10.1117/12.915492.

[55] C. Guo, W. Xu, M. Cai, S. Duan, J. Fu, and X. Zhang, "A Review: Application of Terahertz Nondestructive Testing Technology in Electrical Insulation Materials," *IEEE Access*, vol. 10, no. October, pp. 121547–121560, 2022, doi: 10.1109/ACCESS.2022.3222860.

[56] V. Anitha, A. Beohar, and A. Nella, *THz Imaging Technology Trends and Wide Variety of Applications: a Detailed Survey*, vol. 18, no. 2. Springer US, 2023. doi: 10.1007/s11468-022-01775-9.

[57] J. Wu, B. Nie, C. Zhang, Y. Li, J. Gao, and X. Wang, "Terahertz Non-destructive Imaging System Applied on Composite Materials Testing BT - Proceedings of the 5th China and International Young Scientist Terahertz Conference, Volume 2," C. Chang, Y. Zhang, Z. Zhao, and Y. Zhu, Eds., Singapore: Springer Nature Singapore, 2024, pp. 56–60.

[58] D. A. Tonga *et al.*, "Nondestructive Evaluation of Fiber-Reinforced Polymer Using Microwave Techniques: A Review," *Coatings*, vol. 13, no. 3, 2023, doi: 10.3390/coatings13030590.

[59] Q. Q. Ni, J. Hong, P. Xu, Z. Xu, K. Khvostunkov, and H. Xia, "Damage detection of CFRP composites by electromagnetic wave nondestructive testing (EMW-NDT)," *Compos. Sci. Technol.*, vol. 210, no. March, p. 108839, 2021, doi: 10.1016/j.compscitech.2021.108839.

[60] O. Iervolino and M. Meo, "A spiral passive electromagnetic sensor (SPES) for wireless and wired structural health monitoring," *Meas. Sci. Technol.*, vol. 27, no. 4, 2016, doi: 10.1088/0957-0233/27/4/045601.

[61] Z. Li, A. Haigh, C. Soutis, A. Gibson, R. Sloan, and N. Karimian, "Detection and evaluation of damage in aircraft composites using electromagnetically coupled inductors," *Compos. Struct.*, vol. 140, pp. 252–261, 2016, doi: 10.1016/j.compstruct.2015.12.054.

[62] N. Yusa *et al.*, "Detection of embedded fatigue cracks in Inconel weld overlay and the evaluation of the minimum thickness of the weld overlay using eddy current testing," *Nucl. Eng. Des.*, vol. 236, no. 18, pp. 1852–1859, 2006, doi: 10.1016/j.nucengdes.2006.02.011.

[63] G. Mook, R. Lange, and O. Koeser, “Non-destructive characterisation of carbon-fibre-reinforced plastics by means of eddy-currents,” *Compos. Sci. Technol.*, vol. 61, no. 6, pp. 865–873, 2001, doi: 10.1016/S0266-3538(00)00164-0.
[64] K. Koyama, H. Hoshikawa, and G. Kojima, “Eddy current nondestructive testing for carbon fiber-reinforced composites,” *J. Press. Vessel Technol. Trans. ASME*, vol. 135, no. 4, pp. 1–2, 2013, doi: 10.1115/1.4023253.
[65] A. McNab and J. Thomson, “An eddy current array instrument for application on ferritic welds,” *NDT E Int.*, vol. 28, no. 2, pp. 103–112, 1995, doi: 10.1016/0963-8695(94)00009-9.
[66] T. G. Santos, P. Vilaa, and R. M. Miranda, “Electrical conductivity field analysis for evaluation of FSW joints in AA6013 and AA7075 alloys,” *J. Mater. Process. Technol.*, vol. 211, no. 2, pp. 174–180, 2011, doi: 10.1016/j.jmatprotec.2010.08.030.
[67] Y. Sheiretov, “Deep Penetration Magnetoquasistatic Sensors,” 2001.
[68] L. S. Rosado, J. C. Gonzalez, T. G. Santos, P. M. Ramos, and M. Piedade, “Geometric optimization of a differential planar eddy currents probe for non-destructive testing,” *Sensors Actuators, A Phys.*, vol. 197, pp. 96–105, 2013, doi: 10.1016/j.sna.2013.04.010.
[69] A. Rakow and F. K. Chang, “A structural health monitoring fastener for tracking fatigue crack growth in bolted metallic joints,” *Struct. Heal. Monit.*, vol. 11, no. 3, pp. 253–267, 2012, doi: 10.1177/1475921711429497.
[70] D. Balageas, “HELP Layer for electromagnetic SHM of CFRP . M . Lemistre , D . Placko *, D . Balageas 2nd European Worshop on Structural Health Monitoring,” no. January 2004, 2014.
[71] G. Sorger *et al.*, “Non-destructive microstructural analysis by electrical conductivity: Comparison with hardness measurements in different materials,” *J. Mater. Sci. Technol.*, vol. 35, Sep. 2018, doi: 10.1016/j.jmst.2018.09.047.
[72] O. Postolache, A. L. Ribeiro, and H. Ramos, “Weld testing using eddy current probes and image processing,” *19th IMEKO World Congr. 2009*, vol. 1, no. January, pp. 6–10, 2009.
[73] W. Cheng, I. Komura, M. Shiwa, and S. Kanemoto, “Eddy current examination of fatigue cracks in inconel welds,” *J. Press. Vessel Technol. Trans. ASME*, vol. 129, no. 1, pp. 169–174, 2007, doi: 10.1115/1.2435718.
[74] R. Grimberg, A. Savin, R. Steigmann, and A. Bruma, “Eddy current examination of carbon fibres in carbon-epoxy composites and Kevlar,” *Int. J. Mater. Prod. Technol.*, vol. 27, no. 3–4, pp. 221–228, 2006, doi: 10.1504/IJMPT.2006.011272.
[75] X. E. Gros and K. Takahashi, “Monitoring Delamination Growth In Cfrp Materials Using Eddy Currents,” *Nondestruct. Test. Eval.*, vol. 15, no. 2, pp. 65–82, 1998, doi: 10.1080/10589759908952865.
[76] S. F. Dmitriev, A. V. Ishkov, A. O. Katasonov, V. N. Malikov, and A. M. Sagalakov, “Investigation of welded joints of aluminium alloys using subminiature eddy-current transducers,” *IOP Conf. Ser. Mater. Sci. Eng.*, vol. 327, no. 3, pp. 1–10, 2018, doi: 10.1088/1757-899X/327/3/032018.
[77] A. Ishkov and V. Malikov, *Subminiature Eddy Current Transducer for Inspection of Welded Joints Obtained by Friction Stir Welding*. Springer International Publishing, 2022. doi: 10.1007/978-3-030-85057-9_44.
[78] A. Lamarre, O. Dupuis, and M. Moles, “Complete inspection of friction stir welds in aluminum using ultrasonic and eddy current arrays,” *ASM Proc. Int. Conf. Trends Weld. Res.*, vol. 2005, pp. 219–225, 2005.
[79] M. R. Bhat and V. D. Ragupathy, “Characterisation of Friction Stir Weld

Discontinuities by Non-destructive Evaluation," *Trans. Indian Inst. Met.*, vol. 72, no. 11, pp. 2971–2979, 2019, doi: 10.1007/s12666-019-01813-x.

[80] J. Cheng, J. Qiu, H. Ji, E. Wang, T. Takagi, and T. Uchimoto, "Application of low frequency ECT method in noncontact detection and visualization of CFRP material," *Compos. Part B Eng.*, vol. 110, pp. 141–152, 2017, doi: 10.1016/j.compositesb.2016.11.018.

[81] K. Mizukami, Y. Mizutani, A. Todoroki, and Y. Suzuki, "Damage detection in CFRP aircrafts using eddy current testing and statistical diagnosis," 2015.

[82] S. Yamada, M. Katou, M. Iwahara, and F. P. Dawson, "Defect images by planar ect probe of meander-mesh coils," *IEEE Trans. Magn.*, vol. 32, no. 5 PART 2, pp. 4956–4958, 1996, doi: 10.1109/20.539300.

[83] J. O. Fava, L. Lanzani, and M. C. Ruch, "Multilayer planar rectangular coils for eddy current testing: Design considerations," *NDT E Int.*, vol. 42, no. 8, pp. 713–720, 2009, doi: 10.1016/j.ndteint.2009.06.005.

[84] H. Ding, Y. T. He, and S. B. Jiao, "Rosette eddy current sensor for structural health monitoring," in *Applied Mechanics and Materials*, 2013, pp. 430–436. doi: 10.4028/www.scientific.net/AMM.330.430.

[85] R. Xie *et al.*, "Fatigue crack length sizing using a novel flexible eddy current sensor array," *Sensors (Switzerland)*, vol. 15, no. 12, pp. 32138–32151, 2015, doi: 10.3390/s151229911.

[86] S. Jiao, L. Cheng, X. Li, P. Li, and H. Ding, "Monitoring fatigue cracks of a metal structure using an eddy current sensor," *Eurasip J. Wirel. Commun. Netw.*, vol. 2016, no. 1, 2016, doi: 10.1186/s13638-016-0689-y.

[87] T. Chen, Y. He, and J. Du, "A high-sensitivity flexible eddy current array sensor for crack monitoring of welded structures under varying environment," *Sensors (Switzerland)*, vol. 18, no. 6, 2018, doi: 10.3390/s18061780.

[88] G. Chen, W. Zhang, Z. Zhang, X. Jin, and W. Pang, "A new rosette-like eddy current array sensor with high sensitivity for fatigue defect around bolt hole in SHM," *NDT E Int.*, vol. 94, Dec. 2017, doi: 10.1016/j.ndteint.2017.12.001.

[89] H. Sun, T. Wang, D. Lin, Y. Wang, and X. Qing, "An eddy current-based structural health monitoring technique for tracking bolt cracking," *Sensors (Switzerland)*, vol. 20, no. 23, pp. 1–14, 2020, doi: 10.3390/s20236843.

[90] Y. Song, T. Chen, R. Cui, Y. He, X. Fan, and B. Ma, "The durability of flexible eddy current array (FECA) sensors in harsh service environments," *Sci. Rep.*, vol. 11, no. 1, pp. 1–14, 2021, doi: 10.1038/s41598-021-89750-y.

[91] L. S. Rosado, T. G. Santos, M. Piedade, P. M. Ramos, and P. Vilaça, "Advanced technique for non-destructive testing of friction stir welding of metals," *Meas. J. Int. Meas. Confed.*, vol. 43, no. 8, pp. 1021–1030, 2010, doi: 10.1016/j.measurement.2010.02.006.

[92] N. Goldfine, D. Schlicker, Y. Sheiretov, A. Washabaugh, V. Zilberstein, and D. Grundy, "Surface mounted and scanning periodic field eddy-current sensors for structural health monitoring," *IEEE Aerosp. Conf. Proc.*, vol. 6, no. February, pp. 3141–3152, 2002, doi: 10.1109/AERO.2002.1036155.

[93] N. Goldfine, D. C. Grundy, V. A. Zilberstein, D. G. Kinchen, and A. A. Mccool, "Friction Stir Weld Inspection Through Conductivity Imaging Using Shaped Field MWM(TM)-Arrays," 2002. [Online]. Available: https://api.semanticscholar.org/CorpusID:136637633

[94] N. Goldfine, V. Zilberstein, D. Schlicker, and D. Grundy, " Eddy-Current in situ Sensors for SHM ," *Encycl. Struct. Heal. Monit.*, no. i, pp. 1–14, 2008, doi: 10.1002/9780470061626.shm080.

[95] M. Lemistre, D. Placko, and D. Balageas, *HELP Layer for electromagnetic SHM of CFRP*. 2004.
[96] C. Paget, H. Speckmann, T. Krichel, and F. Eichelbaum, “Validation of SHM Sensors in Airbus A380 Full-Scale Fatigue Test,” *Encycl. Struct. Heal. Monit.*, pp. 1–10, 2008, doi: 10.1002/9780470061626.shm149.
[97] M. Hansen, “A Cooler Weld,” *Mech. Eng.*, vol. 125, no. 03, pp. D10–D16, Mar. 2003, doi: 10.1115/1.2003-MAR-3.
[98] B. Kwon, H. Choe, J. Jeong, H. Ju, J. H. Kweon, and Y. W. Nam, “Static and fatigue behavior of induction-welded single lap carbon fiber reinforced polyetherketoneketone thermoplastic composite joints,” *J. Compos. Mater.*, vol. 55, no. 28, pp. 4183–4193, 2021, doi: 10.1177/00219983211033891.
[99] A. P. Mouritz, *Introduction to aerospace material*. Woodhead Publishing, 2012.
[100] B. Choudhury and M. Chandrasekaran, “Investigation on welding characteristics of aerospace materials - A review,” *Mater. Today Proc.*, vol. 4, no. 8, pp. 7519–7526, 2017, doi: 10.1016/j.matpr.2017.07.083.
[101] G. Çam and S. Mistikoglu, “Recent developments in friction stir welding of al-Alloys,” *J. Mater. Eng. Perform.*, vol. 23, no. 6, pp. 1936–1953, 2014, doi: 10.1007/s11665-014-0968-x.
[102] A. Mishra and S. B. Dutta, “Detection of surface defects in friction stir welded joints by using a novel machine learning approach,” *Appl. Eng. Lett.*, vol. 5, no. 1, pp. 16–21, 2020, doi: 10.18485/aeletters.2020.5.1.3.
[103] Q. Zhao *et al.*, “High-strength titanium alloys for aerospace engineering applications: A review on melting-forging process,” *Mater. Sci. Eng. A*, vol. 845, no. May, p. 143260, 2022, doi: 10.1016/j.msea.2022.143260.
[104] A. Baker, D. SE, and D. Kelly, *Composite Materials for Aircraft Structures*. 2004.
[105] X. Zhang, Y. Chen, and J. Hu, “Recent advances in the development of aerospace materials,” *Prog. Aerosp. Sci.*, vol. 97, no. August 2017, pp. 22–34, 2018, doi: 10.1016/j.paerosci.2018.01.001.
[106] A. S. Warren, “Developments and challenges for aluminum - A boeing perspective,” *Mater. Forum*, vol. 28, pp. 24–31, 2004.
[107] T. Dursun and C. Soutis, “Recent developments in advanced aircraft aluminium alloys,” *Mater. Des.*, vol. 56, pp. 862–871, 2014, doi: 10.1016/j.matdes.2013.12.002.
[108] GMI Global Market Insights, “Expoxy Composite Market Size,” 2024. [Online]. Available: https://www.gminsights.com/industry-analysis/epoxy-composite-market
[109] S. W. Kallee, “5 - Industrial applications of friction stir welding,” in *Woodhead Publishing Series in Welding and Other Joining Technologies*, D. Lohwasser and Z. B. T.-F. S. W. Chen, Eds., Woodhead Publishing, 2010, pp. 118–163. doi: https://doi.org/10.1533/9781845697716.1.118.
[110] D. M. Sekban, S. M. Aktarer, and G. Purcek, “Friction Stir Welding of Low-Carbon Shipbuilding Steel Plates: Microstructure, Mechanical Properties, and Corrosion Behavior,” *Metall. Mater. Trans. A Phys. Metall. Mater. Sci.*, vol. 50, no. 9, pp. 4127–4140, 2019, doi: 10.1007/s11661-019-05324-8.
[111] T. Kawasaki, T. Makino, K. Masai, H. Ohba, Y. Ina, and M. Ezumi, “Application of friction stir welding to construction of railway vehicles,” *JSME Int. Journal, Ser. A Solid Mech. Mater. Eng.*, vol. 47, no. 3, pp. 502–511, 2004, doi: 10.1299/jsmea.47.502.
[112] S. Verma, M. Gupta, and J. P. Misra, “Friction Stir Welding of Aerospace

Materials: a State of Art Review," pp. 135–150, 2016, doi: 10.2507/daaam.scibook.2016.13.

[113] M. (Grenzebach M. G. Weigl, "Friction stir welding processes and welding technology." https://www.grenzebach.com/en-us/markets/friction-stir-welding/welding-technology-process/

[114] Jeroen De Backer, Sam Wei, and Jonathan Martin, "Robotic FSW for three-dimensional components," *SEEIIW2015 Rom.*, no. June, 2015.

[115] J. Kumar, G. Kumar, H. Mehdi, and M. Kumar, "Optimization of FSW parameters on mechanical properties of different aluminum alloys of AA6082 and AA7050 by response surface methodology," *Int. J. Interact. Des. Manuf.*, 2023, doi: 10.1007/s12008-023-01425-2.

[116] N. Kashaev, V. Ventzke, and G. Çam, "Prospects of laser beam welding and friction stir welding processes for aluminum airframe structural applications," *J. Manuf. Process.*, vol. 36, no. November, pp. 571–600, 2018, doi: 10.1016/j.jmapro.2018.10.005.

[117] "https://www.flyingmag.com/aircraft-jets-eclipse-jet-granted-double-service-life/." https://www.flyingmag.com/aircraft-jets-eclipse-jet-granted-double-service-life/%0A

[118] "https://www.esa.int/ESA_Multimedia/Images/2018/12/Hydrogen_tank_for_Ariane_6_upper_stage."

[119] "https://www.cncmachinery.com.my/index.php?ws=latestnews&nid=79975&gid=2874&lang=en".

[120] "https://www.shapesbyhydro.com/en/manufacturing/how-you-can-use-friction-stir-welded-aluminium-panels-for-your-shipbuilding-project/".

[121] S. P. Meyer, B. Jaeger, C. Wunderling, and M. F. Zaeh, "Friction stir welding of glass fiber-reinforced polyamide 6: Analysis of the tensile strength and fiber length distribution of friction stir welded PA6-GF30," *IOP Conf. Ser. Mater. Sci. Eng.*, vol. 480, no. 1, 2019, doi: 10.1088/1757-899X/480/1/012013.

[122] S. Eslami, F. A. T. Vilhena, A. T. Marques, and P. M. G. P. Moreira, "New technological solution for friction stir welding of composites," *Procedia Struct. Integr.*, vol. 28, no. January, pp. 659–666, 2020, doi: 10.1016/j.prostr.2020.10.076.

[123] S. Kumar, J. D. Jafrey Daniel, and B. S. Roy, "Friction stir welding of glass filled Nylon 6 composite sheets using double step shoulder tool," *Mater. Today Proc.*, vol. 44, pp. 2511–2516, 2021, doi: 10.1016/j.matpr.2020.12.600.

[124] M. Y. Ishraq, S. Maqsood, K. Naeem, M. Abid, and M. Omair, "Analysing significant process parameters for friction stir welding of polymer composite," *Int. J. Adv. Manuf. Technol.*, vol. 105, no. 12, pp. 4973–4987, 2019, doi: 10.1007/s00170-019-04548-7.

[125] S. Kumar, T. Medhi, and B. S. Roy, *Friction stir welding of thermoplastic composites*, no. January. Springer Singapore, 2019. doi: 10.1007/978-981-13-6412-9_21.

[126] A. Yousefpour, M. Hojjati, and J. P. Immarigeon, "Fusion bonding/welding of thermoplastic composites," *Journal of Thermoplastic Composite Materials*, vol. 17, no. 4. pp. 303–341, 2004. doi: 10.1177/0892705704045187.

[127] D. Brassard, M. Dubé, and J. R. Tavares, "Resistance welding of thermoplastic composites with a nanocomposite heating element," *Compos. Part B Eng.*, vol. 165, pp. 779–784, 2019, doi: 10.1016/j.compositesb.2019.02.038.

[128] T. G. Unnikrishnan and P. Kavan, “A review study in ultrasonic-welding of similar and dissimilar thermoplastic polymers and its composites,” *Mater. Today Proc.*, vol. 56, pp. 3294–3300, 2022, doi: 10.1016/j.matpr.2021.09.540.
[129] T. J. Ahmed, D. Stavrov, H. E. N. Bersee, and A. Beukers, “Induction welding of thermoplastic composites-an overview,” *Compos. Part A Appl. Sci. Manuf.*, vol. 37, no. 10, pp. 1638–1651, 2006, doi: 10.1016/j.compositesa.2005.10.009.
[130] OrbitsHub, “Exterior Design and Aerodynamics: Gulfstream G280.” https://orbitshub.com/exterior-design-and-aerodynamics-gulfstream-g280/
[131] V. Ingen, V. Wijngaarden, and S. Iii, “Development of the Gulfstream G650 induction welded thermoplastic elevators and rudder.” 2010. [Online]. Available: https://www.researchgate.net/publication/332403057
[132] AirCharter, “Dassault Falcon 5X Specifications and Charter Info.” https://www.aircharter.com/falcon-5x-charter-info/
[133] NASA, “Boeing’s Phantom Eye ISR Technology Demonstrator.” https://www.nasa.gov/image-detail/boeings-phantom-eye-isr-technology-demonstrator-5/
[134] A. Pouliezos and G. Stavrakakis, *Real Time Fault Monitoring of Industrial Processes*. 1994. doi: 10.1007/978-94-015-8300-8.
[135] J. Antony *et al.*, “Benefits, challenges, critical success factors and motivations of Quality 4.0 – A qualitative global study,” *Total Qual. Manag. Bus. Excell.*, vol. 34, no. 7–8, pp. 827–846, May 2023, doi: 10.1080/14783363.2022.2113737.
[136] H. Rocha and C. Semprimoschnig, “Sensors for process and structural health monitoring of aerospace composites : A review,” vol. 237, no. January, 2021, doi: 10.1016/j.engstruct.2021.112231.
[137] Y. Javadi *et al.*, “In-process calibration of a non-destructive testing system used for in-process inspection of multi-pass welding,” *Mater. Des.*, vol. 195, p. 108981, 2020, doi: 10.1016/j.matdes.2020.108981.
[138] P. Sinha, S. Muthukumaran, R. Sivakumar, and S. K. Mukherjee, “Condition monitoring of first mode of metal transfer in friction stir welding by image processing techniques,” *Int. J. Adv. Manuf. Technol.*, vol. 36, no. 5–6, pp. 484–489, 2008, doi: 10.1007/s00170-006-0854-2.
[139] R. R. R.Rajashekar, “Digital Image Processing Of Friction Stir Weld Bead Surface Using Profiling and Contouring For Weld Quality Assessment,” *IOSR J. Mech. Civ. Eng.*, vol. 5, no. 5, pp. 54–64, 2013, doi: 10.9790/1684-0555464.
[140] N. N. Bhat, K. Kumari, S. Dutta, S. K. Pal, and S. Pal, “Friction stir weld classification by applying wavelet analysis and support vector machine on weld surface images,” *J. Manuf. Process.*, vol. 20, pp. 274–281, 2015, doi: 10.1016/j.jmapro.2015.07.002.
[141] R. Ranjan *et al.*, “Classification and identification of surface defects in friction stir welding: An image processing approach,” *J. Manuf. Process.*, vol. 22, pp. 237–253, 2016, doi: 10.1016/j.jmapro.2016.03.009.
[142] V. Soundararajan, H. Atharifar, and R. Kovacevic, “Monitorinf and processing the acoustic emission signals from the friction-stir-welding process,” *Proc. Inst. Mech. Eng. Part B J. Eng. Manuf.*, vol. 220, no. 10, pp. 1673–1685, 2006, doi: 10.1243/09544054JEM586.
[143] D. Kleiner and C. R. Bird, “Signal processing for quality assurance in friction stir welds,” *Insight Non-Destructive Test. Cond. Monit.*, vol. 46, no. 2, pp. 85–87, 2004, doi: 10.1784/insi.46.2.85.55545.
[144] V. Richter-Trummer *et al.*, “Fibre Bragg grating sensors for monitoring the metal inert gas and friction stir welding processes,” *Meas. Sci. Technol.*, vol. 21, no. 8,

2010, doi: 10.1088/0957-0233/21/8/085105.
[145] T. Bento, R. Maciel, D. F. O. Braga, L. da Silva, P. M. G. P. Moreira, and V. Infante, “Self-sensing FS weld-bonded joints for structural monitoring,” *Procedia Struct. Integr.*, vol. 25, no. 2019, pp. 234–245, 2020, doi: 10.1016/j.prostr.2020.04.028.
[146] Hunt, Johnathon, Larsen, Brigham, and Hovanski, Yuri, “In Line Nondestructive Testing for Sheet Metal Friction Stir Welding,” in *WCX SAE World Congress Experience*, SAE International, 2023. doi: https://doi.org/10.4271/2023-01-0069.
[147] F. Flora, M. Boccaccio, G. P. Malfense Fierro, and M. Meo, *Non-destructive thermography-based system for damage localisation and characterisation during induction welding of thermoplastic composites*. 2020. doi: 10.1117/12.2564925.
[148] F. Flora, M. Boccaccio, G. P. M. Fierro, and M. Meo, “Real-time thermography system for composite welding: Undamaged baseline approach,” *Compos. Part B Eng.*, vol. 215, no. November 2020, p. 108740, 2021, doi: 10.1016/j.compositesb.2021.108740.
[149] N. A. A. Rahim, J. Pandher, N. Coppola, V. Penumetsa, and M. van Tooren, “In-situ monitoring and control of induction welding in thermoplastic composites using high definition fiber optic sensors,” *CAMX 2019 - Compos. Adv. Mater. Expo*, 2019, doi: 10.33599/nasampe/c.19.0668.
[150] C. Chen, R. Kovacevic, and D. Jandgric, “Wavelet transform analysis of acoustic emission in monitoring friction stir welding of 6061 aluminum,” *Int. J. Mach. Tools Manuf.*, vol. 43, no. 13, pp. 1383–1390, 2003, doi: 10.1016/S0890-6955(03)00130-5.
[151] E. Jiménez-Macías, A. Sánchez-Roca, H. Carvajal-Fals, J. Blanco-Fernández, and E. Martínez-Cámara, “Wavelets application in prediction of friction stir welding parameters of alloy joints from vibroacoustic ANN-based model,” *Abstr. Appl. Anal.*, vol. 2014, 2014, doi: 10.1155/2014/728564.
[152] J. B. Fernández, A. S. Roca, H. C. Fals, E. J. Macías, and M. P. de la Parte, “Application of vibroacoustic signals to evaluate tools profile changes in friction stir welding on AA 1050 H24 alloy,” *Sci. Technol. Weld. Join.*, vol. 17, no. 6, pp. 501–510, 2012, doi: 10.1179/1362171812Y.0000000040.
[153] S. Subramaniam, S. Narayanan, and A. S. Denis, “Acoustic emission-based monitoring approach for friction stir welding of aluminum alloy AA6063-T6 with different tool pin profiles,” *Proc. Inst. Mech. Eng. Part B J. Eng. Manuf.*, vol. 227, no. 3, pp. 407–416, 2013, doi: 10.1177/0954405412472673.
[154] S. Kannaiyan, S. Murugesan, D. Thirumalaikannan, B. Visvalingam, and B. P. Nagasai, “Characteristics analysis and monitoring of friction stir welded dissimilar AA5083/AA6061-T6 using acoustic emission technique,” *Weld. Int.*, vol. 38, no. 8, pp. 556–573, Aug. 2024, doi: 10.1080/09507116.2024.2376187.
[155] U. Kumar *et al.*, “Defect identification in friction stir welding using discrete wavelet analysis,” *Adv. Eng. Softw.*, vol. 85, pp. 43–50, 2015, doi: 10.1016/j.advengsoft.2015.02.001.
[156] S. Kumari *et al.*, “Defect identification in friction stir welding using continuous wavelet transform,” *J. Intell. Manuf.*, vol. 30, no. 2, pp. 483–494, 2019, doi: 10.1007/s10845-016-1259-1.
[157] P. Fleming *et al.*, “In-process gap detection in friction stir welding,” *Sens. Rev.*, vol. 28, no. 1, pp. 62–67, 2008, doi: 10.1108/02602280810850044.
[158] E. Boldsaikhan, E. M. Corwin, A. M. Logar, and W. J. Arbegast, “The use of neural network and discrete Fourier transform for real-time evaluation of friction stir welding,” *Appl. Soft Comput. J.*, vol. 11, no. 8, pp. 4839–4846, 2011, doi:

10.1016/j.asoc.2011.06.017.
[159] T. Jene, G. Dobmann, G. Wagner, and D. Eifler, “Monitoring of the friction stir welding process to describe parameter effects on joint quality,” *Weld. World*, vol. 52, no. 9–10, pp. 47–53, 2008, doi: 10.1007/BF03266668.
[160] B. Das, S. Pal, and B. Swarup, “Monitoring of Friction Stir Welding Process Through Signals Acquired During the Welding,” *Des. Res. Conf. (AIMTDR 2014)*, no. Aimtdr, pp. 1–7, 2014.
[161] B. Das, S. Pal, and S. Bag, “Weld quality prediction in friction stir welding using wavelet analysis,” *Int. J. Adv. Manuf. Technol.*, vol. 89, no. 1–4, pp. 711–725, 2017, doi: 10.1007/s00170-016-9140-0.
[162] T. Stanley, “Research Paper,” *10 Performance-Based Proj. Math Classr.*, pp. 115–126, 2022, doi: 10.4324/9781003232490-9.
[163] A. Güemes, A. Fernandez-Lopez, A. R. Pozo, and J. Sierra-Pérez, “Structural health monitoring for advanced composite structures: A review,” *Journal of Composites Science*, vol. 4, no. 1. MDPI AG, 2020. doi: 10.3390/jcs4010013.
[164] J. Sierra-Pérez, “Smart aeronautical structures development and experimental validation of a Structural Health Monitoring system for damage detection,” 2014. [Online]. Available: http://oa.upm.es/30438/
[165] C. Kralovec and M. Schagerl, “Review of structural health monitoring methods regarding a multi-sensor approach for damage assessment of metal and composite structures,” *Sensors (Switzerland)*, vol. 20, no. 3, pp. 1–25, 2020, doi: 10.3390/s20030826.
[166] D. E. Bently, C. T. Hatch, and B. Grissom, *Fundamentals of Rotating Machinery Diagnostics*. ASME Press, 2002. doi: 10.1115/1.801FRM.
[167] Q. Deng, B. F. Santos, and W. J. C. Verhagen, “A novel decision support system for optimizing aircraft maintenance check schedule and task allocation,” *Decis. Support Syst.*, vol. 146, no. September 2020, p. 113545, 2021, doi: 10.1016/j.dss.2021.113545.
[168] S. P. Ackert, “Evaluation & Insights of Commercial Aircraft Maintenance Programs,” *Basics Aircr. Maint. Programs Financ.*, pp. 1–23, 2010.
[169] W. J. C. Verhagen *et al.*, “Condition-Based Maintenance in Aviation: Challenges and Opportunities,” *Aerospace*, vol. 10, no. 9, pp. 1–23, 2023, doi: 10.3390/aerospace10090762.
[170] J. W. Xiang, Z. B. Yang, and J. L. Aguilar, “Structural health monitoring for mechanical structures using multi-sensor data,” *Int. J. Distrib. Sens. Networks*, vol. 14, no. 9, pp. 30–32, 2018, doi: 10.1177/1550147718802019.
[171] S. S. Saidin, A. Jamadin, S. Abdul Kudus, N. Mohd Amin, and M. A. Anuar, “An Overview: The Application of Vibration-Based Techniques in Bridge Structural Health Monitoring,” *Int. J. Concr. Struct. Mater.*, vol. 16, no. 1, pp. 1–17, 2022, doi: 10.1186/s40069-022-00557-1.
[172] B. Glisic, “Concise Historic Overview of Strain Sensors Used in the Monitoring of Civil Structures: The First One Hundred Years,” *Sensors*, vol. 22, no. 6, 2022, doi: 10.3390/s22062397.
[173] L. Capineri and A. Bulletti, “Ultrasonic guided-waves sensors and integrated structural health monitoring systems for impact detection and localization: A review,” *Sensors*, vol. 21, no. 9, 2021, doi: 10.3390/s21092929.
[174] V. Giurgiutiu, “Tuned Lamb wave excitation and detection with piezoelectric wafer active sensors for structural health monitoring,” *J. Intell. Mater. Syst. Struct.*, vol. 16, no. 4, pp. 291–305, 2005, doi: 10.1177/1045389X05050106.
[175] T. Singh and S. Sehgal, “Structural Health Monitoring of Composite Materials,”

Arch. Comput. Methods Eng., vol. 29, no. 4, pp. 1997–2017, 2022, doi: 10.1007/s11831-021-09666-8.

[176] D. D. L. Chung, "A review of multifunctional polymer-matrix structural composites," *Compos. Part B Eng.*, vol. 160, no. November 2018, pp. 644–660, 2019, doi: 10.1016/j.compositesb.2018.12.117.

[177] P. Gao, C. Wang, Y. Li, and Z. Cong, "Electromagnetic and eddy current NDT in weld inspection: A review," *Insight Non-Destructive Test. Cond. Monit.*, vol. 57, no. 6, pp. 337–345, 2015, doi: 10.1784/insi.2015.57.6.337.

[178] H. Miao and F. Li, "Shear horizontal wave transducers for structural health monitoring and nondestructive testing: A review," *Ultrasonics*, vol. 114, no. January, p. 106355, 2021, doi: 10.1016/j.ultras.2021.106355.

[179] C. R. Farrar, S. W. Doebling, and D. A. Nix, "Vibration-based structural damage identification," *Philos. Trans. R. Soc. A Math. Phys. Eng. Sci.*, vol. 359, no. 1778, pp. 131–149, 2001, doi: 10.1098/rsta.2000.0717.

[180] D. Montalvão, N. M. M. Maia, and A. M. R. Ribeiro, "A review of vibration-based structural health monitoring with special emphasis on composite materials," *Shock Vib. Dig.*, vol. 38, no. 4, pp. 295–324, 2006, doi: 10.1177/0583102406065898.

[181] J. M. Castillo-Mingorance, M. Sol-Sánchez, F. Moreno-Navarro, and M. C. Rubio-Gámez, "A critical review of sensors for the continuous monitoring of smart and sustainable railway infrastructures," *Sustain.*, vol. 12, no. 22, pp. 1–20, 2020, doi: 10.3390/su12229428.

[182] A. Zitoun *et al.*, "Graphene-based strain sensing in composites for structural and health monitoring applications," *SN Appl. Sci.*, vol. 4, no. 2, 2022, doi: 10.1007/s42452-022-04940-1.

[183] M. Mitra and S. Gopalakrishnan, "Guided wave based structural health monitoring: A review," *Smart Mater. Struct.*, vol. 25, no. 5, 2016, doi: 10.1088/0964-1726/25/5/053001.

[184] M. Philibert, K. Yao, M. Gresil, and C. Soutis, "Lamb waves-based technologies for structural health monitoring of composite structures for aircraft applications," *Eur. J. Mater.*, vol. 2, no. 1, pp. 436–474, 2022, doi: 10.1080/26889277.2022.2094839.

[185] Z. Yang *et al.*, "A review in guided-ultrasonic-wave-based structural health monitoring: From fundamental theory to machine learning techniques," *Ultrasonics*, vol. 133, no. April, p. 107014, 2023, doi: 10.1016/j.ultras.2023.107014.

[186] V. T. Rathod, "A review of acoustic impedance matching techniques for piezoelectric sensors and transducers," *Sensors (Switzerland)*, vol. 20, no. 14, pp. 1–65, 2020, doi: 10.3390/s20144051.

[187] C. Muir *et al.*, "Damage mechanism identification in composites via machine learning and acoustic emission," *npj Comput. Mater.*, vol. 7, no. 1, pp. 1–15, 2021, doi: 10.1038/s41524-021-00565-x.

[188] A. J. Brunner, "Structural health and condition monitoring with acoustic emission and guided ultrasonic waves: What about long-term durability of sensors, sensor coupling and measurement chain?," *Appl. Sci.*, vol. 11, no. 24, 2021, doi: 10.3390/app112411648.

[189] F. Yan, R. L. Royer, and J. L. Rose, "Ultrasonic guided wave imaging techniques in structural health monitoring," *J. Intell. Mater. Syst. Struct.*, vol. 21, no. 3, pp. 377–384, 2010, doi: 10.1177/1045389X09356026.

[190] Q. Yuan, Y. Wang, Z. Su, and T. Zhang, "Quantitative damage evaluation of

curved plates based on phased array guided wave and deep learning algorithm," *Ultrasonics*, vol. 137, no. September 2023, p. 107176, 2024, doi: 10.1016/j.ultras.2023.107176.

[191] D. Roach, T. Lynch-Staunton, B. Shaigec, and D. Formosa, "Assessing the Performance CVM Sensors for Monitoring the 737 Aft Pressure Bulkhead," in *Structural Health Monitoring 2023: Designing SHM for Sustainability, Maintainability, and Reliability - Proceedings of the 14th International Workshop on Structural Health Monitoring*, 2023, pp. 835–842. [Online]. Available: https://www.scopus.com/inward/record.uri?eid=2-s2.0-85182267248&partnerID=40&md5=c28aab7b05dde86d598d375176c4bb05

[192] M. Wang, N. Li, G. D. Wang, S. W. Lu, Q. Di Zhao, and X. L. Liu, "High-sensitive flexural sensors for health monitoring of composite materials using embedded carbon nanotube (CNT) buckypaper," *Compos. Struct.*, vol. 261, no. March 2020, p. 113280, 2021, doi: 10.1016/j.compstruct.2020.113280.

[193] M. Lemistre, "Low Frequency Electromagnetic Techniques," *Structural Health Monitoring*. Wiley-ISTE, pp. 411–461, 2010. doi: 10.1002/9780470612071.ch6.

[194] L. Parida and S. Moharana, "A comprehensive review on piezo impedance based multi sensing technique," *Results Eng.*, vol. 18, no. April, p. 101093, 2023, doi: 10.1016/j.rineng.2023.101093.

[195] W. S. Na and J. Baek, "A review of the piezoelectric electromechanical impedance based structural health monitoring technique for engineering structures," *Sensors (Switzerland)*, vol. 18, no. 5, 2018, doi: 10.3390/s18051307.

[196] A. F. G. Tenreiro, A. M. Lopes, and L. F. M. da Silva, "A review of structural health monitoring of bonded structures using electromechanical impedance spectroscopy," *Struct. Heal. Monit.*, vol. 21, no. 2, pp. 228–249, 2022, doi: 10.1177/1475921721993419.

[197] W. Roth and V. Giurgiutiu, "Structural health monitoring of an adhesive disbond through electromechanical impedance spectroscopy," *Int. J. Adhes. Adhes.*, vol. 73, no. November 2016, pp. 109–117, 2017, doi: 10.1016/j.ijadhadh.2016.11.008.

[198] M. A. Fakih, S. Mustapha, J. Tarraf, G. Ayoub, and R. Hamade, "Detection and assessment of flaws in friction stir welded metallic plates," vol. 10168, p. 88, 2017, doi: 10.1117/12.2258701.

[199] M. A. Fakih, S. Mustapha, J. Tarraf, G. Ayoub, and R. Hamade, "Detection and assessment of flaws in friction stir welded joints using ultrasonic guided waves: experimental and finite element analysis," *Mech. Syst. Signal Process.*, vol. 101, pp. 516–534, 2018, doi: 10.1016/j.ymssp.2017.09.003.

[200] A. Sorrentino, A. Chiariello, L. Di Palma, and A. de Fenza, "Experimental investigation of damage detection on structures with friction stir welding (FSW) junctions," *IOP Conf. Ser. Mater. Sci. Eng.*, vol. 1024, no. 1, 2021, doi: 10.1088/1757-899X/1024/1/012031.

[201] G. Gautam, M. K. Mehta, D. M. Joglekar, and D. K. Dwivedi, "Lamb Wave-based Non-destructive Evaluation in Thin Section Lap Joint of Friction Stir Welding BT - Advances in Non-Destructive Evaluation," B. Ghose, R. Mulaveesala, and P. Mylavarapu, Eds., Singapore: Springer Nature Singapore, 2024, pp. 133–142.

[202] X. Liu *et al.*, "Elastic-plastic deformation and organization analysis for Al 7075 friction stir welding joints based on MXene/SWCNT sensor," *Sensors Actuators A Phys.*, vol. 352, no. November 2022, p. 114203, 2023, doi: 10.1016/j.sna.2023.114203.

[203] P. M. Ferreira *et al.*, “Self-sensing metallic material based on PZT particles produced by friction stir processing envisaging structural health monitoring applications,” *Mater. Charact.*, vol. 205, no. September, p. 113371, 2023, doi: 10.1016/j.matchar.2023.113371.
[204] P. M. Ferreira, M. A. Machado, M. S. Carvalho, and C. Vidal, “Granting Sensorial Properties to Metal Parts through Friction Stir Processing,” *Meas. J. Int. Meas. Confed.*, vol. 207, no. December 2022, p. 112405, 2023, doi: 10.1016/j.measurement.2022.112405.
[205] P. M. Ferreira *et al.*, “Enabling electrical response through piezoelectric particle integration in AA2017-T451 aluminium parts using FSP technology,” *Smart Mater. Struct.*, vol. 33, no. 6, 2024, doi: 10.1088/1361-665X/ad4d45.
[206] O. G. Kravchenko, V. S. Bonab, and I. Manas-Zloczower, “Spray-Assisted Microwave Welding of Thermoplastics Using Carbon Nanostructures with Enabled Health Monitoring,” *Polym. Eng. Sci.*, vol. 59, no. 11, pp. 2247–2254, 2019, doi: 10.1002/pen.25227.
[207] H. Frederick, W. Li, W. Sands, E. Tsai, and G. Palardy, “Multifunctional Films for Fusion Bonding and Structural Health Monitoring of Thermoplastic Composite Joints,” 2020.
[208] W. Li, H. Frederick, and G. Palardy, “Multifunctional films for thermoplastic composite joints: Ultrasonic welding and damage detection under tension loading,” *Compos. Part A Appl. Sci. Manuf.*, vol. 141, no. October 2020, p. 106221, 2021, doi: 10.1016/j.compositesa.2020.106221.
[209] W. Li and G. Palardy, “Electro-Mechanical Response of Ultrasonically Welded Thermoplastic Composite Interfaces under Static and Cyclic Flexural Loads Using Nanocomposites,” *ACS Appl. Polym. Mater.*, vol. 4, no. 7, pp. 5209–5223, 2022, doi: 10.1021/acsapm.2c00737.
[210] W. Li and G. Palardy, “Tensile behavior of repaired thermoplastic composite joints through ultrasonic welding,” in *International SAMPE Technical Conference*, 2023. doi: 10.33599/nasampe/s.23.0009.
[211] P. Ochôa, I. F. Villegas, R. M. Groves, and R. Benedictus, “Diagnostic of manufacturing defects in ultrasonically welded thermoplastic composite joints using ultrasonic guided waves,” *NDT E Int.*, vol. 107, 2019, doi: 10.1016/j.ndteint.2019.102126.
[212] H. Wang, B. Ju, W. Li, and Z. Feng, “Ultrastable eddy current displacement sensor working in harsh temperature environments with comprehensive self-temperature compensation,” *Sensors Actuators, A Phys.*, vol. 211, pp. 98–104, 2014, doi: 10.1016/j.sna.2014.03.008.
[213] H. Wang and Z. Feng, “Ultrastable and highly sensitive eddy current displacement sensor using self-temperature compensation,” *Sensors Actuators, A Phys.*, vol. 203, pp. 362–368, 2013, doi: 10.1016/j.sna.2013.09.016.
[214] Y. Zheng, J. Wu, and Y. Yang, “Temperature compensation of eddy current sensor based on temperature-voltage model,” *Proc. World Congr. Intell. Control Autom.*, vol. 2016-Septe, pp. 438–441, 2016, doi: 10.1109/WCICA.2016.7578616.
[215] B. Lei, P. Yi, Y. Li, and J. Xiang, “A temperature drift compensation method for pulsed eddy current technology,” *Sensors (Switzerland)*, vol. 18, no. 6, 2018, doi: 10.3390/s18061952.
[216] R. Nandan, T. DebRoy, and H. K. D. H. Bhadeshia, “Recent advances in friction-stir welding - Process, weldment structure and properties,” *Prog. Mater. Sci.*, vol. 53, no. 6, pp. 980–1023, 2008, doi: 10.1016/j.pmatsci.2008.05.001.

[217] P. L. Threadgilll, A. J. Leonard, H. R. Shercliff, and P. J. Withers, “Friction stir welding of aluminium alloys,” *Int. Mater. Rev.*, vol. 54, no. 2, pp. 49–93, 2009, doi: 10.1179/174328009X411136.
[218] P. Podržaj, B. Jerman, and D. Klobčar, “Welding defects at friction stir welding,” *Metalurgija*, vol. 54, no. 2, pp. 387–389, 2015.
[219] R. Lazzeri, “A comparison between safe life, damage tolerance and probabilistic approaches to aircraft structure fatigue design,” *Aerotecnica Missili e Spazio*, vol. 81, no. 2. 2002. [Online]. Available: https://www.researchgate.net/publication/267563386
[220] I. De Baere, K. Allaer, W. Van Paepegem, and J. Degrieck, “Fatigue behaviour of infrared welded joints in fibre reinforced thermoplastics,” in *Durability of Composite Systems (Duracosys-2012)*, 2012.
[221] I. De Baere, W. Van Paepegem, and J. Degrieck, “The in-plane shear behaviour of a carbon fabric reinforced thermoplastic under quasi-static and fatigue loading conditions,” *Fiber-Reinforced Compos.*, pp. 159–216, 2012.
[222] J. D. Jackson and R. F. Fox, “ Classical Electrodynamics, 3rd ed . ,” *American Journal of Physics*, vol. 67, no. 9. pp. 841–842, 1999. doi: 10.1119/1.19136.
[223] A. Todoroki, “Skin effect of alternating electric current on laminated CFRP,” *Adv. Compos. Mater.*, vol. 21, no. 5–6, pp. 477–489, 2012, doi: 10.1080/09243046.2012.743716.
[224] C. V. Dodd and W. E. Deeds, “Analytical solutions to eddy-current probe-coil problems,” *J. Appl. Phys.*, vol. 39, no. 6, pp. 2829–2838, 1968, doi: 10.1063/1.1656680.
[225] Y. Bai, X. Zhang, L. Jiang, and C. Tang, “3-D eddy currents analysis in orthotropic materials using truncated region eigenfunction expansion method,” *Appl. Mech. Mater.*, vol. 239–240, pp. 258–263, 2013, doi: 10.4028/www.scientific.net/AMM.239-240.258.
[226] K. Mizukami, Y. Mizutani, A. Todoroki, and Y. Suzuki, “Analytical solutions to eddy current in carbon fiber-reinforced composites induced by line current,” *Adv. Compos. Mater.*, vol. 25, no. 4, pp. 385–401, 2016, doi: 10.1080/09243046.2015.1052132.
[227] S. Sharma, “Application of finite element models to eddy current probe design for aircraft inspection,” Iowa State University, 1998.
[228] N. Angelidis, “Damage sensing in CFRP composites using electrical potential techniques,” Cranfield University, 2004.
[229] J. Cheng, H. Ji, J. Qiu, T. Takagi, T. Uchimoto, and N. Hu, “Role of interlaminar interface on bulk conductivity and electrical anisotropy of CFRP laminates measured by eddy current method,” *NDT E Int.*, vol. 68, pp. 1–12, 2014, doi: https://doi.org/10.1016/j.ndteint.2014.07.001.
[230] G. L. Sorger *et al.*, “Non-destructive microstructural analysis by electrical conductivity: Comparison with hardness measurements in different materials,” *J. Mater. Sci. Technol.*, vol. 35, no. 3, pp. 360–368, 2019, doi: 10.1016/j.jmst.2018.09.047.
[231] L. CUI *et al.*, “Precipitation of metastable phases and its effect on electrical resistivity of Al-0.96Mg2Si alloy during aging,” *Trans. Nonferrous Met. Soc. China*, vol. 24, no. 7, pp. 2266–2274, 2014, doi: https://doi.org/10.1016/S1003-6326(14)63343-4.
[232] H. S. Abdo, A. H. Seikh, J. A. Mohammed, and M. S. Soliman, “Alloying elements effects on electrical conductivity and mechanical properties of newly fabricated al based alloys produced by conventional casting process,” *Materials*

(Basel)., vol. 14, no. 14, 2021, doi: 10.3390/ma14143971.
[233] R. S. Mishra, Partha Sarathi De, and N. Kumar, *Friction Stir Welding and Processing*, vol. 3. 2009.
[234] "ISO 25239-5:2011, Friction stir welding. Aluminium. Part 5: Quality and inspection requirements." p. 16, 2011.
[235] A. Mauduit and H. Gransac, "Study of the precipitation kinetics and mechanisms in 6000 series aluminium alloys through the measurement of electrical conductivity," *Ann. Chim. Sci. des Mater.*, vol. 44, no. 3, pp. 141–149, 2020, doi: 10.18280/acsm.440301.
[236] F. D. Senghor, G. Wasselynck, H. K. Bui, S. Branchu, D. Trichet, and G. Berthiau, "Electrical Conductivity Tensor Modeling of Stratified Woven-Fabric Carbon Fiber Reinforced Polymer Composite Materials," *IEEE Trans. Magn.*, vol. 53, no. 6, 2017, doi: 10.1109/TMAG.2017.2660529.
[237] A. T. Kermanidis, "Aircraft Aluminum Alloys: Applications and Future Trends BT - Revolutionizing Aircraft Materials and Processes," S. Pantelakis and K. Tserpes, Eds., Cham: Springer International Publishing, 2020, pp. 21–55. doi: 10.1007/978-3-030-35346-9_2.
[238] H. Malekinejad, F. Ramezani, R. J. C. Carbas, E. A. S. Marques, and L. F. M. da Silva, "Study of CFRP Laminate Gradually Modified throughout the Thickness Using Thin Ply under Transvers Tensile Loading," *Materials (Basel).*, vol. 17, no. 10, 2024, doi: 10.3390/ma17102388.
[239] C. Multiphysics, "AC / DC Module User ' s Guide," *Manual*, p. 300, 2012, [Online]. Available: https://doc.comsol.com/5.5/doc/com.comsol.help.acdc/ACDCModuleUsersGuide.pdf
[240] A. Drach, B. Drach, I. Tsukrov, H. Bayraktar, and J. Goering, "Realistic fea modeling of 3D woven composites on mesoscale," *ICCM Int. Conf. Compos. Mater.*, vol. 2013-July, no. February 2015, pp. 1813–1820, 2013.
[241] "UNE-EN ISO 25239-4: Soldeo por fricción-agitación. Aluminio. Parte 4: Especificación y cualificación de los procedimientos de soldeo." 2012.
[242] S. K. Burke, "A benchmark problem for computation of ΔZ in eddy-current nondestructive evaluation (NDE)," *J. Nondestruct. Eval.*, vol. 7, no. 1–2, pp. 35–41, 1988, doi: 10.1007/BF00565775.
[243] N. Athanasopoulos and V. Kostopoulos, "Prediction and experimental validation of the electrical conductivity of dry carbon fiber unidirectional layers," *Compos. Part B Eng.*, vol. 42, no. 6, pp. 1578–1587, 2011, doi: 10.1016/j.compositesb.2011.04.008.
[244] Y. Guo, L. Shi, Z. Huang, and S. Fu, "Research on conductivity temperature dependence of CFRP," *IEEE Int. Symp. Electromagn. Compat.*, vol. 2017-Octob, no. October 2017, pp. 1–3, 2018, doi: 10.1109/EMC-B.2017.8260383.
[245] P. D. Sheet and P. Type, "Toray Cetex TC1225 Toray Cetex TC1225," vol. 31, no. 0, pp. 1–7.
[246] I. F. Villegas and C. Rans, "The dangers of single-lap shear testing in understanding polymer composite welded joints," *Philos. Trans. R. Soc. A Math. Phys. Eng. Sci.*, vol. 379, no. 2203, 2021, doi: 10.1098/rsta.2020.0296.